COMPUTER MODELLING OF THE STRUCTURE AND REACTIVITY OF CARBONATE MINERALS

Katrina Fleur Austen

The Royal Institution of Great Britain
and
University College London

Submitted for the Degree of Ph.D.

March 2006

ProQuest LLC
789 East Eisenhower Parkway
P.O. Box 1346
Ann Arbor, MI 48106-1346

ABSTRACT

Work has been carried out over the last few years on the interaction of dolomite surfaces with common, environmentally significant species that are found in the same geographical locations as the mineral. The thesis has evolved from the desire to understand the molecular processes in this environmental problem. In addition to a number of results elucidating the behaviour of a number of pollutant species in contact with a dolomite surface, it also presents an evaluation of some of the oft-used computational methods applied to such systems.

Initial work was carried out on dry surfaces, studying the substitution of native dolomite cations by six divalent, metal cations that are known to form end-member carbonate minerals: Ni, Mn, Zn, Fe, Cd and Co. It was found that, under vacuum, none of the straightforward surface substitutions was energetically favourable. Substitutions at both the edges and terraces of steps were found to be favourable, although with different ordering of cations. Addition of monolayer solvation at the perfect surface generated substitution ordering in accordance with experimental data, but still most were not favoured. Further, a new implementation of implicit surface solvation, COSMIC [1], has been used in this work. It was found that this method provides a useful tool for investigating relative substitution energies at surfaces, and that, as expected from experiment, substitutions at Mg sites are favoured; a reversal of the vacuum results.

Finally, DFT calculations were used to model the absorption of a more complicated pollutant, the arsenate molecule on the dolomite surface. Initially, implicit and explicit solvation methods were used to model a molecule in solution, which allowed the molecule's behaviour when modelled using DFT to be determined. An *ab initio* solvation energy was calculated for the molecule, which favourably compared with that obtained using implicit solvation methods. In addition, the preferred adsorption configuration of the molecule at the carbonate surface was determined. It was shown that the use of DFT methods are worthwhile in understanding the subtleties of molecular scale surface–solution interactions.

1. Gale, J.D. and A.L. Rohl, *An efficient technique for the prediction of solvent-dependent morphology: The COSMIC method.* In Preparation.

TABLE OF CONTENTS

Title Page 1

Abstract 2

Table of Contents 3

List of Figures 6

List of Tables 8

Introductory Quote 9

Acknowledgements 10

1. Introduction to Thesis 12

1.1. Aim of Thesis 12

1.2. Outline of Thesis 12

2. Introduction 15

2.1. Overview 15

2.2. Carbonate Minerals 15

2.3. Solvated Species 20

2.4. Thesis Content 24

3. Theory and Methodology 40

3.1. Electronic Structure Methods 41

3.1.1. Background 41

3.1.2. Hartree-Fock and Post-HF Methods 42

3.1.3. Density Functional Theory 44

3.1.4. Basis Sets 46

3.2. Empirical Potential Methods 49

3.2.1. Force Field Methods and Energy Minimisation 49

3.2.1.1.The Born Model of Solids 50

3.2.1.2.Long-range Interaction 51

3.2.1.2.1. Evaluating the Coulomb Interaction 51

3.2.1.3.Dispersion Interaction 53
3.2.1.4.Short Range Interactions 54
3.2.1.4.1. Two-body Potentials 54
3.2.1.4.2. Three-body Potentials 56
3.2.1.4.3. Four-body Potentials 56
3.2.1.4.4. Treatment of Polarisability 56
3.2.1.4.5. Potential Cut-offs 57
3.3. Static Geometry Optimisation Calculations 58
3.4. Molecular Dynamics 59
3.5. Surface Calculations 61
3.5.1. Surface Structure 62
3.6. Morphology 65
3.7. Solvation Methods 66
3.7.1. Explicit Solvation Methods 66
3.7.1.1.Monolayer Solvation 67
3.7.1.2.Water Simulation 67
3.7.2. Implicit Solvation: Continuum Dielectrics 67
3.7.2.1.Introduction 67
3.7.2.2.Theory 68
3.7.2.3.Simple Methods 71
3.7.2.4.PCM and Further Developments 73
3.7.2.5.Conductor-Like Models 75
3.7.2.6.Alternative Methods 75
3.7.2.7.Surface Solvation 77
3.8. Conclusions 78

4. Surfaces and Surface Impurities: Results of Metal Substitution Reactions 84

4.1. Methods and Parameters Used 84

4.2. Results and Discussion I: Substitutions on Dry Surfaces 89

4.3. Stepped Surface Substitutions 98

4.4. Results and Discussion II: Substitutions on Wet 102

Surface – Monolayer Solvation

5. Solvation of Surfaces: Results of the Application of Implicit Solvation 110 to Surfaces and the Effect on Energetics

5.1. Methods Used 110

5.2. COSMIC Solvation: Effect on Morphology 112

5.3. COSMIC Solvation: Effect on Impurity Substitution 122

6. Results of Electronic Structure Calculations 131

6.1. Arsenate and Its Structure 132

6.1.1. Effect of Solvation on the Raman Spectra and Energetics of 133 Arsenate

6.1.2. Results of Molecular Dynamics Calculations on Arsenate 140

6.2. Arsenate at the Surface of Dolomite 144

7. Conclusions and Future Work 152

Final Quote 158

LIST OF FIGURES

1.1 Schematic showing the various components of the mineral–water interface 12

2.1 Representation of the unit cell of dolomite 16

3.1 Simplest representation of the shape of a STO and a GTO 47

3.2 Pictorial representation of the Ewald Summation method 52

3.3 The three different types of surfaces, according to Tasker 63

4.1 Surfaces viewed from above for $(10\bar{1}4)$, $(11\bar{2}0)$ and $(30\bar{3}0)$ 92

4.2 Possible cuts on the $(10\bar{2}1)$ surface 93

4.3 Substitution energies for dry dolomite surfaces 96

4.4 View of the relaxed reconstructed $(10\bar{2}1)_{0.03718}$ surface from above 97

4.5 View of relaxed $(10\bar{2}1)_{0.1218}$ surface from above 98

4.6 Structure of the steps on the $(10\bar{1}4)$ surface 99

4.7 The energy difference between pure and defective $(10\bar{1}4)$ stepped surfaces 99

4.8 Stepped surface from above 100

4.9 Most favourable substitution energies for the $(10\bar{1}4)$ surface with steps 100

4.10 Monolayer of water on the $(10\bar{1}4)$ surface of dolomite 102

4.11 Contributions to the energetics of solvated substitutions on the surface 105

5.1 Dry equilibrium morphology and wet equilibrium morphology 113

5.2 Relaxed surfaces of the solvated, non-polar surfaces of dolomite 115

5.3 Morphology derived from surface energy of solvated, non-polar surfaces 117

5.4 COSMIC Morphology including surface energy of the two polar surfaces 118

5.5 Relaxed termination of the polar surfaces of dolomite 120

5.6 Morphology of the surface solvated with a solvent of $\varepsilon=10$ 122

5.7 Graphical representation of the substitution energy as a function of impurity cation and the solvation model applied to the surface 125

6.1 Raman Spectra for AsO_4^{3-} 135

6.2 Raman Spectra for AsO_4H^{2-} 136

6.3 Raman Spectra for $AsO_4H_2^-$ 137

6.4 Raman Spectra for AsO_4H_3 139

6.5 Evolution of the energy during the final 4000 steps of the MD run 141

6.6 Radial Distribution Function for arsenate in a box of water 143

6.7 Examples of the starting configurations for $AsO_4H_2^-$ above the surface of dolomite 145

6.8 Figure 6.8: Most energetically favourable binding configuration for $AsO_4H_2^-$ on the dolomite (211) surface 147

LIST OF TABLES

3.1 Molecular dynamics ensembles 60

4.1 Born-Mayer potentials used in this work 89

4.2 Bulk properties of dolomite 90

4.3 Structural and elastic properties for the end-member carbonates from both theoretical calculations and experiment 91

4.4 Surface energies for $(10\bar{1}4)$, $(11\bar{2}0)$, $(30\bar{3}0)$ and $(10\bar{2}1)$ surfaces 92

4.5 Surface energies of the different reconstructions for the $(10\bar{2}1)$ surface 94

4.6 Enthalpy difference between the pure surface and the defective surface 94

4.7 Average cation-nearest neighbour distance 96

4.8 Likelihood for segregation of impurity cations from end-member minerals to Mg and Ca sites 101

4.9 Substitution energies for $(10\bar{1}4)$ surface with a monolayer of water 105

5.1 Van der Waals' radii used for COSMIC calculations 111

5.2 Wet and dry surface energies for dolomite 112

5.3 Effect of C and O van der Waals' radii on the relative surface energies 116

5.4 Surface energies of dry and solvated (111) surface terminations 118

5.5 Dry and Solvated surface energies of steps on the (211) surface 120

5.6 Surface and solvation energies when using $\varepsilon=10$ 121

5.7 Surface and solvation energies for (211) and $(10\bar{1})$ surfaces 123

5.8 Substitution energetics of solvated surfaces 124

5.9 Total energy of metal-carbonate monomers 126

5.10 Substitution energies for monomer substitution at surfaces 127

6.1 Energies of high and low spin arsenate complexes 132

6.2 Solvation energies of arsenate in varying degrees of protonation 134

6.3 Relative energies and relaxed structures for different starting geometries 146

"An absolutely new idea is one of the rarest things known to man."

Thomas More, 1478-1535.

ACKNOWLEDGEMENTS

I would like to take this opportunity to thank the many people who have provided me with help and support over the course of my PhD., and the various organisations that have provided me with funding.

In the latter category, I would like to thank NERC for my studentship, funding for my DSA, and funding for an overseas fieldtrip, which allowed me to travel to and work in Curtin University of Technology in Perth, Western Australia. Similarly, I would like to thank UCL Graduate School, the British Association for Crystal Growth and the Network for Crystal Growth and Nucleation, each of which provided contributions to the funding for a second fieldtrip to Curtin University of Technology.

Thanks to A. Prof. Kate Wright for her supervision and valuable support and advice, which continued even after her leaving the Davy Faraday Research Laboratory to work in warmer climes, and to Dr. Ben Slater for his supervision. My warmest appreciation is extended to Prof. Julian Gale for both the access to the newest versions of GULP and SIESTA, and also to all of his extremely helpful advice and guidance during my stays in Australia. Whilst in Perth I received a great deal of excellent help from Stefano Piana, to whom I would like to offer special thanks for his advice on Molecular Dynamics. I would like to also thank Tanja van Mourik for agreeing to become my secondary supervisor for my final year, and for her help and advice during that time.

On a more personal note, I would like to thank my wonderful family for their constant emotional support and for providing me with a restful and calm environment in which to finish my thesis. I would also like to thank Vanessa Hill for providing a home from home, and to thank Wisdom Beyhum, Misbah Sarwar and Judy To for the support that only fellow final year students can offer. A special thank you to the marvellous Toby White for his advice and Rich Bruin for study groups and for listening, and to both for being so supportive and welcoming in my new job, and for becoming such fast friends.

Saving the best 'til last, my acknowledgements would not be complete without mentioning Dr. Dan Wilson, without whose support, advice and care I might have succumbed to the trials I've undergone in the last few years, and without whom I would not be so happy, hale and hearty as I am today.

This work is dedicated to the memory of Auntie D., whose life was an inspiration and example to many, including myself.

1. INTRODUCTION TO THESIS

"Education is not the piling on of learning, information, data, facts, or abilities – that is training or instruction – but is rather the making visible what is hidden as a seed."
Thomas More, 1478-1535.

1.1. Aim of the Thesis

The aim of this thesis is to investigate, using computational methods, the structure of carbonate mineral surfaces, focussing on dolomite, $CaMg(CO_3)_2$. The interaction of metal impurities with the surface has been studied, both as metal cations and, in the case of arsenate, as a molecular species. Overall, various methodologies have been explored in order to determine the most computationally inexpensive, yet accurate, method to investigate the structure and reactivity of dolomite surfaces, which can then be transferred to other types of mineral surface.

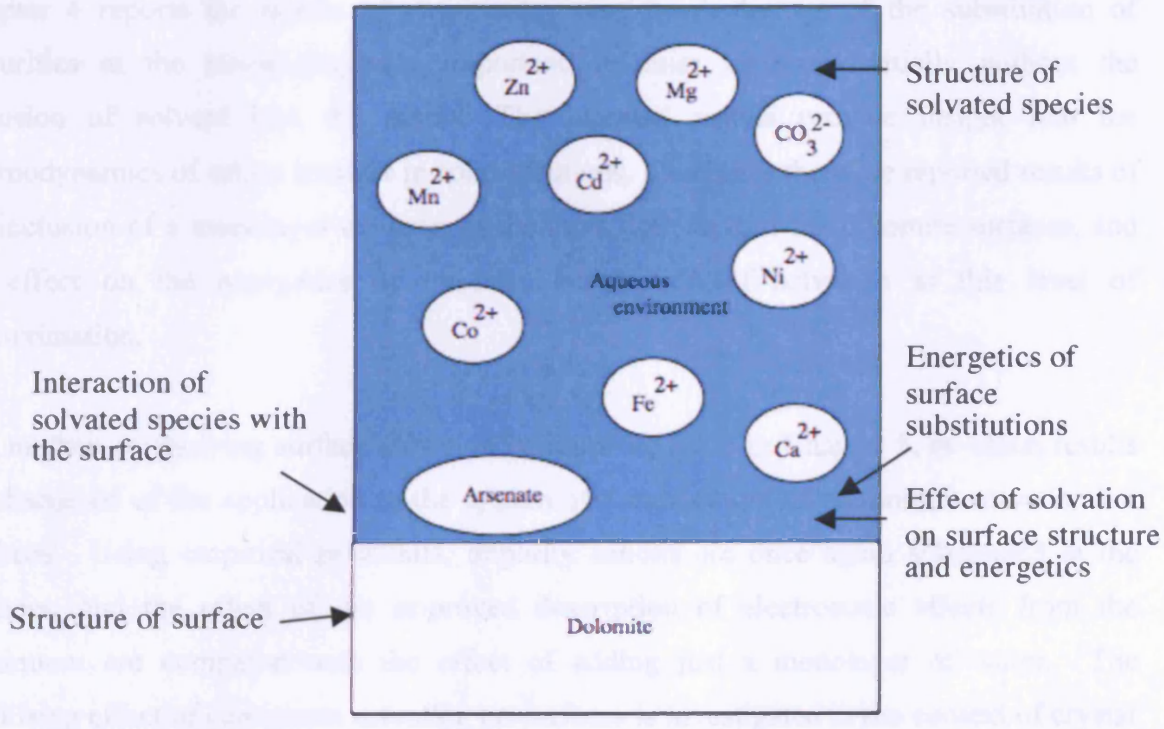

Fig 1.1: Schematic showing the various components of the mineral – water interface

The preceding schematic (Fig 1.1) is representative of the type of system to be studied, and outlines some of the different interactions that must be taken into account in any mineral surface – solution model. The methodology has been developed by starting with the investigation of surfaces under vacuum and subsequently building upon this by solvating the structure using different techniques. Concurrently an effective method has been sought for the solvation of species that will occur naturally in the aquatic environment in which dolomite is found.

1.2. Outline of Thesis

In the Chapter 2, the literature on carbonates and their surfaces, along with literature on relevant solvated species, is reviewed and the work to be carried out is decided upon in the context of previous investigations into this and similar systems. There follows in Chapter 3, a discussion of the various computational techniques that have been employed in this work, in their general application to materials chemistry.

Chapter 4 reports the results of empirical potential calculations of the substitution of impurities at the morphologically important dolomite surfaces, initially without the inclusion of solvent into the model. The reported results provide insight into the thermodynamics of cation transfer in solid-solutions. Thereafter there are reported results of the inclusion of a monolayer of water at the most dominant of the dolomite surfaces, and the effect on the energetics of impurity substitution of solvation at this level of approximation.

The method of studying surface solvation is improved upon in Chapter 5, in which results are discussed of the application to the system of a new model of continuum solvation for surfaces. Using empirical potentials, impurity cations are once again substituted at the surfaces, and the effect of the improved description of electrostatic effects from the continuum are compared with the effect of adding just a monolayer of water. The stabilising effect of continuum solvation on surfaces is investigated in the context of crystal

morphology prediction, and some resultant strengths and deficiencies in the model are outlined.

The final results chapter, Chapter 6, details Density Functional Theory calculations of a molecular pollutant in solution and adsorbed on the dolomite surface. The geometry of the molecule both in solution and at the surface is calculated, as are adsorption and solvation energies. The importance of the inclusion of solvation effects in calculations of environmental problems of the nature addressed in this work is highlighted by calculation of the Raman spectra of the molecule and its ions, comparing vacuum with those obtained using an implicit solvation model and also with experimental spectra. The Conclusions and Further Work in Chapter 7 discuss the results of the work carried out for the production of this thesis. Work on explicit solvation of the dominant dolomite surface that was begun during the period over which this thesis was written is also discussed.

2. INTRODUCTION

"Knowledge itself is power." Francis Bacon, 1597.

2.1. Overview

There follows introductions to the various components of the system, and a review of the current literature on the subjects. The literature will be discussed in more detail, where appropriate, in later chapters, wherein new results are presented.

2.2. Carbonate Minerals

Dolomite, $CaMg(CO_3)_2$, is often found in dolomitic limestone. Its rhombohedral crystals reflect the rhombohedral nature of its unit cell, which is commonly represented in two ways: the hexagonal unit cell or the primitive unit cell (Fig. 2.1). It has a similar structure to calcite, with every other layer of Ca^{2+} ions being replaced by Mg^{2+}. The presence of magnesium in the structure leads to reduced symmetry in comparison to its single cation counterparts, giving rise to the space group R-3. The process of dolomite formation has been a subject of discussion for many years, as it formed in large amounts in the geologic past but more recent formation is scarce. In the laboratory, dolomite will not form from its components unless subjected to forcing conditions, such as temperatures above 400°C [1]. The question of why older specimens of dolomite abound so copiously, in conjunction with its present-day rarity of formation, is known as the dolomite problem [2-4]. An interesting, and related, quirk of dolomite is its defiance of Ostwald's rule [5], which states that in nature a metastable phase of a mineral will form before the stable phase. However, the metastable phase of dolomite does not form in nature, but will form in the laboratory at room temperature and pressure [6]. It is necessary to subject the reagents to low temperature and fluctuations in pH in order for the stable phase to nucleate in the laboratory [7].

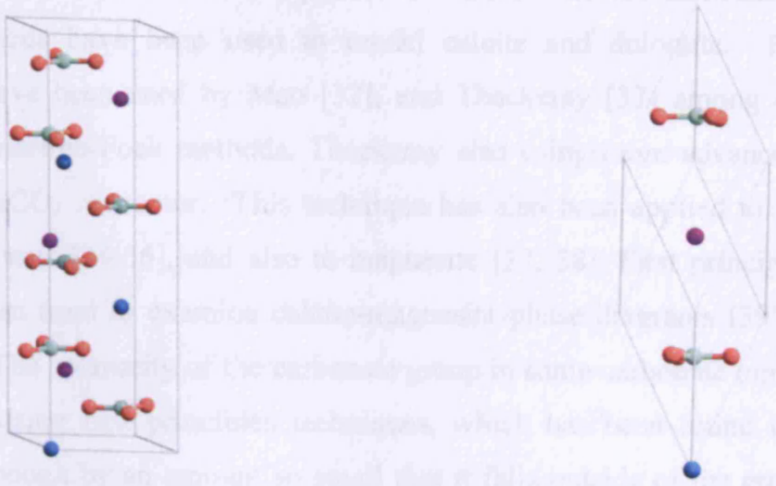

Figure 2.1: Representations of the unit cell of dolomite: Left – hexagonal unit cell, right – primitive unit cell (Ca = blue, Mg = purple, C = green, O = red).

There has been some work on determining carbonate shape due to different types of precipitation reactions in the laboratory [8, 9]. It was shown that calcite crystal morphology was affected by the concentration of sodium silicate present in solution, and can also be manipulated by polymers present at the time of precipitation, or the application of templates. It is generally accepted that the morphology of dolomite consists of the expression of the predominant $(10\bar{1}4)$ surface, although other surfaces are sometimes observed: $(11\bar{2}0)$, $(30\bar{3}0)$ and $(10\bar{2}1)$. Calcite expresses a much wider variety of morphologies [10]. The prediction of crystal morphology has become a routine practice in computer modelling [11, 12], and has been widely applied to carbonate minerals [13-16], and the effect of impurities thereupon [17].

Calcite and dolomite are the most prolific carbonate minerals in nature, together comprising 90% of the carbonate minerals found in rocks [18]. Calcite has been studied extensively using various surface analytical techniques, such as X-ray photoelectron spectroscopy (XPS [19-22] and, most frequently, Atomic Force Microscopy (AFM) [23-30]. In comparison little is known about the surface structure of dolomite, and consequently its reaction to its environment. Some studies have shown that reaction rates for dolomite are slower than for calcite, which makes experimental studies of the mineral more difficult [31].

There have been a number of computational studies into the carbonate minerals and various methods have been used to model calcite and dolomite. First principles techniques have been used by Mao [32], and Thackeray [33] among others, both of whom used Hartree-Fock methods, Thackeray also using more advanced methods, to model the $CaCO_3$ monomer. This technique has also been applied to the calcite and aragonite crystals [34-36], and also to magnesite [37, 38]. First principle calculations have also been used to examine calcite-magnesite phase diagrams [39], and stiffness values [40]. The aplanarity of the carbonate group in some carbonate minerals has been investigated using first principles techniques, which has been found to stabilise the minerals, although by an amount so small that it falls outside of the error margins for most empirical potential studies [41]. A precedent has been set for using atomistic techniques to study both the bulk properties [16, 35, 42] and the surface structures [14, 43, 44] of the carbonates. Interatomic potential methods have been used to investigate growth and dissolution of various carbonate minerals, focussing on pit formation and migration of ion pairs along steps [45]. Defects in the bulk structure of carbonates have been successfully studied [42]. In particular, there has been some previous modelling of some dolomite surfaces [13, 18, 46]. An experimental study of the calcite $(10\bar{1}4)$ surface has shown that there is a 2 x 1 reconstruction of the surface [47, 48], and potentials have been developed to incorporate this into the description of carbonate ion bending when under-coordinated [49].

Carbonate minerals have been shown to chemically interact with various solvated ions and molecules when exposed to aqueous solutions [20, 50-52]. Dolomite and other common carbonate minerals, are frequently exposed to aqueous solutions in nature that contain many environmentally damaging elements, such as zinc, lead, iron, cadmium and nickel [53, 54]. It has been observed that carbonates are important in sulphide rich mine tailings [55, 56] where they are observed to trap iron [56, 57]. Luminescence in dolomite has been observed as a consequence of iron and manganese impurities [1]. The partitioning of Mn impurities has been studied extensively using experimental techniques. Thermoluminescence [58] and cathodeluminescence [59] studies have shown that Mn^{2+} will substitute at both Mg and Ca sites, and Electron Paramagnetic Resonance spectroscopy (EPR) has shown that the distribution favours impurities in Mg sites [60], the ratio of Ca:Mg site substitution being determined by the environmental

conditions at the time of dolomite formation [61, 62]. Calcite has been observed to contain zoned Pb, Zn, Mn and Fe impurities [54], and Fe has been observed to replace Mg in magnesite [63, 64]. Carbonates are also responsible for sulphide removal from solution [65-67] and are important in biogeochemical cycles such as the carbon cycle [31, 68, 69]. It has been shown that through a combination of processes; surface complexation, adsorption and co-precipitation, carbonates help reduce latent acidity in low pH waters, such as mine tailings [55]. This low pH causes the release of trace elements, such as Fe, Al, Cu, Pb and Zn, into the water thereby polluting it and causing environmental damage [55]. Dissolution of the carbonate minerals gives rise to an increase in pH [55, 70]. As a consequence, solubility of the pollutant metals decreases, it becomes less favourable for them to remain in solution, and precipitation will occur [70]. Experimental studies have shown that the sample size of carbonates affects their behaviour under these circumstances [71]. It has also been shown that the rates of dissolution decrease over time, although overall dissolution rates and mechanisms are an area of controversy [71-74]. It is likely that the rate change is partly attributable to the observed build-up of precipitates, such as iron hydroxide, on the surface of calcite, although this phenomenon is not as readily observed in dolomite [71]. In the case of dolomite it is more likely that the rates decrease due to preferential initial dissolution of $CaCO_3$, and once the source of $CaCO_3$ is diminished the rate is influenced more, and hence slowed, by the presence of $MgCO_3$ [73]. However, the dissolution of dolomite has been shown, using vertical scanning interferometry, to involve etch-pit evolution in combination with stepwave advancement across the surface [74]. The aforementioned properties of cycling and entrapment of impurities are already exploited to some extent in industry, and here it has also been shown that particle size is important [75]. Carbonates are used to remove Cd^{2+} from industrial by-products, sometimes to reduce wastage [76]. Dolomite is also used in industry for dye removal from waste water by entrapment of the dye due to adsorption [77].

Experimental studies have been carried out into the interaction of solvated impurities with the surfaces of carbonate minerals during growth. Step-site specificity has been observed in the incorporation of Co, Cd, Zn and Ba at the calcite $(10\bar{1}4)$ surface through Synchrotron X-ray Fluorescence Microanalysis [78], and AFM confirms this is the case for Ba [79], and also for Mn [80]. Boron shows similar site specificity on

calcite [81], as does Cu^{2+} [82]. XSW and Surface Extended X-ray Absorption Fine Structure (SEXAFS) studies of Co on calcite surfaces have shown that the impurity will be displaced with respect to the position of the replaced Ca ion [83]. Surface studies of dolomite are rarer, though it has been shown that actinides exchange with Ca on dolomite surfaces over a range of pHs [84].

Many studies of impurities on calcite surfaces have been made using computational techniques [43, 44, 85-90]. Previous computational studies of impurities in dolomite [46] concentrated on impurity substitution at the bulk and on the common $(10\bar{1}4)$ surface [91]. The effect of non-stoichiometry on these substitutions [46] was also considered, and diffusion in the bulk was also studied [91]. The impurities studied were the divalent cations of Mn, Fe, Cd, Co, Zn and Ni, which are often found to be present, along with dolomite, in aquatic environments. The calculated values of the substitution energies indicated a strong preference of impurity elements to substitute at Ca rather than Mg sites, both in the bulk and at the surface. The segregation energy, however, was found to be an important indicator of the preference for substitution at the different cation sites. A first-principles study of SO_2 adsorption on calcite and dolomite structures has predicted a preference for sorption on calcite surfaces. Bulk defect calculations have been carried out for calcite, and a range of end-member carbonate minerals have been studied [42]. Additionally, disorder and non-stoichiometry in the dolomite structure has been studied [18, 42].

It should be noted that most of these computational investigations model the surfaces at the point of zero charge (PZC), where there is no ionic mobility at the surface. The PZC for carbonates is environment dependent, but for dolomite at average pCO_2 and solution concentrations, the value is pH 8 [92]. At pHs other than that of the PZC, the surface is charged and compensates by forming an electronic double-layer with the surrounding solution, where charges opposite to those found at the surface form a charge-compensating layer above the surface. This charge compensation is quickly found to become diffuse further away from the surface.

Studies have been carried out on the nature of water at the carbonate-solution interface, specifically whether dissociation of water occurs. X-ray photoelectron spectroscopy

(XPS), time-of-flight secondary ion mass spectrometry (TOF-SIMS) and Low Energy Electron Diffraction (LEED) results have been interpreted to indicate that water will dissociate on the calcite surface [29, 47, 93], and dissociated water has been included in theoretical surface speciation models for both dolomite [92] and calcite [94]. However, there is controversy over the interpretation of these results [29, 95], high-resolution X-ray reflectivity measurements, which, it should be noted, are not very sensitive to hydrogen atoms, have suggested that at the PZC for calcite there is no dissociation [96] and computational modelling of the calcite $(10\bar{1}4)$ surface has indicated that water dissociation on the surface is unlikely to occur [97]. Computational studies have, however asserted that there is layering of the water molecules up to 10Å from the surface [98], though this has not been observed experimentally, despite the same method showing ordering for other solid-water interfaces (KDP, orthoclase and muscovite) [99].

2.3. Solvated Species

The structure of species in solution is of importance in the complexation of these species with mineral surfaces, as both the strength of the binding energy between water and the solvated species and the solvation energy of the species play a part in the propensity for complexation to take place.

There have been a number of studies into the coordination numbers of the hydration shell around metal cations, and their vibrations [100-119]. Molecular Dynamics studies have been carried out looking at the change in the hydration shell and free energy of metal cations on their approach to the calcite $(10\bar{1}4)$ surface [98, 120], and it was found that there is a large electrostatic free energy barrier that governs the formation of innersphere complexes at the surface. This type of calculation yields important information on the incorporation and release of solvated species into and out of minerals, through the processes of growth and dissolution.

In this work, the nature of arsenic species in solution is of great importance when considering its interactions with minerals. There have been a vast number of studies into arsenic and its compounds because of its impact on human health and the

environment [121, 122]. Pollution from human activity has elevated environmental arsenic levels, increasing their concentrations in areas around industrial plants and mines [121, 123, 124].

Arsenic is known to form insoluble complexes with iron, calcium and magnesium, and forms a variety of interesting compounds with the transition metals and with organic ligands [125]. Organic arsenic compounds have increased in nature due to anthropological input. However, important, naturally occurring arsenic species tend to be in the form of inorganic trivalent (As (III)) or pentavalent (As(V)) arsenic oxyanions, the relative proportions of these being governed by the redox potential and aqueous solution pH [121]. It has been determined that $AsO(OH)_3$ is a stronger acid than is arsenite $As(OH)_3$ [126]. Arsenate loses its first proton at a pH of 2.25, its second at 6.77 and its third at 11.6 [126]. Under oxidising conditions, As(V) will predominate, and will usually be in the form of either the arsenate molecule, or $[AsO_2(OH)_2]^-$ [127, 128], although the redox potential of As(III)-As(V) is affected by the concomitant presence of metal and transition metal ions. For, example the redox reaction between As(III) and Fe(III) results in As(V) and Fe(II) [129]. In most groundwaters it is expected that As(V) will be the species more strongly sorbed onto mineral surfaces [121, 130].

There have been many studies into the complexation of arsenic species with minerals, combining computational and experimental methods [131-133]; the latter both being field-based [132, 134] and laboratory studies. The interaction of arsenate with gibbsite [135], iron (III) hydroxides [136], and hematite [131] have been studied using controlled laboratory techniques, determining the complexation mechanism through a combination of Extended X-ray Absorption Fine Structure (EXAFS) and Density Functional Theory calculations. Complexation with Zn and goethite under aqueous conditions has also been probed with EXAFS [137]. Fourier Transform Infra-Red and semi-empirical calculations have been used to study the structure of arsenate in water and at Ca and Al-hydroxide surfaces [138], and the arsenic content in pyrites [139] and natural waters [140] have been determined by Inductively Coupled Plasma-Mass Spectrometry (ICP-MS) techniques. There have been few studies into the interaction between carbonate minerals and dissolved arsenic species. Cheng *et al.* [141] have investigated the incorporation of arsenite (As(III)) on the $(10\bar{1}4)$ surface of calcite

using the X-ray standing waves (XSW) technique, finding that the deprotonated arsenite ion will occupy vacant surface carbonate sites, though attempts to reproduce these results with arsenate molecules were unsuccessful. A Scanning Electron Microscopy (SEM) study on the removal of arsenate from alkaline solutions indicated that, in the presence of dolomite and portlandite, at high pH, an unidentified calcium arsenate phase will precipitate out immediately [142]. It has been observed that As(III) may form aqueous complexes with carbonate ions [143], however their existence has not been conclusively proven and the interaction between carbonate and arsenic species remains ambiguous and somewhat unexplored [144]. This point is made eloquently by P. L. Smedley and Kinniburgh in their review article of 2002 [121]:

> The extent of As(V) sorption to, and coprecipitation on, carbonate minerals in unknown but if it behaves like phosphate, it is likely to be strongly retained by these minerals and this may limit As concentrations in groundwaters from limestone aquifers.

There are known carbonate minerals that contain arsenates [145]. In 2003 a new mineral, sailaufite, associated with calcite and dolomite, and found to grow on calcite, was found in the Spessart mountains in Germany [146]. Its idealised composition is suggested to be $CaNaMn^{3+}{}_3O_2(AsO_4)_2(CO_3).3H_2O$, and its discovery indicates that pentavalent arsenic can interact with carbonate surfaces.

Investigations into the solvated structure of arsenic oxyanions have been carried out using experimental [147-155] and computational techniques [156-159], and sometimes a combination of both [138, 148]. Many of the experimental studies have concentrated on arsenite speciation and vibrational spectra [147, 160], with one study suggesting a possibility of arsenite polymerisation in solution [147], were the concentration high enough. The concentration of arsenic needed for this polymerisation to occur is stated as 2-5.2 mol kg^{-1}, which translates to between 150 and 390 g kg^{-1}. In natural, unaffected groundwater, even in areas such as Mexico and the Bengal Basin, where the concentration of arsenic is highest, it does not exceed 0.005 g kg^{-1} [121]. In areas affected by mining or application of arsenical herbicides, the concentration has not been observed to be higher than 0.8 g kg^{-1} [161], precluding the possibility of polymerisation in natural systems. Further, polymerisation has not been observed in other studies of highly concentrated arsenite solutions [149, 155] and has been found to be energetically

unfavourable in a theoretical study [148], although polymerisation has been observed at high arsenite concentrations in hydrothermal waters [151].

The Raman spectra of solvated arsenite and arsenate have been reported a number of times [153-155]. Eysel and Wagner [154] give a detailed report of the Raman spectrum of the fully deprotonated arsenate ion, gleaning the bond polarisability and Raman intensities from their data. A comprehensive report of the Raman spectra of arsenic acid, in all its degrees of protonation, is given by Vasant [153], and is in fair agreement with the later work of Eysel and Wagner regarding the spectrum for the fully deprotonated ion. Vasant's second paper reports the force constants and bond orders for arsenic acid, which vary from those reported later, though this is probably due to the discrepancy in bond lengths used in the calculations.

There have been reports on the hydration numbers and stability of arsenite complexes in mixed water-organic compound solutions [149], and the Raman spectra of the solutions collected as a function of water activity. Hydration numbers for arsenite were determined as a function of the equilibrium constant for hydration reactions [149], and reports a hydration number of 4 to be the most likely, corresponding to a tightly bound $As(OH)_3 \cdot 4H_2O$ species at ambient temperatures. Results from a combined XAS and DFT/MP2 study conflict with this, asserting that 3 rather than 4 water molecules will coordinate around the fully protonated, solvated arsenite species [148]. In contrast, no data can be found in the literature for the hydration number of arsenate in any form.

Tossell has carried out a number of studies into aqueous arsenic (III) compounds using computational techniques [156-158]. Initial work used a low quality basis set and Hartree-Fock theory, and the authors chose to scale the vibrational frequencies [157], although later work improved upon these methods, using time-dependent DFT and HF, and a variety of basis sets, effectively allowing for methodological comparisons to be made [156]. Solvation is achieved via both microsolvation, modelling the suggested $As(OH)_3 \cdot 4H_2O$ species of Pokrovski *et al.* [149], and by use of polarisable continuum methods. It was found that the IPCM solvation method used underestimated the shift in UV spectra between the gas phase and aqueous species. It was shown in this study that, while a smaller basis set was adequate for the description of the uncharged species,

deprotonated species required a larger basis set to describe them to an acceptable accuracy.

An extensive combined experimental and theoretical study of arsenate coordination in various environments has been carried out by Myneni and co-workers [138]. IR and Raman spectroscopy of solvated AsO_4^{3-} were measured and the influence of protonation was investigated, with the resulting spectra in fair agreement with earlier studies [153, 154]. Semi-empirical computational calculations were carried out on the various protonated states of arsenate, and up to 4 water molecules were included in the calculations to approximate the effect of solvation. The vibrational frequencies derived from these calculations were higher than experimental values by as many as 100 cm^{-1}, which is due, at least in part, to the incomplete solvation model. One conclusion reached by this study was that the data gleaned from studying the solvated structure of arsenate, both alone and complexed with different species, while informative, cannot conclusively aid the interpretation of surface-solution interface spectra with a view to understanding complexation mechanisms of arsenate at mineral surfaces. Clearly, there is here an opening for higher-level, computational studies to give a molecular-scale picture of the interaction of this important semi-metal with prevalent mineral surfaces. Further, there is obviously a need for a complete theoretical model for modelling mineral-solution interfaces and the molecular scale interactions thereupon with solvated species in general.

2.4. Thesis Content

A review of the literature covering the topics pertinent to the study of carbonate mineral – aqueous solution interfaces has highlighted a number of issues that it is the purpose of this work to address. Part of this study extends previous work to look at the complete set of dolomite's morphologically important surfaces, using an improved description of the mineral. The influence of water upon substitution energetics is examined, and a comparison made of different solvation models. Further, in the interest of devising the most realistic model possible, the incorporation of cations at a stepped surface is investigated. The results are rationalised in the context of uptake of cations, either from solution or from mineral sources, on dolomite crystals.

The structure of water around solvated pentavalent arsenic species is determined, and their interaction with the dolomite surface is probed using computational techniques. These studies, using various methodologies, lead to the development of a computational model for the investigation of mineral-solution interfaces.

1. Braithwaite, C.J.R., *Dolomites, A Review Of Origins, Geometry And Textures.* Transactions Of The Royal Society Of Edinburgh-Earth Sciences, 1991. **82**: p. 99-112.
2. Kelleher, I.J. and S.A.T. Redfern, *Hydrous calcium magnesium carbonate, a possible precursor to the formation of sedimentary dolomite.* Molecular Simulation, 2002. **28**(6-7): p. 557-572.
3. Holland, H.D. and H. Zimmerman, *The dolomite problem revisited.* International Geology Review, 2000. **42**(6): p. 481-490.
4. Arvidson, R.S. and F.T. Mackenzie, *The dolomite problem: Control of precipitation kinetics by temperature and saturation state.* American Journal of Science, 1999. **299**(4): p. 257-288.
5. Putnis, A., *Introduction to Mineral Sciences.* Cambridge University Press, Cambridge, 1992.
6. Deelman, J.C., *Breaking Ostwald's Rule.* Chemie Der Erde-Geochemistry, 2001. **61**(3): p. 224-235.
7. Deelman, J.C., *Low-temperature nucleation of magnesite and dolomite.* Neues Jahrbuch Fur Mineralogie-Monatshefte, 1999(7): p. 289-302.
8. Lakshminarayanan, R. and S. Valiyaveettil, *Influence of silicate anions on the morphology of calcite crystals.* Crystal Growth & Design, 2003. **3**(4): p. 611-614.
9. Colfen, H., *Precipitation of carbonates: recent progress in controlled production of complex shapes.* Current Opinion in Colloid & Interface Science, 2003. **8**(1): p. 23-31.
10. Cornelis Klein, C.D.A.H., James Dwight Dana, *Manual of Mineralogy.* 21st Edition ed. 1998, London: John Wiley & Sons Inc.
11. Rohl, A.L., *Computer prediction of crystal morphology.* Current Opinion In Solid State & Materials Science, 2003. **7**(1): p. 21-26.

12. Kenway, P.R., et al., *Computer-Simulation Of Surface Segregation.* Molecular Simulation, 1992. **9**(2): p. 83-98.
13. Titiloye, J.O., N.H. de Leeuw, and S.C. Parker, *Atomistic simulation of the differences between calcite and dolomite surfaces.* Geochimica Et Cosmochimica Acta, 1998. **62**(15): p. 2637-2641.
14. de Leeuw, N.H. and S.C. Parker, *Surface structure and morphology of calcium carbonate polymorphs calcite, aragonite, and vaterite: An atomistic approach.* Journal of Physical Chemistry B, 1998. **102**(16): p. 2914-2922.
15. de Leeuw, N.H. and S.C. Parker, *Atomistic simulation of mineral surfaces.* Molecular Simulation, 2000. **24**(1-3): p. 71-+.
16. Parker, S.C., J.O. Titiloye, and G.W. Watson, *Molecular modelling of carbonate minerals: studies of growth and morphology.* Philosophical Transactions of the Royal Society of London, A, 1993. **344**: p. 37-48.
17. Braybrook, A.L., et al., *Parallel computational and experimental studies of the morphological modification of calcium carbonate by cobalt.* Journal Of Crystal Growth, 2002. **243**(2): p. 336-344.
18. De Leeuw, N.H., *Surface structures, stabilities, and growth of magnesian calcites: A computational investigation from the perspective of dolomite formation.* American Mineralogist, 2002. **87**(5-6): p. 679-689.
19. Stipp, S.L., et al., *Cd^{2+} Uptake by Calcite, Solid-State Diffusion, and the Formation of Solid-Solution - Interface Processes Observed with near-Surface Sensitive Techniques (Xps, Leed, and Aes).* Geochimica Et Cosmochimica Acta, 1992. **56**(5): p. 1941-1954.
20. Garcia-Sanchez, A. and E. Alvarez-Ayuso, *Sorption of Zn, Cd and Cr on calcite. Application to purification of industrial wastewaters.* Minerals Engineering, 2002. **15**(7): p. 539-547.
21. Baer, D.R. and D.L. Blanchard, *Studies of the Calcite Cleavage Surface for Comparison with Calculation.* Applied Surface Science, 1993. **72**(4): p. 295-300.
22. Baer, D.R., et al., *The Interaction of Water and Mn with Surfaces of $CaCO_3$ - an Xps Study.* Surface and Interface Analysis, 1991. **17**(1): p. 25-30.
23. Baer, D.R., et al., *Anisotropic processes on the calcite surface: Atomic force microscopy and kinetic Monte Carlo views of dissolution.* Abstracts of Papers of the American Chemical Society, 1996. **211**: p. 67-COLL.

24. De Giudici, G., *Surface control vs. diffusion control during calcite dissolution: Dependence of step-edge velocity upon solution pH.* American Mineralogist, 2002. **87**(10): p. 1279-1285.

25. Hillner, P.E., et al., *AFM Images of Dissolution and Growth on a Calcite Crystal.* Ultramicroscopy, 1992. **42**: p. 1387-1393.

26. Liang, Y. and D.R. Baer, *Anisotropic dissolution at the $CaCO_3$(10.4)-water interface.* Surface Science, 1997. **373**(2-3): p. 275-287.

27. Liang, Y., et al., *Dissolution kinetics at the calcite-water interface.* Geochimica Et Cosmochimica Acta, 1996. **60**(23): p. 4883-4887.

28. Liang, Y., et al., *Interplay between step velocity and morphology during the dissolution of $CaCO_3$ surface.* Journal of Vacuum Science & Technology a-Vacuum Surfaces and Films, 1996. **14**(3): p. 1368-1375.

29. Liang, Y., et al., *Structure of the cleaved $CaCO_3$ (10.4) surface in an aqueous environment.* Surface Science, 1996. **351**(1-3): p. 172-182.

30. Liao, L.B., Z.S. Ma, and N.C. Shi, *Atomic-Force Microscopy of Calcite Surface.* Chinese Science Bulletin, 1993. **38**(24): p. 2058-2061.

31. Morse, J.W. and R.S. Arvidson, *The dissolution kinetics of major sedimentary carbonate minerals.* Earth-Science Reviews, 2002. **58**(1-2): p. 51-84.

32. Mao, Y. and P.D. Siders, *Molecular Hartree-Fock model of calcium carbonate.* Theochem-Journal of Molecular Structure, 1997. **419**: p. 173-184.

33. Thackeray, D.J. and P.D. Siders, *Molecular-orbital and empirical-potential descriptions of $CaCO_3$.* Journal of the Chemical Society-Faraday Transactions, 1998. **94**: p. 2653-2661.

34. Aquilano, D., et al., *Theoretical equilibrium and growth morphology of $CaCO_3$ polymorphs.1. Aragonite.* Journal of Crystal Growth, 1997. **182**(1-2): p. 168-184.

35. Pavese, A., et al., *Modelling of the thermal dependence of structural and elastic properties of calcite, $CaCO_3$.* Physics and Chemistry of Minerals, 1996. **23**(2): p. 89-93.

36. Catti, M., et al., *Quantum-Mechanical Hartree-Fock Study of Calcite ($CaCO_3$) at Variable-Pressure, and Comparison with Magnesite ($MgCO_3$).* Physics and Chemistry of Minerals, 1993. **20**(2): p. 104-110.

37. Catti, M. and A. Pavese, *Theoretical structure factors and electron density of magnesite ($MgCO_3$).* Acta Crystallographica Section A, 1996. **52**: p. 413-418.

38. Catti, M., et al., *Static Lattice and Electron Properties of $MgCO_3$ (Magnesite) Calculated by Abinitio Periodic Hartree-Fock Methods.* Physical Review B, 1993. **47**(15): p. 9189-9198.

39. Burton, B.P. and A.V. de Walle, *First-principles-based calculations of the $CaCO_3$-$MgCO_3$ and $CdCO_3$-$MgCO_3$ subsolidus phase diagrams.* Physics and Chemistry of Minerals, 2003. **30**(2): p. 88-97.

40. Le Page, Y., P. Saxe, and J.R. Rodgers, *Ab initio stiffness for low quartz and calcite.* Physica Status Solidi B-Basic Research, 2002. **229**(3): p. 1155-1161.

41. Winkler, B., J. Zemann, and V. Milman, *Aplanarity of CO_3^{2-} groups: a theoretical investigation.* Acta Crystallographica Section B-Structural Science, 2000. **56**: p. 648-653.

42. Fisler, D.K., J.D. Gale, and R.T. Cygan, *A shell model for the simulation of rhombohedral carbonate minerals and their point defects.* American Mineralogist, 2000. **85**(1): p. 217-224.

43. de Leeuw, N.H., *Molecular dynamics simulations of the growth inhibiting effect of Fe^{2+}, Mg^{2+}, Cd^{2+}, and Sr^{2+} on calcite crystal growth.* Journal of Physical Chemistry B, 2002. **106**(20): p. 5241-5249.

44. Parker, S.C., et al., *Modelling inorganic solids and their interfaces: A combined approach of atomistic and electronic structure simulation techniques.* Faraday Discussions, 2003. **124**: p. 155-170.

45. Duckworth, O.W. and S.T. Martin, *Dissolution rates and pit morphologies of rhombohedral carbonate minerals.* American Mineralogist, 2004. **89**(4): p. 554-563.

46. Wright, K., R.T. Cygan, and B. Slater, *Impurities and nonstoichiometry in the bulk and on the (1014) surface of dolomite.* Geochimica Et Cosmochimica Acta, 2002. **66**(14): p. 2541-2546.

47. Stipp, S.L. and M.F. Hochella, *Structure and Bonding Environments at the Calcite Surface as Observed with X-Ray Photoelectron-Spectroscopy (XPS) and Low- Energy Electron-Diffraction (Leed).* Geochimica Et Cosmochimica Acta, 1991. **55**(6): p. 1723-1736.

48. Stipp, S.L.S., C.M. Eggleston, and B.S. Nielsen, *Calcite Surface-Structure Observed at Microtopographic and Molecular Scales with Atomic-Force Microscopy (AFM).* Geochimica Et Cosmochimica Acta, 1994. **58**(14): p. 3023-3033.

49. Rohl, A.L., K. Wright, and J.D. Gale, *Evidence from surface phonons for the (2x1) reconstruction of the (10.4) surface of calcite from computer simulation.* American Mineralogist, 2003. **88**(5-6): p. 921-925.

50. Martin-Garin, A., P. Van Cappellen, and L. Charlet, *Aqueous cadmium uptake by calcite: A stirred flow-through reactor study.* Geochimica Et Cosmochimica Acta, 2003. **67**(15): p. 2763-2774.

51. Makarov, V.N., et al., *Calcite and dolomite for the decontamination of process solutions from heavy metals and iron.* Russian Journal of Inorganic Chemistry, 2001. **46**(11): p. 1646-1654.

52. Moturi, M.C.Z., M. Rawat, and V. Subramanian, *Distribution and fractionation of heavy metals in solid waste from selected sites in the industrial belt of Delhi, India.* Environmental Monitoring and Assessment, 2004. **95**(1-3): p. 183-199.

53. De la Villa, R.V., M. De la Flor, and V. Cala, *Influence of carbonate on cadmium distribution in soils under semiarid environment.* Agrochimica, 1997. **41**(6): p. 270-278.

54. Wogelius, R.A., et al., *Trace element and isotopic zonation in vein calcite from the Mendip Hills, UK, with spatial-process correlation analysis.* Geochimica Et Cosmochimica Acta, 1997. **61**(10): p. 2037-2051.

55. Al, T.A., C.J. Martin, and D.W. Blowes, *Carbonate-mineral/water interactions in sulfide-rich mine tailings.* Geochimica Et Cosmochimica Acta, 2000. **64**(23): p. 3933-3948.

56. Jacimovic, R., et al., *Determination of major and trace elements in some minerals by k(0)-instrumental neutron activation analysis.* Journal of Radioanalytical and Nuclear Chemistry, 2002. **253**(3): p. 427-434.

57. Billon, G., et al., *Depth variability and some geochemical characteristics of Fe, Mn, Ca, Mg, Sr, S, P, Cd and Zn in anoxic sediments from Authie Bay (Northern France).* Estuarine Coastal and Shelf Science, 2002. **55**(2): p. 167-181.

58. Calderon, T., et al., *Crystal field effects on the thermoluminescence of manganese in carbonate lattices.* Radiation Measurements, 1996. **26**(5): p. 719-731.

59. Galoisy, L., *Local versus average structure around cations in minerals from spectroscopic and diffraction measurements.* Physics and Chemistry of Minerals, 1996. **23**(4-5): p. 217-225.

60. Granwehr, J., P.G. Weidler, and A.U. Gehring, *The fate of structure-bound Mn2+ during the decomposition of dolomite and in the resulting conversion products.* Geochimica Et Cosmochimica Acta, 2004. **68**(11): p. A107-A107.

61. Lumsden, D.N. and R.V. Lloyd, *Mn(II) Partitioning Between Calcium And Magnesium Sites In Studies Of Dolomite Origin.* Geochimica Et Cosmochimica Acta, 1984. **48**(9): p. 1861-1865.

62. Wildeman, T.R., *Distribution Of Mn^{2+} In Some Carbonates By Electron Paramagnetic Resonance.* Chemical Geology, 1970. **5**(3): p. 167-&.

63. Zhang, J.Z., et al., *Effects of Mg-Fe^{2+} substitution in calcite-structure carbonates: Thermoelastic properties.* American Mineralogist, 1998. **83**(3-4): p. 280-287.

64. Bottcher, M.E. and P.L. Gehlken, *Cationic Substitution in Natural Siderite-Magnesite ($FeCO_3$- $MgCO_3$) Solid-Solutions - a FTIR Spectroscopic Study.* Neues Jahrbuch Fur Mineralogie-Abhandlungen, 1995. **169**(1): p. 81-95.

65. Anthony, E.J., et al., *Agglomeration behavior of dolomitic sorbents during long-term sulfation.* Energy & Fuels, 2003. **17**(2): p. 348-353.

66. Hartman, M., et al., *Reactions of calcium and magnesium materials in high-temperature desulfurization of flue and fuel gases.* Chemicke Listy, 2002. **96**(10): p. 777-783.

67. Montagnaro, F., P. Salatino, and F. Scala, *The influence of sorbent properties and reaction temperature on sorbent attrition, sulfur uptake, and particle sulfation pattern during fluidized-bed desulfurization.* Combustion Science and Technology, 2002. **174**(11-2): p. 151-169.

68. Van Cappellen, P., et al., *A Surface Complexation Model of the Carbonate Mineral-Aqueous Solution Interface.* Geochimica Et Cosmochimica Acta, 1993. **57**(15): p. 3505-3518.

69. Morse, J.W., *The Surface-Chemistry of Calcium-Carbonate Minerals in Natural- Waters - an Overview.* Marine Chemistry, 1986. **20**(1): p. 91-112.

70. Hindar, A., et al., *Effects on stream water chemistry and forest vitality after whole-catchment application of dolomite to a forest ecosystem in southern Norway.* Forest Ecology and Management, 2003. **180**(1-3): p. 509-525.

71. Brown, J.G. and P.D. Glynn, *Kinetic dissolution of carbonates and Mn oxides in acidic water: measurement of in situ field rates and reactive transport modeling.* Applied Geochemistry, 2003. **18**(8): p. 1225-1239.

72. Plummer, L.N., T.M.L. Wigley, and D.L. Parkhurst, *The kinetics of calcite dissolution in CO_2-water systems at 5° to 60°C and 0.0 to 1.0 atm CO_2.* American Journal of Science, 1978. **278**: p. 179-216.

73. Busenberg, E. and L.N. Plummer, *The Kinetics of Dissolution of Dolomite in CO_2-H_2O Systems at 1.5-Degrees-C to 65-Degrees-C and O-Atm to 1-Atm PCO_2.* American Journal of Science, 1982. **282**(1): p. 45-78.

74. Luttge, A., U. Winkler, and A.C. Lasaga, *Interferometric study of the dolomite dissolution: A new conceptual model for mineral dissolution.* Geochimica Et Cosmochimica Acta, 2003. **67**(6): p. 1099-1116.

75. Nakazato, T., et al., *H_2S removal by fine limestone particles in a powder-particle fluidized bed.* Industrial & Engineering Chemistry Research, 2003. **42**(14): p. 3413-3419.

76. Najafpour, G.D. and S. Rezaei, *Chromium and dolomite removal from rotary filter cake in chrome chemical industries.* Journal of the Indian Chemical Society, 2002. **79**(1): p. 99-102.

77. Walker, G.M., et al., *Kinetics of a reactive dye adsorption onto dolomitic sorbents.* Water Research, 2003. **37**(9): p. 2081-2089.

78. Reeder, R.J., *Interaction of divalent cobalt, zinc, cadmium, and barium with the calcite surface during layer growth.* Geochimica Et Cosmochimica Acta, 1996. **60**(9): p. 1543-1552.

79. Astilleros, J.M., et al., *The effect of barium on calcite {10.4} surfaces during growth.* Geochimica Et Cosmochimica Acta, 2000. **64**(17): p. 2965-2972.

80. Astilleros, J.M., et al., *Molecular-scale surface processes during the growth of calcite in the presence of manganese.* Geochimica Et Cosmochimica Acta, 2002. **66**(18): p. 3177-3189.

81. Hemming, N.G., R.J. Reeder, and S.R. Hart, *Growth-step-selective incorporation of boron on the calcite surface.* Geochimica Et Cosmochimica Acta, 1998. **62**(17): p. 2915-2922.

82. Elzinga, E.J. and R.J. Reeder, *X-ray absorption spectroscopy study of Cu^{2+} and Zn^{2+} adsorption complexes at the calcite surface: Implications for site- specific metal incorporation preferences during calcite crystal growth.* Geochimica Et Cosmochimica Acta, 2002. **66**(22): p. 3943-3954.

83. Cheng, L.K., N.C. Sturchio, and M.J. Bedzyk, *Local structure of Co^{2+} incorporated at the calcite surface: An x-ray standing wave and SEXAFS study.* Physical Review B, 2000. **61**(7): p. 4877-4883.

84. Brady, P.V., H.W. Papenguth, and J.W. Kelly, *Metal sorption to dolomite surfaces.* Applied Geochemistry, 1999. **14**(5): p. 569-579.

85. De Leeuw, N.H., J.H. Harding, and S.C. Parker, *Molecular dynamics simulations of the incorporation of Mg^{2+}, Cd^{2+} and Sr^{2+} at calcite growth steps: Introduction of a $SrCO_3$ potential model.* Molecular Simulation, 2002. **28**(6-7): p. 573-589.

86. de Leeuw, N.H. and S.C. Parker, *Modeling absorption and segregation of magnesium and cadmium ions to calcite surfaces: Introducing $MgCO_3$ and $CdCO_3$ potential models.* Journal of Chemical Physics, 2000. **112**(9): p. 4326-4333.

87. De Leeuw, N.H., D.M. Heyes, and J.H. Harding, *Calcite and related materials: Growth and dissolution.* Molecular Simulation, 2002. **28**(6-7): p. 473-474.

88. de Leeuw, N.H. and T.G. Cooper, *A computer modeling study of the inhibiting effect of organic adsorbates on calcite crystal growth.* Crystal Growth & Design, 2004. **4**(1): p. 123-133.

89. Cooper, T.G. and N.H. De Leeuw, *Adsorption of methanoic acid onto the low-index surfaces of calcite and aragonite.* Molecular Simulation, 2002. **28**(6-7): p. 539-556.

90. Nygren, M.A., et al., *Incorporation of growth-inhibiting diphosphates into steps on the calcite cleavage plane surface.* Journal of the Chemical Society-Faraday Transactions, 1998. **94**(24): p. 3685-3693.

91. Cygan, R.T., et al., *Atomistic models of carbonate minerals: Bulk and surface structures, defects, and diffusion.* Molecular Simulation, 2002. **28**(6-7): p. 475-495.

92. Pokrovsky, O.S., J. Schott, and F. Thomas, *Dolomite surface speciation and reactivity in aquatic systems.* Geochimica Et Cosmochimica Acta, 1999. **63**(19-20): p. 3133-3143.

93. Stipp, S.L.S., *Toward a conceptual model of the calcite surface: Hydration, hydrolysis, and surface potential.* Geochimica Et Cosmochimica Acta, 1999. **63**(19-20): p. 3121-3131.

94. Pokrovsky, O.S., et al., *Surface Speciation Models of Calcite and Dolomite/ Aqueous Solution Interfaces and Their Spectroscopic Evaluation.* Langmuir, 2000. **16**: p. 2677-2688.

95. Ohnesorge, F. and G. Binnig, *True Atomic-Resolution By Atomic Force Microscopy Through Repulsive And Attractive Forces.* Science, 1993. **260**(5113): p. 1451-1456.

96. Fenter, P., et al., *Surface speciation of calcite observed in situ by high-resolution X-ray reflectivity.* Geochimica Et Cosmochimica Acta, 2000. **64**(7): p. 1221-1228.

97. Kerisit, S., S.C. Parker, and J.H. Harding, *Atomistic simulation of the dissociative adsorption of water on calcite surfaces.* Journal of Physical Chemistry B, 2003. **107**(31): p. 7676-7682.

98. Kerisit, S. and S.C. Parker, *Free energy of adsorption of water and calcium on the (10-14) calcite surface.* ChemComm, 2004: p. 52-53.

99. Geissbuhler, P., et al., *Three-dimensional structure of the calcite-water interface by surface X-ray scattering.* Surface Science, 2004. **573**(2): p. 191-203.

100. Amira, S., D. Spangberg, and K. Hermansson, *Distorted five-fold coordination of Cu^{2+} (aq) from a Car- Parrinello molecular dynamics simulation.* Physical Chemistry Chemical Physics, 2005. **7**(15): p. 2874-2880.

101. Amira, S., et al., *Molecular dynamics simulation of Fe^{2+} (aq) and Fe^{3+} (aq).* Journal of Physical Chemistry B, 2004. **108**(1): p. 496-502.

102. Amira, S., et al., *Car-Parrinello molecular dynamics simulation of Fe^{3+} (aq).* Journal Of Physical Chemistry B, 2005. **109**(29): p. 14235-14242.

103. Bako, I., J. Hutter, and G. Palinkas, *Car-Parrinello molecular dynamics simulation of the hydrated calcium ion.* Journal of Chemical Physics, 2002. **117**(21): p. 9838-9843.

104. Bleuzen, A., et al., *Water exchange on magnesium(II) in aqueous solution: a variable temperature and pressure O-17 NMR study.* Magnetic Resonance in Chemistry, 1997. **35**(11): p. 765-773.

105. Floris, F.M., et al., *Hydration Shell Structure Of The Calcium-Ion From Simulations With Ab-Initio Effective Pair Potentials.* Chemical Physics Letters, 1994. **227**(1-2): p. 126-132.

106. Floris, F.M., A. Tani, and J. Tomasi, *Evaluation Of Dispersion Repulsion Contributions To The Solvation Energy - Calibration Of The Uniform*

Approximation With The Aid Of RISM Calculations. Chemical Physics, 1993. **169**(1): p. 11-20.

107. Inada, Y., et al., *Hydration structure and water exchange reaction of Nickel(II) ion: Classical and QM/MM Simulations.* Journal of Physical Chemistry A, 2002. **106**(29): p. 6783-6791.

108. Masuda, K., et al., *Structural change of water with solutes and temperature up to 100 degrees C in aqueous solutions as revealed by attenuated total reflectance infrared spectroscopy.* Applied Spectroscopy, 2003. **57**(3): p. 274-281.

109. Matwiyof.Na and H. Taube, *Direct Determination of Solvation Number of Magnesium(2) Ion in Water Aqueous Acetone and Methanolic Acetone Solutions.* Journal of the American Chemical Society, 1968. **90**(11): p. 2796-&.

110. Megyes, T., et al., *Solvation of calcium ion in polar solvents: An X-ray diffraction and ab initio study.* Journal of Physical Chemistry A, 2004. **108**(35): p. 7261-7271.

111. Merrill, G.N., S.P. Webb, and D.B. Bivin, *Formation of alkali metal/alkaline earth cation water clusters, M(H2O)(1-6), M = Li^+, Na^+, K^+, Mg^{2+}, and Ca^{2+}: An effective fragment potential (EFP) case study.* Journal of Physical Chemistry A, 2003. **107**(3): p. 386-396.

112. Naor, M.M., K. Van Nostrand, and C. Dellago, *Car-Parrinello molecular dynamics simulation of the calcium ion in liquid water.* Chemical Physics Letters, 2003. **369**(1-2): p. 159-164.

113. Rodriguez-Cruz, S.E., R.A. Jockusch, and E.R. Williams, *Hydration energies of divalent metal ions, $Ca^{2+}(H_2O)(n)$ (n=5-7) and $Ni^{2+}(H_2O)(n)$ (n=6-8), obtained by blackbody infrared radiative dissociation.* Journal of the American Chemical Society, 1998. **120**(23): p. 5842-5843.

114. Rodriguez-Cruz, S.E., R.A. Jockusch, and E.R. Williams, *Hydration energies and structures of alkaline earth metal ions, $M^{2+}(H_2O)(n)$, n=5-7, M = Mg, Ca, Sr, and Ba.* Journal of the American Chemical Society, 1999. **121**(38): p. 8898-8906.

115. Schwenk, C.F. and B.M. Rode, *Ab initio QM/MM MD simulations of the hydrated Ca^{2+} ion.* Pure and Applied Chemistry, 2004. **76**(1): p. 37-47.

116. Tongraar, A., K.R. Liedl, and B.M. Rode, *Solvation of Ca^{2+} in water studied by Born-Oppenheimer ab initio QM/MM dynamics.* Journal of Physical Chemistry A, 1997. **101**(35): p. 6299-6309.

117. Tulub, A.V. and D.S. Yakovlev, *Structural transformations of the solvation shell of $M(H_2O)(6)$ (2+) (M = Mg, Ca) in the triplet and singlet states during hydrogen elimination and electron attachment.* Russian Journal of Physical Chemistry, 2002. **76**(3): p. 380-383.

118. Vitorge, P. and M. Masella, *A theoretical study of Be, $(H_2O)(n)$ (2+), BeOH, $(H_2O)(n-1)$ (+) and $Be(OH)(2)$, $(H_2O)(n-2)$ aggregates (n=1-6). Incidence of the first hydration shells on the hydrolysis reactions of Be^{2+} and $BeOH^+$ systems.* Chemical Physics Letters, 2000. **332**(3-4): p. 367-374.

119. Guo, J.H., et al., *The interaction of cations and liquid water studied by resonant soft-X-ray absorption and emission spectroscopy.* Journal Of Electron Spectroscopy And Related Phenomena, 2005. **144**: p. 287-290.

120. Kerisit, S. and S.C. Parker, *Free energy of adsorption of water and metal ions on the {1014} calcite surface.* Journal Of The American Chemical Society, 2004. **126**(32): p. 10152-10161.

121. Smedley, P.L. and D.G. Kinniburgh, *A review of the source, behaviour and distribution of arsenic in natural waters.* Applied Geochemistry, 2002. **17**(5): p. 517-568.

122. Smith, A.H., E.O. Lingas, and M. Rahman, *Contamination of drinking-water by arsenic in Bangladesh: a public health emergency.* Bulletin Of The World Health Organization, 2000. **78**(9): p. 1093-1103.

123. Sanchez-Rodas, D., et al., *Arsenic speciation in river and estuarine waters from southwest Spain.* Science Of The Total Environment, 2005. **345**(1-3): p. 207-217.

124. Mahoney, J., et al., *Arsenic readily released to pore waters from buried mill tailings.* Applied Geochemistry, 2005. **20**(5): p. 947-959.

125. Whitmire, K.H., *Organotransition metal compounds with element to transition metal bonds.* Chemistry of Arsenic, Antimony and Bismuth, ed. N.C. Norman. 1998, London: Chapman & Hall.

126. Godfrey, S.M., et al., *Coordination chemistry and solution chemistry.* Chemistry of Arsenic, Antimony and Bismuth, ed. N.C. Norman. 1998, London: Chapman & Hall.

127. Terlecka, E., *Arsenic speciation analysis in water samples: A review of the hyphenated techniques.* Environmental Monitoring And Assessment, 2005. **107**(1-3): p. 259-284.

128. Hollibaugh, J.T., et al., *Arsenic speciation in Mono lake, California: Response to seasonal stratification and anoxia.* Geochimica Et Cosmochimica Acta, 2005. **69**(8): p. 1925-1937.

129. Emett, M.T. and G.H. Khoe, *Photochemical oxidation of arsenic by oxygen and iron in acidic solutions.* Water Research, 2001. **35**(3): p. 649-656.

130. Gault, A.G., et al., *Preliminary EXAFS studies of solid phase speciation of As in a West Bengali sediment.* Mineralogical Magazine, 2003. **67**(6): p. 1183-1191.

131. Arai, Y., D.L. Sparks, and J.A. Davis, *Effects of dissolved carbonate on arsenate adsorption and surface speciation at the hematite-water interface.* Environmental Science & Technology, 2004. **38**(3): p. 817-824.

132. Paktunc, D., A. Foster, and G. Laflamme, *Speciation and characterization of arsenic in Ketza River mine tailings using x-ray absorption spectroscopy.* Environmental Science & Technology, 2003. **37**(10): p. 2067-2074.

133. Arai, Y., D.L. Sparks, and J.A. Davis, *Arsenate adsorption mechanisms at the allophane - water interface.* Environmental Science & Technology, 2005. **39**(8): p. 2537-2544.

134. Roddick-Lanzilotta, A.J., A.J. McQuillan, and D. Craw, *Infrared spectroscopic characterisation of arsenate (V) ion adsorption from mine waters, Macraes mine, New Zealand.* Applied Geochemistry, 2002. **17**(4): p. 445-454.

135. Ladeira, A.C.Q., et al., *Mechanism of anion retention from EXAFS and density functional calculations: Arsenic (V) adsorbed on gibbsite.* Geochimica Et Cosmochimica Acta, 2001. **65**(8): p. 1211-1217.

136. Sherman, D.M. and S.R. Randall, *Surface complexation of arsenic(V) to iron(III) (hydr)oxides: Structural mechanism from ab initio molecular geometries and EXAFS spectroscopy.* Geochimica Et Cosmochimica Acta, 2003. **67**(22): p. 4223-4230.

137. Grafe, M., M. Nachtegaal, and D.L. Sparks, *Formation of metal-arsenate precipitates at the goethite-water interface.* Environmental Science & Technology, 2004. **38**(24): p. 6561-6570.

138. Myneni, S.C.B., et al., *Experimental and theoretical vibrational spectroscopic evaluation of arsenate coordination in aqueous solutions, solids, and at mineral-*

water interfaces. Geochimica Et Cosmochimica Acta, 1998. **62**(19-20): p. 3285-3300.

139. Zacharias, J., et al., *Arsenopyrite and As-bearing pyrite from the Roudny deposit, Bohemian Massif.* Mineralogical Magazine, 2004. **68**(1): p. 31-46.
140. Bednar, A.J., et al., *Field and laboratory arsenic speciation methods and their application to natural-water analysis.* Water Research, 2004. **38**(2): p. 355-364.
141. Cheng, L.W., et al., *X-ray standing wave study of arsenite incorporation at the calcite surface.* Geochimica Et Cosmochimica Acta, 1999. **63**(19-20): p. 3153-3157.
142. Reardon, E.J., C.J. Warren, and M.Y. Hobbs, *Reduction of Trace-Element Concentrations in Alkaline Waste Porewaters by Dedolomitization.* Environmental Science & Technology, 1993. **27**(2): p. 310-315.
143. Kim, M.J. and J. Nriagu, *Oxidation of arsenite in groundwater using ozone and oxygen.* Science of the Total Environment, 2000. **247**(1): p. 71-79.
144. Su, C.M. and R.W. Puls, *Arsenate and arsenite removal by zerovalent iron: Effects of phosphate, silicate, carbonate, borate, sulfate, chromate, molybdate, and nitrate, relative to chloride.* Environmental Science & Technology, 2001. **35**(22): p. 4562-4568.
145. Railsback, L.B., *Patterns in the compositions, properties, and geochemistry of carbonate minerals.* Carbonates And Evaporites, 1999. **14**(1): p. 1-20.
146. Wildner, M., et al., *Sailaufite, (Ca, Na, rectangle)(2)$Mn_3O_2(AsO_4)(2)(CO_3)$center dot $3H_2O$, a new mineral from Hartkoppe hill, Ober-Sailauf (Spessart mountains, Germany), and its relationship to mitridatite-group minerals and pararobertsite.* European Journal Of Mineralogy, 2003. **15**(3): p. 555-564.
147. Gout, R., et al., *Raman spectroscopic study of arsenic speciation in aqueous solutions up to 275 degrees C.* Journal Of Raman Spectroscopy, 1997. **28**(9): p. 725-730.
148. Ramirez-Solis, A., et al., *Experimental and theoretical characterization of arsenite in water: Insights into the coordination environment of As-O.* Inorganic Chemistry, 2004. **43**(9): p. 2954-2959.
149. Pokrovski, G.S., J.M. Beny, and A.V. Zotov, *Solubility and Raman spectroscopic study of As(III) speciation in organic compound-water solutions.*

A hydration approach for aqueous arsenic in complex solutions. Journal of Solution Chemistry, 1999. **28**(12): p. 1307-1327.

150. Pokrovski, G.S., et al., *Experimental study of arsenic speciation in vapor phase to 500 degrees C: Implications for As transport and fractionation in low-density crustal fluids and volcanic gases.* Geochimica Et Cosmochimica Acta, 2002. **66**(19): p. 3453-3480.
151. Pokrovski, G., et al., *Thermodynamic properties and stoichiometry of As(III) hydroxide complexes at hydrothermal conditions.* Geochimica Et Cosmochimica Acta, 1996. **60**(5): p. 737-749.
152. Vansant, F.K. and Vanderve.Bj, *Vibrational Analysis Arsenic Acid And Its Anions.2. Normal Coordinate Analysis.* Journal Of Molecular Structure, 1973. **15**(3): p. 439-444.
153. Vansant, F.K., Vanderve.Bj, and H.O. Desseyn, *Vibrational Analysis Of Arsenic Acid And Its Anions.1. Description Of Raman-Spectra.* Journal Of Molecular Structure, 1973. **15**(3): p. 425-437.
154. Eysel, H.H. and R. Wagner, *Raman Intensities of Liquids - Absolute Scattering Activities and Electrooptical Parameters (Eops) of Arsenate and Selenate Ions in Aqueous-Solutions.* Spectrochimica Acta Part a-Molecular and Biomolecular Spectroscopy, 1993. **49**(4): p. 503-507.
155. Loehr, T.M. and R.A. Plane, *Raman Spectra And Structures Of Arsenious Acid And Arsenites In Aqueous Solution.* Inorganic Chemistry, 1968. **7**(9): p. 1708-&.
156. Tossell, J.A., *Calculation of the UV absorption spectra of As(III) oxo- and thio-acids and anions in aqueous solution and of PF3 in the gas-phase.* Aquatic Geochemistry, 2001. **7**(4): p. 239-254.
157. Tossell, J.A., *Theoretical studies on arsenic oxide and hydroxide species in minerals and in aqueous solution.* Geochimica Et Cosmochimica Acta, 1997. **61**(8): p. 1613-1623.
158. Tossell, J.A., *Calculation of the visible-UV spectra of As and Sb sulfides and polysulfides.* Abstracts of Papers of the American Chemical Society, 2003. **225**: p. 026-GEOC.
159. Tossell, J.A., *Calculation of the visible-UV absorption spectra of hydrogen sulfide, bisulfide, polysulfides, and As and Sb sulfides, in aqueous solution.* Geochemical Transactions, 2003. **4**: p. 28-33.

160. Francesconi, K.A. and D. Kuehnelt, *Determination of arsenic species: A critical review of methods and applications, 2000-2003.* Analyst, 2004. **129**(5): p. 373-395.

161. Nordstrom, D.K. and C.N. Alpers, *Negative pH, efflorescent mineralogy, and consequences for environmental restoration at the Iron Mountain Superfund site, California.* Proceedings Of The National Academy Of Sciences Of The United States Of America, 1999. **96**(7): p. 3455-3462.

3. THEORY AND METHODOLOGY

"The belief that there is only one truth and that oneself is in possession of it seems to me the deepest root of all evil that is in the world." Max Born (1882-1970).

A number of computational methods have been used in this study and this chapter discusses their details. This chapter presents merely an overview, in the interests of brevity and applicability, and more detailed information is available in the literature cited and the contents of the bibliography.

Initially, it is important to discuss the foundation upon which these methods are built, the Born-Oppenheimer Approximation. The Born-Oppenheimer Approximation is the fundamental premise upon which most computational chemistry methods are based; without it, computational modelling of complex systems would not be possible. At the level at which chemists are interested, an atom is comprised of electrons and nuclei, the latter of which, in turn, consists of protons and neutrons. The nuclear sub-atomic particles can be reduced further into combinations of quarks and anti-quarks. However, for the purposes of studying the behaviour of materials, reductionism need only proceed so far as protons and neutrons comprising the nucleus, and electrons.

The Schrödinger equation, which relates the wavefunction of a particle to its energy, can only be solved exactly for systems with two constituents or fewer, such as the hydrogen atom. In order to solve it for larger systems, it is necessary to make approximations. As mass of a proton is 1800 times that of an electron, the nucleus of an atom is considerably larger in mass than the electrons orbiting it. The velocity of the electrons is also much faster than that of the nucleus, so the electrons can respond effectively instantaneously to any motion of the larger, heavier nuclei. It follows that the motion of the nuclei can be separated from the motion of the electrons, giving us the Born-Oppenheimer Approximation. So, when considering the atomic motion due to atomic interactions, the motion of the nuclei can be considered to dictate the motion of the atom, as the electrons

will so readily respond to the changes in co-ordinates, and the electronic wavefunction can be solved for any given nuclear geometry.

3.1. Electronic Structure Methods

3.1.1. Background

Fundamentally, Density Functional Theory (DFT) and *ab initio* methods, such as Hartree-Fock (HF) and post-Hartree-Fock (Møller-Plesset N^{th} Order etc.) methods, all calculate the energy of a system with respect to the electronic density (DFT) or the electronic wavefunction (HF, MP2, MP3).

The Schrödinger equation is fundamental in quantum mechanics, and relates the wavefunction, Ψ, to the energy of a system through the Hamiltonian operator, $\hat{H}$. The time independent version of the Schrödinger equation is:

$$\hat{H}\Psi = E\Psi \tag{3.1}$$

where:

$$\hat{H} = -\frac{\hbar^2}{2m}\nabla^2 + V \tag{3.2}$$

The kinetic energy operator, the first term on the r.h.s. of equation (3.2), contains the mass, m, of the particle upon which wavefunction the Hamiltonian will operate and $\hbar$, which is Plank's constant divided by 2π. The second term, V, is the potential energy operator, and in the application of the Schrödinger equation to chemical systems this describes the interaction of the electrons with the nucleus. The application of the Born-Oppenheimer approximation allows for the solution of the Schrödinger equation for a certain set of nuclear coordinates. From this premise, the ground state energies of each configuration can be found through exploration of the potential energy surface of the system to find the coordinates that give the lowest energy.

The energy, then, can be calculated thus:

$$E = \frac{\int \Psi^* \hat{H} \Psi d\tau}{\int \Psi^* \Psi d\tau}, \tag{3.3}$$

where the wavefunction is integrated over all space. It is not possible to find an exact solution for the wavefunction in many-body problems, so approximations must be made in order to find the energy of the system and the electronic distribution. The following sections explore the different methods used to calculate the energy, either from an approximation to the wavefunction or from the electron density of the system. A fundamental principle when identifying the best approximation to the wavefunction or the electron density is that of the 'variation theorem'. The variation theorum states that the energy of the true wavefunction will always be lower than the energy of an approximation to the wavefunction, and so the wavefunction that gives you the lowest energy is the best approximation. Variational methods may also be applied to other quantities that can be used to calculate the energy, such as the electron density.

In practice, the energy for a given set of nuclear coordinates is broken down into the nuclear-nuclear interactions, the interaction between the electrons and the nuclei, the Coulombic interaction between the electrons, and the exchange and correlation terms for the electrons. The exchange term is a correction to the Coulombic interaction, removing the electronic self-interaction and the correlation term quantifies the repulsion between two localised electrons in proximity to each other, which results in a correlation of their positions.

3.1.2. Hartree-Fock and Post-HF methods

In Hartree-Fock theory, each electron is considered to move in an average potential brought about by the other electrons and the nuclei in the system. HF theory is built upon Hartree's variational Self-Consistent Field (SCF) method, where electron-electron interactions are ignored and separate Schrödinger equations are written for a series of one-electron orbitals,

where the effect of the surroundings, i.e.: the other electrons and the nuclei in the system, are represented by the average of their potential energy. Fock [1] introduced the antisymmetry of the orbitals by writing them as Slater determinants. The initial guess to the molecular orbitals in which to house the system's electrons is written as a Linear Combination of Atomic Orbitals (LCAO), which comprises of weighted one-electron orbitals. The one-electron functions in the LCAO are known as 'basis functions', and their nature will be discussed further in section 3.1.1.4. The Schrödinger equations are solved, with the Fock operator incorporated, with each step improving the initial approximation of a uniform potential energy until self-consistency is achieved. The Fock operator, $\hat{F}$, consists of three operators: the core Hamiltonian operator, $\hat{H}$, which describes the effect of a single nucleus on a single electron; the Coulomb operator, $\hat{J}$, which gives the average potential due to an electron in a specific molecular orbital (MO); and the exchange operator, $\hat{K}$, which acts upon a specific spin orbital and describes the exchange of the electrons in the system:

$$\hat{F}(1) = \hat{H}^{core}(1) + \sum_{j=1}^{N}\left[\hat{J}_j(1) - \hat{K}_j(1)\right] \qquad (3.3)$$

The HF method neglects to adequately account for the energetic contribution of electron correlation, in fact electron correlation is defined as the difference between the total energy of a system and the full HF energy. Electrons will, due to their charge, avoid each other, which leads to a correlation in their positions at any one instant. In HF, each electron exists in an average field of all the other electrons, and the instantaneous nature of the correlation effect cannot be incorporated into the theory. This can lead to errors of the magnitude of around one electron volt, although in these calculations there can often be a fortuitous cancellation of errors. The use of post-HF methods can incorporate correlation effects into computational calculations. These methods were not used in the present work, and as such a detailed discussion of them will not be included, although further detail can be found in Leach [2] and Cramer [3]. Suffice it to say that, in the post-HF Configuration Interaction (CI) approach, various excited configurations (singles – CIS, doubles – CID, or both - CISD) are included in linear combination with the ground state configuration to give an

improved approximation to the wavefunction, allowing for a description of correlation. Alternatively, Many-body Perturbation Theory states that the true Hamiltonian operator is the zeroth order Hamiltonian, plus a perturbation times a coefficient, λ, that is comprised of energies that are the eigenvalues of the wavefunction multiplied by λ to various powers, which relate to the different orders of electronic excitations included for the system. The HF energy is the sum of the zeroth and first order energies, and improvements to this value can be made by incorporating energies of higher orders, leading to, for example, the computationally expensive second and third order Møller-Plesset methods (MP2, and MP3 respectively), among others.

3.1.3. Density Functional Theory

Density Functional Theory (DFT) bypasses the calculation of the multi-electronic wavefunction and calculates the system's energy from its electron density. The theory rests, fundamentally, on the building blocks that were laid down in 1964 by Hohenberg and Kohn, who linked the external potential and the electron density through a functional of the density. They proved that the ground state density uniquely determines all the properties of a system, and the global minimum of the energy that is found from the ground state density is the ground state energy [4]. Hohenberg-Kohn theory, however, proposes no means of calculating the system's properties from the density, i.e.: it suggests no way to derive a functional to act upon the density. A year later, Kohn and Sham [5] introduced the idea that the electron density of the true system is the same as that of an auxiliary system, which contains electrons acting independently, plus a correction term that accounts for the exchange correlation potential. The energy functional is given as:

$$E[\rho(\mathbf{r})] = T_s[\rho(\mathbf{r})] + \int V_{ext}(\mathbf{r})\rho(\mathbf{r})d\mathbf{r} + E_{II} + E_{Hartree}[\rho(\mathbf{r})] + E_{XC}[\rho(\mathbf{r})] \qquad (3.4)$$

T_s is the independent-particle kinetic energy, a functional of the system's orbitals. The second term gives the interaction of the electrons in external potential, V_{ext}, created by the nuclei, E_{II} is the electrostatic interaction between the nuclei, $E_{Hartree}[\rho(\mathbf{r})]$ is the Hartree electrostatic energy, the Coulombic energy between the electrons, and $E_{XC}[\rho(\mathbf{r})]$ is the

contribution from electronic exchange and correlation, plus the difference in the kinetic energy between the auxiliary and the true, interacting, many-body system. DFT is an iterative procedure like HF, but in this case the procedure starts with a guess at the electron density over the system, which in turn gives the Kohn-Sham orbitals, from which a new, improved density can be calculated.

The Kohn-Sham equations, the solution of which give the individual orbital energies, ε_i, are:

$$\left\{-\frac{\nabla_1^2}{2}-\left(\sum_{A=1}^{M}\frac{Z_A}{r_{1A}}\right)+\int\frac{\rho(\mathbf{r})}{r_{12}}d\mathbf{r}_2+V_{XC}[\mathbf{r}_1]\right\}\psi_i(\mathbf{r}_1)=\varepsilon_i\psi_i(\mathbf{r}_1), \tag{3.5}$$

φ_i, are the one-electron orbitals that comprise the auxiliary system, spread over M nuclei. V_{XC} is the exchange-correlation potential:

$$V_{XC}[\mathbf{r}_1]=\left(\frac{\delta E_{XC}[\rho(\mathbf{r})]}{\delta\rho(\mathbf{r})}\right). \tag{3.6}$$

Were the exact exchange-correlation term known, the exact energy for the system could also be found, so the most suitable form for the exchange-correlation functional is the focus of much research [6-13].

The exchange-correlation energy can be assumed to be a functional of either the spatial coordinates alone, which gives rise to the Local Density Approximation (LDA), or dependant on the coordinates and the gradient of the density, known as the Generalised Gradient Approximation (GGA). When applied to a closed-shell system, the LDA is equal to the Local Spin Density Approximation (LSDA). Both approximations treat the local density as a uniform electron gas, so that the exchange correlation energy is expressed only in terms of coordinates. The LSDA splits the electron density in two with respect to the electronic spin (as is the case in unrestricted HF methods). Importantly, however, the density of the uniform gas is allowed to vary for each value of **r**. The LDA and LSDA are

generally found to underestimate exchange and overestimate correlation, leading to over-bonding in the system. Various GGA approaches exist, and the best method to choose between them is through comparison of results from experiment or high-level wavefunction-based calculations. Some GGA functionals are gradient-corrected LDA functionals, eg: B88 [14] or PW86 [15]; some provide new formulations for the exchange and the correlation functionals, eg: LYP [16]. A further development to DFT functionals is the use of hybrid functionals. Hybrid functionals approximate the total exchange-correlation energy to have contributions from the exact HF exchange energy, calculated from the Kohn-Sham orbitals (the non-interacting system of electrons), and from the exchange and correlation energies from various GGA or LDA functionals, the particular components depending on the choice of hybrid functional. The various coefficients in these functionals are parameterised according to a variety of experimental data.

3.1.4. Basis Sets

The electron density of a system is described through the population of basis functions, defined in the input for a calculation. In order to calculate the electron density and thus the energy of a system without error for a specific functional, it would be necessary to include an infinite number of basis functions on each atom. As this is not practically possible, approximations must be made, which necessarily introduce some error into the calculation. The basis sets must be chosen to minimise these errors in the description of the molecular wavefunction. Even approaching a complete basis set is prohibitively expensive, and so, energies from QM calculations must be viewed in a relative context in order to have meaning. The most common type of basis set is the atom-centred basis set, which was used in this study and are discussed below.

There are two main types of atom centred basis functions, Slater Type Orbitals (STOs) and Gaussian Type Orbitals (GTOs). Though they provide high-quality calculations of atomic and diatomic systems, the integrals of STOs can prove difficult to evaluate analytically for more complex systems. It is common practice instead to use GTOs, which are based on

Gaussian functions, multiplied by integer powers of the coordinates and normalised. In Cartesian coordinates, the general form is:

$$X_{\alpha,l_x,l_y,l_z}(x,y,z) = Nx^{l_x}y^{l_y}z^{l_z}e^{-\alpha r^2}. \qquad (3.7)$$

The sum of the integer powers determines the orbital anglular momentum (s, p, d etc.). While more analytically convenient, GTOs have the drawback that a single Gaussian function is inadequate to describe the shape of an atomic orbital accurately. Unlike STOs, GTOs do not form a cusp at the nucleus, instead they have zero gradient at this point (Fig. 3.1), and they decay too rapidly with respect to radius from the nucleus, as r^2 rather than r. In general, a linear combination of three primitive Gaussians is required to give as adequate a representation of the orbital as a STO. The resulting Gaussian function is known as a contracted GTO.

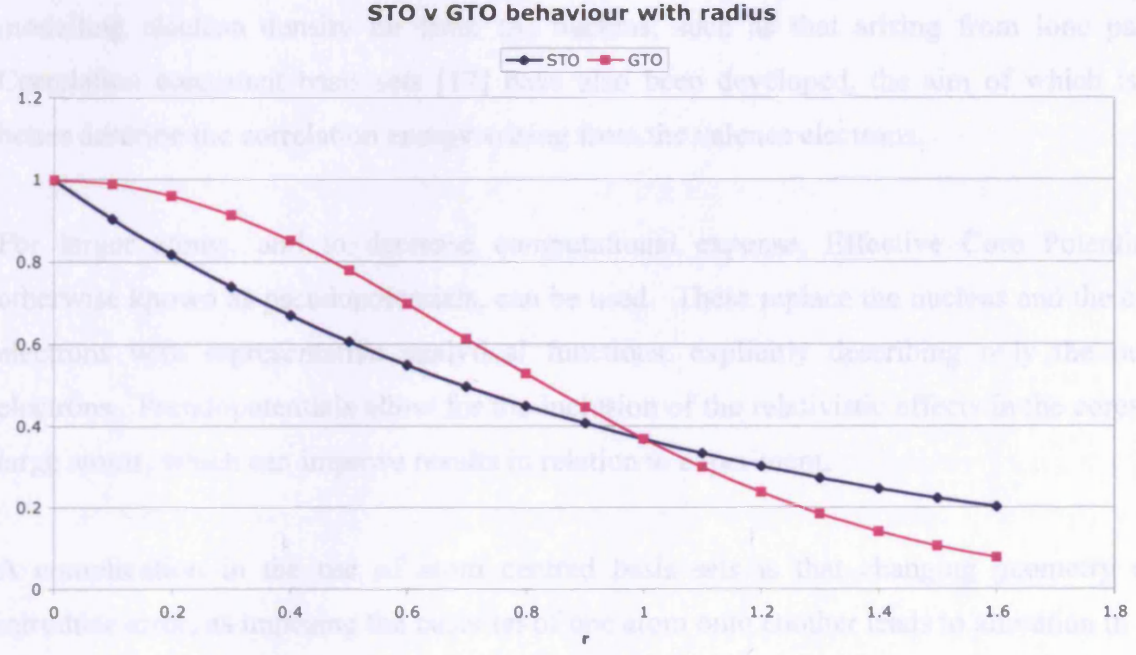

Figure 3.1: Simplest representation of the shape of a STO and a GTO by plotting the behaviour of exponential functions of x, where $x = r$ and $x=r^2$

The various basis sets available differ in the number of functions they use to represent the orbitals in the system. Minimal basis sets, such as STO-3G, STO-4G etc., provide enough orbitals to accommodate all the electrons in the atoms and no more. The "3" and "4" in the notation denote the number of Gaussians used to form each atomic orbital. To overcome some of the limitations of a minimal basis set, such as the inability to describe the anisotropy of electron distribution and the limited ability of the orbitals to expand and contract, multiple Gaussian functions can be used for each orbital. Doubling the number of functions gives rise to a *Double Zeta* (DZ) basis set, tripling the number yields *Triple Zeta* (TZ), and so on. For larger atoms, the number of functions is sometimes only multiplied in this way for the valence electrons, leading to split valence basis sets, such as DZV and TZV. Other split valence basis sets are 3-21G, 6-31G etc., where the latter two numbers describe the number of contracted and diffuse Gaussians used to form the valence orbitals. To better describe the behaviour of orbitals in a molecular environment, it is often necessary to incorporate polarisation functions, corresponding to nearby, empty atomic orbitals. Diffuse functions can also be incorporated, and are important in accurately modelling electron density far from the nucleus, such as that arising from lone pairs. Correlation consistent basis sets [17] have also been developed, the aim of which is to better describe the correlation energy arising from the valence electrons.

For larger atoms, and to decrease computational expense, Effective Core Potentials, otherwise known as pseudopotentials, can be used. These replace the nucleus and the core electrons with representative analytical functions, explicitly describing only the outer electrons. Pseudopotentials allow for the inclusion of the relativistic effects in the cores of large atoms, which can improve results in relation to experiment.

A complication in the use of atom centred basis sets is that changing geometry can introduce error, as imposing the basis set of one atom onto another leads to alteration in the quality of the basis set for that atom, with the effect that not all atoms are being described at the same level of theory, causing discrepancies in relative energies. This is an artefact of the necessity of incomplete atomic basis sets, and is known as the Basis Set Superposition Error; it results in over-binding in the area in which the basis sets overlap. The BSSE can

be counteracted by the counterpoise correction method, though this method will always overestimate the extent of the BSSE. In general practice, the BSSE is minimised by the use of adequately sized basis sets. Alternatively, numerical basis sets are sometimes used, which solves atomic DFT equations for the radial part of each AO numerically. This allows for the description of the molecule to be analysed with respect to its constituent atoms and minimises the BSSE.

3.2. Empirical Potential Methods

Empirical methods are so called because they are, in some way, reliant upon empirical evidence, i.e.: they are fitted to experimental data, or to high-level calculations. While DFT is an electronic structure method, empirical nature is sometimes introduced into the method as functionals are often optimised to experimental data.

3.2.1. Force Field Methods and Energy Minimisation

When modelling large systems, or carrying out long timescale molecular dynamics simulations, the computational cost of calculating the electronic wavefunction for each component of the system can prove prohibitive. In such cases it is practical to adopt an alternative approach, whereby the atoms or ions in a system are treated as indivisible units, replacing the calculation of the contributions from subatomic particles with interatomic potentials, which describe the interactions of the atom or ion, as a whole, with its environment. For static energy calculations, just as in *ab initio* methods, the total energy of the system is calculated with respect to the coordinates of its components. The total energy is computed by the addition of the contributions from all the various interactions within the system, described by the potentials.

Empirical potentials, implemented in the General Utility Lattice Program (GULP 3) [18], have been used in this work for the investigation of impurities at dolomite surfaces. The standard practise for creating potentials is to fit different potential parameters to data from

experiment, and sometimes from quantum mechanical calculations when experimental information is unobtainable or incomplete, so that the potential describes correctly the behaviour of the system. Potentials need to be tailored to describe the behaviour of systems under different conditions, such as at different pressures or different co-ordination environments. There are two types of interactions that need to be included in the calculation of the energy of a system: the long-range interactions of ions at a distance, and the short-range interactions. A discussion follows of the different interactions and the various means of calculating their effect on the total system.

3.2.1.1. The Born Model of Solids

As an introduction to the principles behind interatomic potential methods, it is useful to consider one of the oldest and best known models, the Born model of solids[19]. Intuitively, the expression for the potential energy of an ionic, or polar, solid system is the summation of the incremental many-body interactions, thus:

$$U_{Tot} = U_0 + \sum_{i=1}^{N}\sum_{j=1}^{N} \upsilon_{ij}(r) + \sum_{i=1}^{N}\sum_{j=1}^{N}\sum_{k=1}^{N} \upsilon_{ijk}(r) + \dots , \qquad (3.8)$$

Equation 3.8 shows the contributions from pairwise and three-body interactions, as well as the self-energies of each species, which are equal to zero for forcefield methods. The Born model restricts equation (3.8) to only the two-body interactions, comprised of the attractive long-range interactions of the electrostatic interaction, represented by Coulomb's law, and short-range interactions, V_{ij}:

$$U_{Tot} = \sum_{i=1}^{N}\sum_{j=1}^{N}\left(\frac{q_i q_j}{4\pi\varepsilon_0 r_{ij}} + V_{ij}\left(r_{ij}\right)\right) \qquad (3.9)$$

These two contributions will be discussed in the following sections, and the concept initiated by Born will be expanded upon to encompass current methods.

3.2.1.2. Long-range Interactions

Long-range interactions, as the name suggests, describe the interactions between different components of the system over long distances. In an ionic system, these arise due to electrostatic interactions of the charged species in the system. The force acting on a point charge q_i due to the influence of a second point charge q_j, at a separation of r_{ij}, is given by Coulomb's law (the first term in equation (3.9)):

$$U_{ij}^{Coulomb} = \frac{kq_iq_j}{r_{ij}}, \tag{3.10}$$

where, $k = 1/4\pi\varepsilon_0$, Coulomb's constant, expressed in terms of ε_0, the permittivity of space. Coulomb's law is the expression of the fact that like charges repel each other and opposite charges attract. The subsequent force acts along a vector between the charges involved, and decays inversely with the distance between them. For an infinite system, as created by the inclusion of periodic boundary conditions (PBCs), which is the case for all solid-state calculations, the Coulomb interaction becomes difficult to evaluate. The system extends to infinity in 3-dimensions and it is necessarily the case under these conditions that the number of interacting species will increase with distance just as the interactions between the charges decay. It is important to calculate accurately the degree to which both of these aspects change in relation to each other to determine their contribution to the total energy of the lattice. This problem must be dealt with effectively in order to evaluate the long-range forces computationally.

For non-ionic systems, the long-range forces comprise of the interactions of permanent dipoles or quadrupoles with each other, and with the dipoles that they induce in the species with which they interact.

3.2.1.2.1. Evaluating the Coulomb Interaction

The Coulomb interaction, over all the cells in a periodic system, is evaluated differently for 3-dimensional and 2-dimensional periodic systems. The formulae used for the calculations

will not be derived here, as these have been extensively discussed elsewhere [2, 3, 18]; however an outline of the different methods used will be given. The 3-dimensional calculation in GULP uses the Ewald summation[18, 20], and the 2-dimensional case uses the Parry summation [18, 21]. In order to sum the Coulomb interaction over 3-dimensions using the Ewald summation, conditions of charge neutrality and zero dipole are enforced on the system. A Laplace transform is applied to the calculation, and the overall effect of these measures equates to imposing a spherical Gaussian of opposite charge on the point charges in real space and applying Gaussians of exactly opposite charge to the first set to the ions in reciprocal space. The application of an Ewald summation speeds up convergence of the Coulomb interaction and removes the problem of conditional convergence, where the positive and negative components of the sum are both divergent when calculated separately. A correction factor must be included to subtract the interaction of each Gaussian with itself.

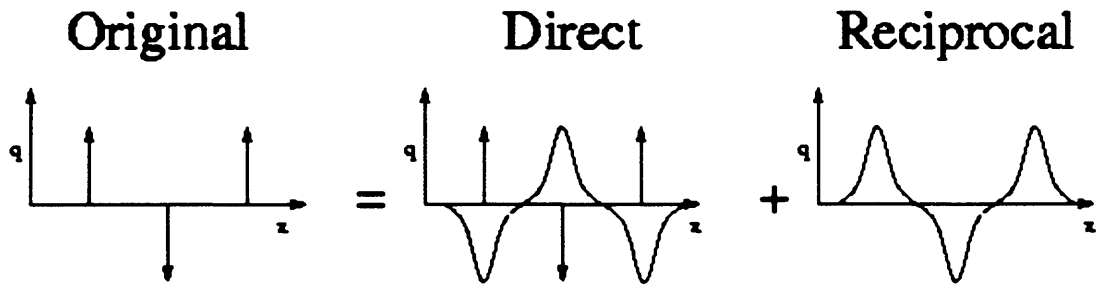

Figure 3.2: Pictorial representation of the Ewald Summation method [22]

It is possible to calculate the Coulomb interaction for a system with a dipole by adding a correction factor to the Ewald result. It is also possible to calculate the energy of a system with net charge, which can be effected by the addition to the system of a uniform background charge of equal magnitude but opposite charge, and subsequent correction for this compensatory charge. This allows calculations of charged defect energies using the supercell method.

The Parry summation is used to calculate the electrostatic interaction for surfaces, which repeat in two dimensions along the x and y directions, having depth in the z direction. This

entails summing the potential from a series of charged sublattices, which lie in a plane with the surface at different values of z, in order to reproduce the electrostatic potential for the system [23].

An alternative to the above summations, applicable to systems of any dimensionality, is the Wolf summation [24], which sums over pair-wise interactions in real space. The system incorporates a method that allows for charge neutrality, once the pair potentials have been truncated, and which yields a constant Coulombic value regardless of the order in which the pair-wise interactions are included.

3.2.1.3. Dispersion Interaction

The dispersion, or London, force, like the electrostatic energy, is a non-bonded interaction. Unlike the Coulomb interaction, it has little effect at very long distances. At intermediate inter-atomic distances, however, the dispersion interaction is attractive, and contributes to the overall energy of the system. The dispersion interaction is the longer-range component of the non-permanent components of the van der Waals' interaction.

The idea of induced dipoles or quadrupoles arises from quantum mechanics. Electrons in their ground state, even at absolute zero, exhibit a zero point energy resulting from fluctuations in the electronic density. These fluctuations have a characteristic frequency, and result in an electromagnetic wave, or "virtual photon", analogous to photons propagated by electronic transitions between excited states. The field associated with the production of these virtual photons is such that it will affect nearby electron clouds, polarising them and creating the instantaneous dipole-instantaneous dipole interaction that characterises the London force. The resultant interaction is slightly attractive due to the small charge differences, and explains the attractive behaviour of the noble gases.

The Drude model for dispersive interaction shows that the energy arising from dipole-dipole interactions varies as r_{ij}^{-6} in 3-dimensions [2]. The related attractive force varies as

r_{ij}^{-7} [25]. If dipole-quadrupole and quadrupole-quadrupole interactions are then included, the total dispersion interaction is given as:

$$U_{ij}^{dispersion} = -\frac{C_6}{r_{ij}^6} - \frac{C_8}{r_{ij}^8} - \frac{C_{10}}{r_{ij}^{10}} \ldots \tag{3.11}$$

where, C_6, C_8 etc. are constants. However, for most systems it is adequate to calculate only the first term; notable exceptions are certain metallic systems [26].

3.2.1.4. Short-range interactions

Short range interactions, sometimes referred to as exchange forces, describe the repulsive behaviour of atoms or ions at close proximity. These, along with the dispersion interaction, are modelled by interatomic potentials, the natures of which vary for different systems. For most systems, it is adequate to include terms up to and including four-body interactions in order to model it to a sufficient degree of accuracy. There follows a discussion of the various different forms of short-range interatomic potentials for two-, three- and four-body interactions.

3.2.1.4.1. Two-body Potentials

There are a number of forms available for two-body potentials, which describe the interaction of neighbouring species, whether atoms within a molecule or ions. One of the most commonly used is the Buckingham potential, which takes the form,

$$U_r = A\exp\left(-\frac{r_{ij}}{\rho}\right) + \frac{C_6}{r_{ij}^6}, \tag{3.12}$$

The removal of the attractive C_6 term, which models the dispersion interaction, gives rise to the Born-Mayer potential. A, ρ and C are parameters that are fitted in order to describe correctly the interaction of the two species that are being described, where A can be understood to model the effective size of the atom or ion, and ρ its compressibility. Obviously, C is fitted to model the London interaction accurately. The exponential term

describes the repulsion between neighbouring species at a distance r_{ij} from each other. The argument for the exponential form of the repulsive part of the potential is founded in the distribution of the electron density. Repulsion between atoms arises from the overlap of the electron densities described by the wavefunctions, and the electron densities diminish roughly exponentially with increasing distance from the nucleus.

The interatomic repulsion can also be modelled as the inverse of the atomic separation, as in the Lennard-Jones potential:

$$U_{ij} = 4\varepsilon\left(\frac{\sigma}{r_{ij}^{m}} - \frac{\sigma}{r_{ij}^{6}}\right), \tag{3.13}$$

The Lennard-Jones is sometimes called the "12-6" potential, because typically m = 12. The potential has an attractive tail at long distance but becomes rapidly repulsive at closer proximity. Compared to the Buckingham potential, the Lennard-Jones potential better describes interactions at very close distances, as the repulsive term rapidly increases for a small value of r_{ij}. In the Buckingham potential, at very small distances, the dispersive r^{-6} term dominates, which can cause the structure to collapse in on itself if a poor starting configuration is chosen. However, at reasonable distances the Buckingham potential's exponential term provides a better description of interatomic repulsion.

Morse potentials are often employed to describe the bond stretching between atoms in a covalently bonded molecule. It takes the form:

$$U_{ij} = D_{eq}(1 - \exp(-a(r - r_e)))^2, \tag{3.14}$$

where, D_e is the dissociation energy and r_e is the equilibrium bond length. The 'a' parameter describes the width of the potential well, and is related to the dissociation energy by:

$$a = \sqrt{\frac{k}{2D_{eq}}}. \tag{3.15}$$

The form of the Morse potential describes the fact that it is harder to compress a bond than to stretch it and reproduces fairly accurately the behaviour of a bond up to roughly 10 kcal/mol above the minimum for the bond length [27].

3.2.1.4.2. Three-body Potentials

Three-body potentials are often included when modelling covalently bonded molecules to describe the bond-bond repulsion that gives rise to molecular shape, which has been the case in this work. They are sometimes also included for ionic materials, to better describe the ionic interactions by describing van der Waals'-like contributions due to triplets of oscillating dipoles. In this work the three-body potential takes the form:

$$U_{ij} = 0.5k_e(\theta - \theta_0)^2 \tag{3.16}$$

where θ is the angle between the vectors and θ_0 is the equilibrium value of angle.

3.2.1.4.3. Four-body Potentials

Four-body potentials describe the torsion angle of a molecule. They take a variety of different forms, as do the two- and three-body potentials. They describe either the rotation of groups around a central bond, or the out-of-plane bending of a planar molecule. The out-of-plane four-body potential has the form:

$$U_{12} = k_2 d^2 + k_4 d^4 \tag{3.17}$$

where d is the out-of-plane distortion.

3.2.1.4.4. Treatment of Polarisability

The most common treatment of the polarisability of atoms or ions is through the use of the shell model [28]. Conceptually, the model describes the polarisability of an ion by connecting, via a spring, the point charge of the core, which holds all the mass, to a

massless shell. The core describes the nucleus and inner electrons of the atom or ion, the shell describes the outer electron(s), which would be affected by polarisation. The coordinates of the shell and the core are allowed to vary separately during the simulation. The degree to which the shell coordinate is allowed to vary from the core position is constrained by the value of the spring parameter, k, the force constant for the harmonic spring. The force constant is related to the polarisabilty, α, through the charge on the shell, q_s, by the relation:

$$\alpha = \frac{q_s^2}{k}, \tag{3.18}$$

The shell and core are assigned separate charges for the purposes of the calculation. For a negative ion the core is positive and the negative charge is carried on the shell. For a positive ion it can be the case that both the core and shell are positive. There is no repulsion between cores and shells on the same atom in such a case as they are always Coulombically screened from each other. Most short-range potentials will act upon the shell, so that the degree of polarisation becomes dependant upon the immediate vicinage.

3.2.1.4.5. Potential Cut-offs

All potentials used must be truncated, as it is not possible to calculate the potential energy for potentials acting to infinity. This is often done by means of a radial cut-off, after which interactions between species are ignored. It is important to choose a reasonable value for the cut-off, as one that is too small will result in neglect of important interatomic forces, and one that is too large will require unnecessary extra computational expense for no improvement in accuracy. The inclusion of a radial cut-off will often lead to some degree of discontinuity in the energy arising from the described interaction.

Should problems arise as a result of the use of a cut-off, the discontinuity in the energy can be smoothed. One means of achieving this is the use of a shifted potential, where a constant term, equal to the value of the potential at the cut-off radius, is subtracted from the

potential at all values within the sphere over which the potential is calculated. Obviously, this method leads to deviation of the potential from its original, fitted value. Additionally, discontinuities in the forces, arising from the cut-off, must also be counteracted by the inclusion of a linear term to the potential. As such this method is seldom used when the calculation of thermodynamic properties is desired.

Alternatively, the potential may be multiplied by a switching function, in order to resolve the problem of discontinuity. The switching function takes a polynomial form that acts upon distance within the cut-off radius. The inclusion of a switching function can, however, affect the value and position of minimum energy structures, and as such is not always a viable solution to the problem arising from the use of potential cut-offs.

In preference to the two aforementioned solutions, it is most often the case that the potential is tapered between two cutoff radii. The potential acts as usual up to the distance denoted by the smallest cutoff. Between this and the larger radius, a switching function is applied to the potential. This switching function is such that it varies from 1 to 0 between the smaller and larger cutoff radii respectively. The switching function can be tailored to ensure that there are no discontinuities in either the energy or the forces deriving from the potential to which this method is applied.

3.3. Static Geometry Optimisation Calculations

Geometry optimisations are a family of methods for minimising the energy of a system with respect to its atomic or ionic coordinates. The different approximations for deriving the energy of the system of interest have been discussed in previous sections. The methods are applicable to both geometry optimisation and to simulation techniques like Molecular Dynamics, which will be discussed in Section 3.4.

3.4. Molecular Dynamics

Molecular dynamics is a deterministic statistical technique that allows the modeller to sample successive, time-correlated configurations of the system that is under investigation, outputting a trajectory for the calculation. The trajectory of the simulation is calculated through the integration of Newton's second law of motion to give the positions, velocities and accelerations as a function of the time. The system can be studied using any of the methods mentioned in Sections 3.1 and 3.2. Molecular dynamics calculations can be used to glean many different thermodynamic properties about the system by taking the time average of the property as a function of the variation in positions and momenta over the duration of the calculation. Were the sampling of phase space complete during any calculation, these thermodynamic properties would be exact. However, for most systems phase space is prohibitively large for complete sampling, so sufficient samples must be taken to minimise the errors in the desired quantities. The calculation of the time average is mathematically unwieldy, and the use of statistical mechanics allows us to replace it with an ensemble average, which is the average over a large number of simultaneously considered conformations of the system containing N atoms:

$$\langle A \rangle = \iiint \iiint d\mathbf{p}^N d\mathbf{r}^N A(\mathbf{p}^N, \mathbf{r}^N) \rho(\mathbf{r}^N, \mathbf{r}^N), \tag{3.17}$$

where **p** are the momenta and **r** are the positions of the atoms in the system, A is the thermodynamic property of interest and ρ is the probability of finding a configuration with atoms at positions **r**, with momenta **p**, known as the probability density. The probability density changes form with variations in the ensemble chosen for the calculation. Molecular dynamics calculations are carried out over a time period divided into a certain number of time-steps, typically of around 0.5-1fs in length. The average of the required property then becomes:

$$\langle A \rangle = \frac{1}{M} \sum_{i=1}^{M} A(\mathbf{p}^N, \mathbf{r}^N), \tag{3.18}$$

where M is the number of steps taken.

The size of the time-step is determined by the timescale of the shortest event that the user desires to observe. In the case of proton transfer, which is rather rapid, a time-step greater than 0.5 fs can lead to erroneous statistics. The molecular dynamics run must go through a period of equilibration, the "equilibration phase", before the statistics from the calculation can be sampled reliably, after which time it enters the "production phase". Typically, the equilibration phase is over, once the property to be varied reaches a roughly constant value.

There are a number of common ensembles used in molecular dynamics calculations, and their choice depends on the equilibrium state desired for the simulation. The different ensembles, the properties of the system that they keep constant, and the respective equilibrium state are all listed in Table 3.1.

Ensemble Name	Fixed Properties	Equilibrium State
Canonical	N, V, T	Minimum Helmholtz free E
Microcanonical	N, V, E	Maximum Entropy
Isothermal-isobaric	N, T, P	Minimum Gibbs' function
Grand canonical	μ, V, T	Maximum P x V

Table 3.1: Molecular dynamics ensembles

In this work, molecular dynamics runs have been carried out using a canonical ensemble. The temperature can be kept constant either by directly scaling the velocities at each step, or by using the Nosé-Hoover method, where the system contains a heat bath with which energy is exchanged in order to maintain the temperature.

Aside from thermodynamic properties, molecular dynamics simulations provide other useful information about the system. In simulations of liquids it is often desirable to understand the ordering of the system, or the number of molecules in the solvation shells of a solute, in which case it is useful to calculate the Radial Distribution Function (RDF). The RDF gives the average number of particles of a certain type that are present in a shell of

thickness, δr, at a distance r from the atom for which the RDF is required. The RDF is expressed in terms of $g(r)$, the pair distribution function, which expresses the probability of finding an atom of a certain type at distance r from the atom of choice, relative to the ideal gas distribution, and so gives an indication of the ordering of the species in the system.

3.5. Surface Calculations

Surfaces can either be modelled using a 3-dimensional slab method, or by using a 2-dimensional method. The 3D method employs 3D Periodic Boundary Conditions (PBCs), enabling non-specialist codes to perform surface calculations. The surface is made up of a solid slab that repeats in two directions, and is separated from the periodic image of itself by a vacuum gap, which may or may not be filled with some substance. The 3-dimensional slab method is used in this study for surface calculations using DFT methods. As with all simulations that use PBCs it is important that the repeat cell is large enough so that imaging problems do not occur.

The method for studying surfaces using interatomic potentials, in this work, uses the 2D method. Surface calculations will be discussed with the 2D method in mind, but the methods for 3-dimensions are analogous. By convention in 2D calculations the periodicity is in the x and y directions, the z direction describing the depth of the surface. The surface is composed of two regions. Uppermost is the surface region, which is allowed to relax fully upon geometry optimisation. The lower region represents the effect of the bulk on the surface region, and must contain enough atoms to include all the significant interactions between the bulk and the surface. The ions within this region are held fixed at their bulk positions during the optimisation.

Surfaces are denoted by its Miller indices, or Miller-Bravais indices if an hexagonal unit cell is used, which describe the plane through which the bulk structure has been cleaved. The surface is further characterised by the shift, which is the fractional displacement of the surface from the origin of the initial unit cell. Surfaces with different shifts may have different species at the interfacial layer, and the surface energy may vary as a consequence.

3.5.1. Surface Structure

Surfaces can be classified as one of three types, according to the method of Tasker [23]:

> "The surfaces of any ionic or partly ionic crystal may be classified into three types. Type 1 consists of neutral planes with both anions and cations. Type 2 consists of charged planes arranged symmetrically so that there is no dipole moment perpendicular to the unit cell. Neither of these surfaces affect ions in the bulk of the crystal and they should therefore have modest surface energies. The type 3 surface is charged and there is a perpendicular dipole moment. These surfaces have infinite surface energies (or very large surface energies for finite crystals) and produce a polarising electric field on the bulk. An electrostatic argument therefore indicates that such surfaces cannot exist."

The different surface types are illustrated in Figure 3.3. The Type 1 surface obviously will have no net dipole, as each layer of ions is charge neutral. The Type 2 surface is a slightly more complicated matter. It is formed of layers which, when combined, become charge neutral. Consequently, for a given surface there will be shifts that result in a dipole moment across the cell, but there will also be shifts where the arrangement of the layers is such that there is no net dipole.

A dipole will arise at a surface when the difference between the coordination number at the surface and that in the bulk varies for differently charged species [29]. These surfaces are classed as Type 3 surfaces. Modelling of polar surfaces can be problematic, as the electrostatic interactions between surface layers increase for a polar surface, rather than cancelling each other out as they do in Type 1 or Type 2 surfaces. In order to model a polar surface it is necessary to remove the charge imbalance, which is achieved by reconstructing the surface. An appropriate proportion of the ions at the surface must be moved to the bottom of Region 1, and the same proportion then shifted from the Region 1- Region 2 interface to the bottom of the surface unit. This reconstruction may be done by hand, but there are a number of different visualisation packages that facilitate the process. In this

work, the graphical user interface (GUI) GDIS [30] was used to create, manipulate and visualise surfaces and morphologies.

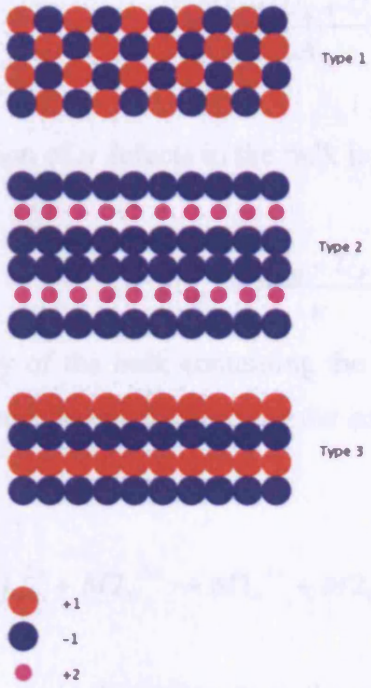

Figure 3.3: The three different types of surfaces, according to Tasker [23]

Once the surface has been relaxed, it is possible to calculate the surface energy. This is defined as the energy required to cleave the surface from the bulk material, and is given by:

$$\gamma = \frac{U_s - U_b}{A}, \tag{3.19}$$

where U_s is the enthalpy of the surface region, U_b is the enthalpy of an equal number of atoms in the bulk and A is the surface area. Surface energies will be positive, and a surface is more stable the closer the value is to zero, ie: the smaller the difference between the values of U_s and U_b.

In this work, substitutions of impurities have been made at the surface. Once a defect impurity has been introduced into the surface, the above equation cannot be used to

calculate the surface energy. Instead, the surface energy must be calculated with respect to the enthalpy of the defect in the bulk, U_{db}:

$$\gamma = \frac{U_1 - (U_b + U_{db})}{A}. \tag{3.20}$$

The enthalpy of substitution of n defects in the bulk is given by:

$$U_{Subs} = \frac{(U_D - U_P)}{n}, \tag{3.21}$$

where, U_D is the enthalpy of the bulk containing the defect, and U_P is the enthalpy of the pure bulk. This corresponds to the reaction for the substitution of an impurity, $M2^{2+}$, for a surface cation, $M1^{2+}$:

$$M1_b^{2+} + M2_x^{2+} \rightarrow M1_x^{2+} + M2_b^{2+}.$$

Conceptually, the cations are substituting from the gas phase, where they exist at infinite separation from the bulk. Under such circumstances, the gaseous ion has no potential energy from interactions with the surface, and within interatomic potential methods, the cation has no self-energy. As such, the energy of the gaseous ions is neglected in equation (3.21), and the substitution energy is calculated solely from the difference in the energies of the surface unit.

When solvation effects are included into calculations, the substitution equations must include the effect of hydration of both the surface and the ions in solution. There are a number of methods that can be used to solvate a surface, which will be discussed in detail in section 3.7.

3.6. Morphology

Morphologies are a sensitive indicator of the relative stabilities of surfaces. The morphology can be calculated from any of three different quantities: surface energy, attachment energy, or d_{hkl} ranking. In this study, Wulff plots[18, 31] have been used to construct the morphology of crystals using either of the first two quantities. When using the surface energy, surfaces with lower surface energies are expressed to a greater extent in the morphology; the distance of the surface plane from the centre of the crystal is proportional to the surface energy. A morphology constructed from the surface energies is known as the equilibrium morphology, whereas that derived from the attachment energy is the growth morphology, which is the morphology as controlled by thermodynamic effects. The less negative the attachment energy, the more likely the surface is to be expressed, as this surface will have the slowest growth. The calculated, equilibrium morphology is usually more representative of small, laboratory-grown crystals, whereas the growth morphology normally echoes the shape of geological samples.

The attachment energy is calculated using:

$$E_{att}(hkl) = \sum_{i=1}^{\infty} E_i(hkl) \tag{3.43}$$

where $E_i(hkl)$ is the interaction energy per molecule between a slice, with thickness d_{hkl} and its i^{th} underlying neighbour. When considering the surfaces solvated under COSMIC (Section 3.7.2.7.), the definition of the attachment energy, which is usually known as the energy required to add one growth slice to the surface, loses meaning, and consequently only equilibrium morphologies are studied in this case.

It is important to note that the crystal morphology is sensitive to environmental factors, and can be influenced not only by the surface and attachment energies: The growth media and conditions, growth mechanism and the presence of impurities can all greatly affect the crystal habit.

3.7. Solvation Methods

This work is focussed on understanding the interaction of aqueous species with dolomite mineral surfaces, in order to clarify the important contributing factors in impurity uptake by dolomite. In so doing, a method has been developed that facilitates the investigation of solid-liquid interfaces, of the nature found in mineral-aqueous solution systems.

While gas phase calculations provide insights into some of the energetics and configurations that are important in the processes studied, the benefit of gas phase calculations is limited. Incorporation of solvation into the model can affect the relative stability of reactants and products, ultimately affecting the viability of a reaction. The inclusion of solvation can also change which configuration of the energy minimised structure for molecules and surfaces by stabilizing different geometries with respect to the gas phase. Adding solvation to the gas phase calculations increases the computational expense of any calculations carried out, so efforts have been made to determine the minimum requirement for the adequate description of solvation for the type of system studied here. To this end, the effect of solvation has been modelled by using two methods in this study; by explicitly describing the solvent molecules (3.4.1) and by using an implicit solvation model (3.4.2), which describes the average effect of the bulk solvent on the solute. These methods have been used together where appropriate, replacing the less influential solvent molecules with a continuum to reduce computational expense.

3.7.1. Explicit Solvation Methods

Explicit solvation methods simulate the effect of individual water molecules on a structure. Modelling water involves the investigation of a very complex potential energy surface, with numerous local minima, which prohibits static optimisation calculations for all but the most simplified cases. In this work, two types of explicit solvation methods have been used: monolayer solvation of surfaces and molecular dynamics simulation of water either at the surface or using a large box of water that also contains the solute.

3.7.1.1. Monolayer Solvation

Hydration of mineral surfaces with a monolayer of water is a method that has commonly been used to assess the surface structure under solution [32-34]. A monolayer coverage on a carbonate mineral surface is considered to be equal to one water molecule per cation site. In order to investigate all possible configurations, a number of different, plausible starting positions are chosen for the water molecules above the cations. Initially, one water molecule is added to the energy-minimised surface structure and optimisation is carried out. The configuration with the lowest energy is chosen, and water molecules are added sequentially, and the structures optimised, until a full monolayer coverage is achieved. In general, the smoother the surface, the easier it is to find a global minimum for the configuration of the monolayer.

3.7.1.2. Water Simulation

Molecular dynamics methods, detailed in section 3.2, are often used to sample the many possible configurations available in large-scale explicit solvation models. In this study, water has been simulated for two different purposes. A 3D box of water has been used to solvate a molecular solute, and a QM MD simulation carried out. Similarly, a QM MD simulation has been carried out on the solvation of a surface using 3D PBCs. The details of these calculations will be given in the following chapters.

3.7.2. Implicit Solvation: Continuum Dielectrics

3.7.2.1. Introduction

Implicit solvation methods have been used for a number of years in order to simulate the effect of a large body of solvent on a molecule or cluster in solution [35-39]. The continuum model is useful when the solvent molecules do not need to be modelled explicitly because they are not directly involved with the processes occurring within the system. In such cases, the solvent can be assessed with respect to the perturbations it

induces in the charge density of the system when compared to the gas phase behaviour, which are the average of the effect from all possible configurational degrees of freedom of the solvent.

Most commonly, continuum representations of the solvent have been applied to individual solute molecules or clusters, and as such much of the following information will be discussed with this in mind. Thereafter follows an explanation of the manner in which these methods can be modified and applied to systems with 2D PBCs.

3.7.2.2. Theory

The Gibbs' free energy of solvation is the energy difference between the existence of a molecule in the gas phase and the molecule in solution. It can be calculated as the sum of contributing energies, thus:

$$\Delta G_{solvation} = \Delta G_{el} + \Delta G_{vdW} + \Delta G_{cavity}(+\Delta G_{hb}). \tag{3.23}$$

These energies are, respectively, the electrostatic energy arising from solvation, the van der Waals' energy, comprising, as we know, of a repulsive and an attractive term, and finally the free energy required for the formation of the cavity. The last of these has a large entropic contribution due to the requirement for the reorganisation of the solvent molecules around the solute. The bracketed term is the contribution from solute-solvent hydrogen bonding, should this arise in the system.

The theory behind continuum solvation models stems from basic electrostatics. From Gauss' law, the electric field, **E**, that is generated by a point charge, q, is related to the magnitude of the charge at any point defined by a vector, **r**, by:

$$\mathbf{E}(\mathbf{r}) = \frac{q}{4\pi\varepsilon_0 r^3}\mathbf{r}. \tag{3.24}$$

In practical terms, it is more useful to relate the electric field to the charge density rather than the point charge. This is possible through the divergent relationship between the electric field and the charge:

$$\nabla \mathbf{E} = \frac{\rho}{\varepsilon_0}, \tag{3.25}$$

where ρ is the charge density and ε_0 is the permittivity of a vacuum.

However, evaluation of the electric field is mathematically complicated because it is a vector field, so it is convenient in analytic solutions to replace the electric field with the electrostatic potential, ϕ, which is a scalar quantity, through the relation:

$$\mathbf{E} = -\nabla\phi. \tag{3.26}$$

The above relationship is used in Poisson's equation, which describes the electrostatic potential within a dielectric as a consequence of the embedding of a charge, at a point, $\mathbf{r}$, as a function of the dielectric constant, ε, and the charge density:

$$\nabla^2\phi(\mathbf{r}) = -\frac{4\pi\rho(\mathbf{r})}{\varepsilon}. \tag{3.27}$$

In the case of continuum solvation, the solute is confined within the cavity, upon the surface of which the charge is distributed. The cavity constitutes a region that is discrete from that of the solvent medium, which is not described by the solvent's dielectric constant. Consequently, the Poisson equation can be rewritten in this instance so that:

$$\nabla \cdot [\varepsilon(\mathbf{r})\nabla\phi(\mathbf{r})] = -4\pi\rho(\mathbf{r}). \tag{3.28}$$

The Poisson equation must be solved for all continuum solvation models of a non-ionic solvent. However, when using continuum solvation to model ionic solvents, it should be

noted that the system has additional complexity and it is necessary for the potential to satisfy the Poisson-Boltzmann equation, which uses the Boltzmann distribution to describe the whereabouts of the ions that comprise the solvent. Analytical solution of the Poisson and Poisson-Boltzmann equations is only possible if applied to ideal shaped solute cavities, although the equations can be modified for an ellipsoidal cavity by using the axes of the ellipse rather than the radius of the sphere; cylinders can also be used.

The electrostatic contribution to the solvation energy is the work necessary to polarise the charge distribution of the species in solution in comparison to the gas phase. The polarisation in solution is a result of the interaction between the charge density of the solute and the electrostatic potential of the solute, known as the *reaction field*, according to:

$$G_{el\_sol} = -\frac{1}{2}\int \rho(\mathbf{r})\phi(\mathbf{r})d\mathbf{r}. \tag{3.29}$$

The factor of one half is included because the electrostatic potential and the charge density are interacting with each other, and so the electrostatic potential is not external to the solute. The first calculation of the electrostatic contribution was derived by the inimitable Max Born, who derived the electrostatic contribution to the free energy of solvation of a charge within a spherical solvent cavity in 1920 [19]. Under these circumstances, the charge density is uniformly distributed on the surface of the sphere, of radius a, so that at any point $\mathbf{s}$ on the surface:

$$\rho(\mathbf{s}) = \frac{q}{4\pi a^2}. \tag{3.30}$$

The solution for the Poisson equation in this special case gives the electrostatic potential as:

$$\phi(\mathbf{r}) = -\frac{q}{\varepsilon|\mathbf{r}|}. \tag{3.31}$$

The combination of equations (3.29), (3.30) and (3.31) gives the polarisation energy in solution:

$$G_{el\_sol} = -\frac{1}{2}\int\left(\frac{q}{4\pi a^2}\right)\left(-\frac{q}{\varepsilon a}\right)d\mathbf{s} = \frac{q^2}{2\varepsilon a} \tag{3.32}$$

The work done for the transfer of the point charge from the gas phase into solution is then given by the Born equation:

$$\Delta G_{el} = -\frac{q^2}{2a}\left(1-\frac{1}{\varepsilon}\right). \tag{3.33}$$

Equation (3.33) can be used to calculate the electrostatic contribution to the solvation energy through the charge on the ion, q, the dielectric constant, ε, and a, the cavity radius. The dielectric value of the solvent can be altered within the calculation, so that in effect the solvent can be changed. In this work, the only solvent that has been used has been water, the dielectric constant of which is 78.4.

3.7.2.3. Simple Models

Born's work laid the foundation for Kirkwood's work on the solvation of molecules consisting of point charges in a sphere [40], and for Onsager to derive the electrostatic contribution for a dipole in a spherical cavity [41]:

$$\Delta G_{el} = -\frac{\mu^2}{2a^3}\left(\frac{2(\varepsilon-1)}{(2\varepsilon+1)}\right). \tag{3.34}$$

Indeed, the Onsager model is implemented in a number of codes as one of the available continuum solvation methods. The Kirkwood-Onsager equation (3.34), which relates directly to the Born equation, gives the electrostatic contribution to the solvation energy as a function of the dipole moment, μ, although this concept can be extended to incorporate

multipoles of higher order to increase accuracy, and also to solve the problem that the use of the above expression will give zero energy for a solute with no dipole.

The Onsager model can be used to calculate the electrostatic contribution to the solvation energy using quantum mechanics by modifying the Hamiltonian to include the perturbations induced by the solvent upon the solute. The total Hamiltonian then becomes:

$$\hat{H}_{tot} = \hat{H}_0 + \hat{H}_{RF}. \tag{3.35}$$

$\hat{H}_0$ is the standard gas-phase Hamiltonian and $\hat{H}_{RF}$ is that of the reaction field [42]:

$$\hat{H}_{RF} = -\mu^{\mathrm{T}} \cdot \left[\left(\frac{2(\varepsilon-1)}{(2\varepsilon+1)a^3}\right)\mathbf{1}\right] \cdot \langle \Psi \mid \mu \mid \Psi \rangle, \tag{3.36}$$

comprising the dipole moment operator, its transpose μ^{T}, and a coupling tensor (in squared brackets, wherein **1** is the unit tensor).

The electrostatic contribution to the solvation energy is then given by:

$$\Delta G_{el} = \langle \Psi \mid \hat{H}_{tot} \mid \Psi \rangle - \langle \Psi_0 \mid \hat{H}_0 \mid \Psi_0 \rangle + \frac{\mu^2}{2a^3}\left(\frac{2(\varepsilon-1)}{(2\varepsilon+1)}\right) \tag{3.37}$$

The second term involves the gas phase Hamiltonian acting on the gas phase wavefunction. Equation (3.37) is solved iteratively to find the wavefunction, as is the case in usual quantum mechanical calculations, and also involves another self-consistent iterative sequence to solve with respect to the reaction field Hamiltonian. Due to this, the method is known as the Self Consistent Reaction Field method (SCRF).

While the Onsager model is still used today, continuum solvation methods have become increasingly sophisticated since the initial work in the early half of the last century. There

is a wealth of literature on this rapidly developing field; consequently, the methods most relevant to the work in hand are discussed in detail, and only brief reference is made to the alternatives available.

3.7.2.4. PCM and Further Developments

The greatest drawback of the Born and Onsager models are the cavity shape, which must be ideal in order for the posited analytical solutions to apply. The most standard method used to define a more realistic cavity shape is the assignment of spheres of an appropriate radius, usually related to the respective van der Waals' radii, to the atoms that comprise the solute, such as is used in the Polarisable Continuum Model (PCM) [43]. There are also models that assign the surface through isodensities, such as the IPCM, which uses the gas-phase charge density, or SCIPCM [44], which alters the surface self-consistently as the charge density is calculated throughout the simulation. In all cases where the cavity shape is non-ideal, the Poisson equation must be solved numerically.

A standard method of numerically solving for ΔG_{el}, which was initially introduced in the PCM, is to cover the solute surface in small tesserae, each of which contain a point charge that is proportional to the electric field normal to that surface segment. In this model, the total electric field depends on contributions from two factors: the potential due to the solvent and the potential due to the other point charges in different surface segments. The method employed in the PCM involves a number of iterative cycles. Initially the gas phase charge distribution is taken; from equation (3.25), the electric field is then determined normal to the centre of each segment, and then the density of virtual charges on the cavity surface is determined using the following relation:

$$\sigma(s) = -\left(\frac{(\varepsilon - 1)}{4\pi\varepsilon}\right)\mathbf{E}_{\rho}(s)_{vac}, \tag{3.38}$$

where $\mathbf{E}_{\rho}$ is the electric field, normal to the surface, in vacuum. The virtual point charges at the centre of each segment, i, are then found by using the relation:

$$q_i = \sigma(s)_i \Delta S_i . \tag{3.39}$$

These point charges are used, in turn, to give a value of the electric field deriving from the surface charges, $\mathbf{E}_\sigma$, which is calculated as the finite difference between the electric field at the surface vector, and at a point normal to the surface at an increment, δ_i, from the surface within the cavity. The method must include here calculation of the self-polarisation of the surface charge at each point on the surface, as the finite difference method for the evaluation of the electric field at each point must exclude the point charge to avoid divergence. This is determined using Gauss' theorem, which gives the electric field due to a surface element, but this method includes neither the effects of the curvature of the surface segments nor the perturbations of the charge density within the segment, both of which necessitate the incorporation of correction factors. This additional contribution to the electric field is subsequently used to give an improved value of the charge density:

$$\sigma(s) = -\left(\frac{(\varepsilon - 1)}{4\pi\varepsilon}\right)\left(\mathbf{E}_\rho(s) + \mathbf{E}_\sigma(s)\right). \tag{3.40}$$

The process is repeated until self-consistency is achieved. The final set of point charges give rise to a new approximation of the charge distribution through the solution of the modified Hamiltonian, which incorporates the electrostatic potential derived from the surface charge:

$$\hat{H} = \hat{H}_0 + \phi_\sigma \tag{3.41}$$

The new value of ρ is subsequently used in a new iterative cycle, until convergence is achieved.

Another variant on the PCM is IEF-PCM [45, 46], or Integral Equation Formulation PCM. IEF-PCM and CPCM both use operators that relate to the electrostatic potential rather than

the electric field [47], which decreases the magnitude of the error arising for the solute charge distribution partially lying outside the cavity.

3.7.2.5. Conductor-Like Models

The electrostatic potential will vary through the solvent, which is difficult to represent when using the segment / point charge approach outlined above. In the PCM, formulae have been derived that compensate for these tails of charge distribution. A variant on the above approach that addresses the aforementioned problem is to treat the solvent dielectric as a conductor, as conductors have an infinite dielectric constant and thus they have no electrostatic potential. Once found, the surface charges are scaled by the Onsager factor for the reaction field, $2(\varepsilon-1)/(2\varepsilon+1)$, to incorporate the dielectric nature of the solvent. There are two implementations of this method in use, the Conductor-like Screening Model, COSMO [48] and CPCM [49], the latter an application of the concept to the PCM method. The conductor approximation is beneficial in the respect that it removes the necessity for iteratively solving the charge density with respect to the electric field. COSMO uses a slightly different formulation from PCM in the construction of the cavity surface; the solvent accessible surface (SAS) is created from the assignment of overlapping spheres as in PCM, but an additional exclusion zone is added, which describes, and has the magnitude of, the effective radius of the solvent molecules. The points on the surface are assigned by the projection onto the system of an atom-centred icosahedron, and the number of points is then increased by iterative triangulation until the desired number of points is achieved. The points are, subsequently, grouped into segments, and at long range the interactions between segments, rather than individual points, is calculated. An additional term, which is usually derived empirically, is then subtracted from this total radius, and accounts for the location of the solvent screening charges away from the centre of the solvent molecule.

3.7.2.6. Alternative Methods

There are alternative methods for the application of continuum solvation; however, as they were not used in this work they will be addressed only briefly. Poisson's equation and the

Poisson-Boltzmann equation can be evaluated directly through imposing a 3-dimensional mesh on the system. Values for the electrostatic potential and dielectric constant are assigned to each grid point, a low dielectric constant (usually 2-4) being assigned to the cavity space. The charge associated with any point is distributed over the 8 surrounding grid-cubes; the closer the cube to the point the higher the proportion of the charge that is allocated to that cube. The charge electrostatic potential for each cube is the solved iteratively, with each cube interacting with its surroundings, until a stationary point is found for the potential.

The Born model has been extended to the Generalised Born model, which is applicable to non-ideal solutes. The electrostatic contribution to the solvation energy is calculated as a combination of the Coulomb energy and the Born free energy of solvation. The former is determined by the partial charges on the solute's atoms; however, determination of the latter is more complicated. Effective Born radii are assigned to the atoms within the solute molecule by solving the Poisson equation for each atom. Thus, the polarisation energy for the atom is found by solving a radial integral over a system of spheres that radiate from the centre of each atom until the entire molecule is enclosed in the final sphere, and thereafter analytically solving the Born equation for a sphere containing the atom's partial charge. The polarisation energy for the atom is used to assign the effective Born radii for the solute's atoms, which can then be used in the Generalised Born equation to find ΔG_{el}.

The Generalised Born model uses partial charges and so is directly applicable to force field methods. Some force field methods approximate that the solvation energy can be determined by the exposed surface area ([50], and references therein). The other models discussed above can also be modified for use with either force field or semi-empirical methods.

Some of the above methods allow for the calculation of the dispersive-repulsive and cavitation contributions to the solvation free energy within their formulation. It is possible to incorporate these contributions into the Hamiltonian at the same time as the electronic contribution [47], but it is more common for them to be assessed classically [51]. The

cavitation energy can be assessed by the application of formulae, which relate the energy to the cavity volume, developed from the examination of the solvation energies of the noble gases, for which the energies arising from polarisation can be assumed to be minimal[52, 53]. To calculate the dispersion-repulsion term, data from gas phase calculations can be used to assess the polarisabilites of the solute and solvent separately [54]. It is possible to calculate the non-electrostatic contributions using one scheme only, which relies on the area of the SAS and the characteristic surface tensions of the various groups comprising the solute. The non-electrostatic contribution to the energy is then found by summing over the surface tension multiplied by the accessible area for each group. The surface tensions can either be taken from a database of values determined empirically, or they can be calculated as a function of solvent properties, as in the SMx models [50] and COSMO-RS (COSMO for Real Solvents) [55]. Despite its apparent improvements, COSMO-RS was not used in this work, as it has not been implemented in Gaussian03, the code used for the majority of the QM calculations.

3.7.2.7. Surface Solvation

In this work, a new implementation of continuum solvation, COSMIC [56], has been used to assess surface solvation, using 2-dimensional PBCs. This model is based on the approach of COSMO, although the approach has been developed for force field methods, so the atom charge-atom charge interactions are described by the interatomic potentials and need not be calculated within the solvation model, and there are some important differences in the implementation. In order to reduce symmetry-breaking forces on formulation of the points, a starting polyhedron of octahedral shape is chosen. Additionally, upon relaxation the number of points at the surface may change as the accessible surface area for each atom varies. To avoid discontinuity at the surface, a weighting function has been introduced for each point, which depends on a unit switching function of the distance between surface points. This weighting factor is incorporated into the matrices that describe the Coulombic interaction between surface points and the interaction between each point and the charge on the atom to which that sphere belongs. The latter Coulombic interaction is then assessed using the Parry summation, as with any 2D surface calculation, to account for the

conditional convergence. However, for the point-point Coulombic interactions another strategy is needed, because the requirement of charge neutrality for the Parry summation is not fulfilled under these circumstances. For this reason, the Wolf summation technique [24] has been used, which sums over real space and avoids the difficulty of fulfilling charge neutrality. A further modification is needed in the periodic system, to avoid the formation of a charged system, which will usually arise due to the induced charges at the surface. The implementation for COSMIC, then, applies the weighting factors, w_i, already defined for the matrices that describe the Coulombic interactions of the charges, to the surface point charges, q, yielding COSMIC induced point charges:

$$q^C = q - w\left(\frac{(\sum q_i)}{(\sum w_i)}\right) \tag{3.42}$$

Here, w, is the vector for all the weights of the point charges on the SAS. This results in the desired charge neutrality at the SAS.

3.8. Conclusions

In this chapter, the basic theory behind the research presented in this thesis has been described. The remainder of the thesis describes the results obtained using these methods, and gives a detailed description of the methodology for each section. Chapter 4 reports the results of empiricial calculations on morphologically important dolomite surfaces under vacuum, chapter 5 reports similar calculations and the effect of different types of solvation on the results and chapter 6 gives the results of QM calculations on the most predominant dolomite surface, and its interaction with complex impurities.

Overall, the thesis reports the application of the various methods detailed in this chapter to a complex chemical system, and evaluates the appropriateness of each method to the given task.

1. Fock, V., Zeitschrift Fur Physik, 1930. **61**: p. 126.
2. Leach, A.R., *Molecular Modelling: Principles and Applications*. 2nd ed. 2001, Harlow, Essex: Pearson Education Limited.
3. Cramer, C.J., *Essentials of Computational Chemistry: Theories and Models*. 2nd Edition ed. 2004, Chichester: John Wiley & Sons Ltd.
4. Hohenberg, P. and W. Kohn, *Inhomogeneous Electron Gas.* Physical Review B, 1964. **136**(3B): p. B864-&.
5. Kohn, W. and L.J. Sham, *Self-Consistent Equations Including Exchange And Correlation Effects.* Physical Review, 1965. **140**(4A): p. 1133-&.
6. Teale, A.M. and D.J. Tozer, *Exchange methods in Kohn-Sham theory.* Physical Chemistry Chemical Physics, 2005. **7**(16): p. 2991-2998.
7. Perdew, J.P., et al., *Prescription for the design and selection of density functional approximations: More constraint satisfaction with fewer fits.* Journal Of Chemical Physics, 2005. **123**(6).
8. Perdew, J.P., et al., *Meta-generalized gradient approximation: Explanation of a realistic nonempirical density functional.* Journal Of Chemical Physics, 2004. **120**(15): p. 6898-6911.
9. Kurth, S. and J.P. Perdew, *Role of the exchange-correlation energy: Nature's glue.* International Journal Of Quantum Chemistry, 2000. **77**(5): p. 814-818.
10. Kurth, S., J.P. Perdew, and P. Blaha, *Molecular and solid-state tests of density functional approximations: LSD, GGAs, and meta-GGAs.* International Journal Of Quantum Chemistry, 1999. **75**(4-5): p. 889-909.
11. Perdew, J.P., K. Burke, and Y. Wang, *Generalized gradient approximation for the exchange-correlation hole of a many-electron system.* Physical Review B, 1996. **54**(23): p. 16533-16539.
12. Perdew, J.P., M. Emzerhof, and K. Burke, *Rationale for mixing exact exchange with density functional approximations.* Journal Of Chemical Physics, 1996. **105**(22): p. 9982-9985.
13. Perdew, J.P., K. Burke, and M. Ernzerhof, *Local and gradient-corrected density functionals*, in *Chemical Applications Of Density-Functional Theory*. 1996. p. 453-462.

14. Becke, A.D., *Density-Functional Exchange-Energy Approximation With Correct Asymptotic-Behavior.* Physical Review A, 1988. **38**(6): p. 3098-3100.
15. Perdew, J.P. and W. Yue, *Accurate And Simple Density Functional For The Electronic Exchange Energy - Generalized Gradient Approximation.* Physical Review B, 1986. **33**(12): p. 8800-8802.
16. Lee, C.T., W.T. Yang, and R.G. Parr, *Development Of The Colle-Salvetti Correlation-Energy Formula Into A Functional Of The Electron-Density.* Physical Review B, 1988. **37**(2): p. 785-789.
17. Woon, D.E. and T.H. Dunning, *Gaussian-Basis Sets For Use In Correlated Molecular Calculations .5. Core-Valence Basis-Sets For Boron Through Neon.* Journal Of Chemical Physics, 1995. **103**(11): p. 4572-4585.
18. Gale, J.D. and A.L. Rohl, *The General Utility Lattice Program (GULP).* Molecular Simulation, 2003. **29**(5): p. 291-341.
19. Born, M., *Volumen and Hydratationswärme der Ionen.* Zeitschrift für Physik, 1920. **1**: p. 45-48.
20. Ewald, P.P., *Due Berechnung optischer und elektrostatischer Gitterpotentiale.* Annalen der Physik, 1921. **64**: p. 253-287.
21. Parry, D.E., *Electrostatic Potential In Surface Region Of An Ionic-Crystal.* Surface Science, 1975. **49**(2): p. 433-440.
22. Cramer, C.J. and J.A. Board, *The Development and Integration of a Distributed 3D FFT for a Cluster of Workstations.* Proceedings of the 4th Annual Linux Showcase and Conference, Atlanta, 2000: p. 121-128.
23. Tasker, P.W., *Stability of Ionic-Crystal Surfaces.* Journal of Physics C-Solid State Physics, 1979. **12**(22): p. 4977-4984.
24. Wolf, D., et al., *Exact method for the simulation of Coulombic systems by spherically truncated, pairwise r(-1) summation.* Journal Of Chemical Physics, 1999. **110**(17): p. 8254-8282.
25. Levine, I.N., *Quantum Chemistry.* 5th ed. 2000, New Jersey: Prentice Hall.
26. Dobson, J.F. and A. Rubio, *Nonuniversality of the dispersion interaction: analytic benchmarks for van der Waals' energy functionals* Condensed Matter: cond-mat/0502422, 2005.

27. Jensen, F., *Introduction to Computational Chemistry.* John Wiley and Sons Ltd., Chichester, 1999.
28. Dick, B.G. and A.W. Overhauser, *Theory of the Dielectric Constants of Alkali Halide Crystals.* Physical Review, 1958. **112**(1): p. 90-103.
29. Nygren, M.A., et al., *Incorporation of growth-inhibiting diphosphates into steps on the calcite cleavage plane surface.* Journal of the Chemical Society-Faraday Transactions, 1998. **94**(24): p. 3685-3693.
30. Fleming, S., *GDIS: GTK Display Interface For Structures.*
31. Wulff, G., *Zur Frage der Geschwindigkeit des Wachstums und der Aufl osung der Krystallflachen.* Zeitschrift Krystallographica Mineral. , 1901. **34**: p. 449.
32. de Leeuw, N.H. and S.C. Parker, *Atomistic simulation of the effect of molecular adsorption of water on the surface structure and energies of calcite surfaces.* Journal of the Chemical Society-Faraday Transactions, 1997. **93**(3): p. 467-475.
33. Wright, K., R.T. Cygan, and B. Slater, *Structure of the (10(1)over-bar4) surfaces of calcite, dolomite and magnesite under wet and dry conditions.* Physical Chemistry Chemical Physics, 2001. **3**(5): p. 839-844.
34. de Leeuw, N.H. and S.C. Parker, *Surface-water interactions in the dolomite problem.* Physical Chemistry Chemical Physics, 2001. **3**(15): p. 3217-3221.
35. Mehler, C., A. Klamt, and W. Peukert, *Use of COSMO-RS for the prediction of adsorption equilibria.* Aiche Journal, 2002. **48**(5): p. 1093-1099.
36. Klamt, A., *Prediction of the mutual solubilities of hydrocarbons and water with COSMO-RS.* Fluid Phase Equilibria, 2003. **206**(1-2): p. 223-235.
37. Tossell, J.A., *Theoretical studies on the formation of mercury complexes in solution and the dissolution and reactions of cinnabar.* American Mineralogist, 1999. **84**(5-6): p. 877-883.
38. Tossell, J.A., *Calculation of the visible-UV absorption spectra of hydrogen sulfide, bisulfide, polysulfides, and As and Sb sulfides, in aqueous solution.* Geochemical Transactions, 2003. **4**: p. 28-33.
39. Tossell, J.A., *Theoretical studies on arsenic oxide and hydroxide species in minerals and in aqueous solution.* Geochimica Et Cosmochimica Acta, 1997. **61**(8): p. 1613-1623.

40. Kirkwood, J.G., *Theory of Solutions of Molecules Containing Widely Separated Charges with Special Application to Zwitterions.* Journal of Chemical Physics, 1934. **2**(7): p. 351-361.

41. Onsager, L., *Electric Moments of Molecules in Liquids.* Journal of the American Chemical Society, 1936. **58**: p. 1486-1493.

42. Tapia, O. and O. Goscinski, *Self-Consistent Reaction Field-Theory Of Solvent Effects.* Molecular Physics, 1975. **29**(6): p. 1653-1661.

43. Miertus, S., E. Scrocco, and J. Tomasi, *Electrostatic Interaction Of A Solute With A Continuum - A Direct Utilization Of Abinitio Molecular Potentials For The Prevision Of Solvent Effects.* Chemical Physics, 1981. **55**(1): p. 117-129.

44. Foresman, J.B., et al., *Solvent effects .5. Influence of cavity shape, truncation of electrostatics, and electron correlation ab initio reaction field calculations.* Journal Of Physical Chemistry, 1996. **100**(40): p. 16098-16104.

45. Cances, E., B. Mennucci, and J. Tomasi, *A new integral equation formalism for the polarizable continuum model: Theoretical background and applications to isotropic and anisotropic dielectrics.* Journal Of Chemical Physics, 1997. **107**(8): p. 3032-3041.

46. Tomasi, J., B. Mennucci, and E. Cances, *The IEF version of the PCM solvation method: an overview of a new method addressed to study molecular solutes at the QM ab initio level.* Journal Of Molecular Structure-Theochem, 1999. **464**(1-3): p. 211-226.

47. Amovilli, C., et al., *Recent advances in the description of solvent effects with the polarizable continuum model*, in *Advances In Quantum Chemistry, Vol 32: Quantum Systems In Chemistry And Physics, Pt Ii.* 1999. p. 227-261.

48. Klamt, A. and G. Schuurmann, *Cosmo - a New Approach to Dielectric Screening in Solvents with Explicit Expressions for the Screening Energy and Its Gradient.* Journal of the Chemical Society-Perkin Transactions 2, 1993(5): p. 799-805.

49. Barone, V. and M. Cossi, *Quantum calculation of molecular energies and energy gradients in solution by a conductor solvent model.* Journal Of Physical Chemistry A, 1998. **102**(11): p. 1995-2001.

50. Cramer, C.J. and D.G. Truhlar, *Implicit solvation models: Equilibria, structure, spectra, and dynamics.* Chemical Reviews, 1999. **99**(8): p. 2161-2200.

51. Cossi, M., et al., *Energies, structures, and electronic properties of molecules in solution with the C-PCM solvation model.* Journal of Computational Chemistry, 2003. **24**(6): p. 669-681.

52. Pierotti, R.A., *Scaled Particle Theory Of Aqueous And Non-Aqueous Solutions.* Chemical Reviews, 1976. **76**(6): p. 717-726.

53. Colominas, C., et al., *Cavitation contribution to the free energy of solvation. Comparison of different formalisms in the context of MST calculations.* Chemical Physics, 1999. **240**(1-2): p. 253-264.

54. Floris, F.M., A. Tani, and J. Tomasi, *Evaluation Of Dispersion Repulsion Contributions To The Solvation Energy - Calibration Of The Uniform Approximation With The Aid Of Rism Calculations.* Chemical Physics, 1993. **169**(1): p. 11-20.

55. Klamt, A., et al., *Refinement and parametrization of COSMO-RS.* Journal of Physical Chemistry A, 1998. **102**(26): p. 5074-5085.

56. Gale, J.D. and A.L. Rohl, *An efficient technique for the prediction of solvent-dependent morphology: The COSMIC method.* In Preparation.

4. SURFACES AND SURFACE IMPURITIES: RESULTS OF METAL SUBSTITUTION REACTIONS

"The power of any springy body is in the same proportion with the extension." Robert Hooke, 1676.

The energetics of impurity incorporation into dolomite surfaces are important in understanding the mechanisms through which metal pollutants complex with the mineral in nature. In order to look at the various contributing factors that determine metal uptake at the mineral surface, the surfaces have been modelled under dry conditions initially, and subsequently were modelled using two methods of solvation: monolayer solvation and COSMIC implicit solvation. This chapter describes the interatomic potential methods used to probe the thermodynamic element of impurity substitution into dolomite surfaces.

4.1. Methods and Parameters Used

The calculations were carried out using interatomic potential methods, using the GULP code [1], and the surfaces were modelled using 2-dimensional PBCs. In this study, impurity substitutions have been investigated on the morphologically important $(10\bar{1}4)$, $(11\bar{2}0)$, $(30\bar{3}0)$ and $(10\bar{2}1)$ surfaces, the latter of which is a polar 'type 3' surface [2]. In the case of the polar surface, the surface was reconstructed to remove the surface dipole. In nature, either a reconstruction would occur, or the polarity of the surface would be quenched by the formation of an electrical double layer. The reconstruction method, used in this study, involved moving the required number of units from the surface to the region 1-region 2 interface, and moving an equal number of the same units from the interface to the bottom of region 2. The units moved, in the case of the polar surface reconstruction, possess charge of the nature in excess at the bulk-terminated surface. Surface super-cells were used to avoid defect self-interaction across the periodic boundary, and to facilitate study of the effect of relative substitution site on the energy of substitution. The super-cells contained the same number of formula units for each surface, so that there were 24 cations on each surface repeat unit, allowing for direct comparisons to be made when individual

substitutions were made. The exception is the $(10\bar{2}1)$ surface, where a 2x1 surface supercell was used, such that after reconstruction there were 3 possible surface sites for cation substitution. The sizes of region 1 and region 2 in the 2D surface block were converged for each of the surfaces studied, such that increasing their size had negligible effect on the surface energy. The size of region 1 was converged at 14.4 Å for the $(10\bar{1}4)$ and $(11\bar{2}0)$ surfaces and at 16.7 and 16.1 Å for the $(30\bar{3}0)$ and $(10\bar{2}1)$, regions respectively.

The most morphologically important surface is known to be the $(10\bar{1}4)$ surface [3], and as such it has been the focus of extra study. It is well known that real surfaces contain many defects such as steps and islands, which disrupt the perfect terrace termination in the surface plane [4]. To incorporate surface defects into the model, steps were created on the morphologically important $(10\bar{1}4)$ surface. The method used was similar to that used to reconstruct the polar $(10\bar{2}1)$ surface, however, in the case of step formation, charge neutral units were removed to the bottom of the surface block. The size of the terrace and trough created were converged so that the step edges would not interact.

Impurity cations were substituted on each non-polar surface, at calcium and magnesium sites. The impurities studied were Fe^{2+}, Zn^{2+}, Co^{2+}, Cd^{2+}, Mn^{2+} and Ni^{2+}, all of which are found alongside dolomite in aqueous environments, and which form end member carbonate minerals. Single and multiple substitutions were made, and substitutions were made at both calcium and magnesium sites together as well as separately. The stabilities of the various possible terminations for the polar surface were compared, and impurity substitutions were made on the lowest energy termination. Due to the surface cuts, only one type of cation is exposed at the surface for each termination of the $(10\bar{2}1)$ surface. Prior to carrying out substitutions at cation sites on the stepped $(10\bar{1}4)$ surface, the energetics of the different terminations was investigated. In order to understand the differences in stability between the stepped surface and the terrace, the most stable step configuration was investigated. The most energetically favoured configuration has an acute carbonate termination combined with a calcium ion termination, which is discussed in more detail below.

The surface energy, or energy per unit area required to form the surface from the bulk, is calculated as follows:

$$\gamma = \frac{U_s - U_b}{A}, \qquad (4.1)$$

where U_s is the energy of region 1, U_b is the energy of an equal number of atoms in the bulk and A is the surface area. Surface energies will be positive, and a surface is more stable the closer the value is to zero, ie: the smaller the difference between the values of U_s and U_b.

Once an impurity has been introduced into the surface, equation (4.1) can no longer be used to calculate the surface energy. Instead, the surface energy must be calculated with reference to the enthalpy of the defect in the bulk, U_{db}:

$$\gamma = \frac{U_s - (U_b + U_{db})}{A}. \qquad (4.2)$$

where, U_s is the enthalpy of atoms in the surface region, U_b is the enthalpy of the same number of atoms in the bulk and U_{db} is the enthalpy of the defect in the bulk.

For substitutions at the surface under vacuum, the impurity cations are considered to come from the bulk end-member carbonate. So, the reaction for the substitution of a divalent impurity cation, M2, at a Ca or Mg site, denoted by M1, on the dolomite surface is given as:

$$U_{s_{pure}} + U_{M2CO_3} \rightarrow U_{s_{def}} + U_{M1CO_3}. \qquad (4.3)$$

U_{MXCO_3} is the enthalpy of one formula unit of an end-member carbonate mineral.

The enthalpy of substitution for the above reaction is found using:

$$U_{Subs} = \frac{\left(U_{s_{def}} - U_{s_{pure}}\right) + n\left(U_{M1CO_3} - U_{M2CO_3}\right)}{n}, \tag{4.4}$$

where $U_{s_{def}}$ is the total enthalpy of the system with n substitutions at the surface, and $U_{s_{pure}}$ is the total enthalpy of a pure system of the same size, U_{M1CO_3} is the enthalpy of one formula unit of calcite or magnesite, depending on which cation is replaced at the surface, and U_{M2CO_3} is the enthalpy of one formula unit of the carbonate mineral that corresponds to the impurity cation. For the calculation of the enthalpy per cation of multiple substitutions at both Ca and Mg sites, equation (4.4) can be modified, thus:

$$U_{Subs} = \frac{\left(U_{s_{def}} - U_{s_{pure}}\right) + \left(\left(n_{Ca}U_{CaCO_3} + n_{Mg}U_{MgCO_3}\right) - n_{Ca+Mg}U_{M2CO_3}\right)}{n_{Ca+Mg}}, \tag{4.5}$$

where n_{Ca} is the number of substitutions at the Ca site, likewise n_{Mg} is the number at the Mg site, and n_{Ca+Mg} is the total number of substitutions at the surface.

Addition of a monolayer of water to the surface was attempted for all the non-polar surfaces, using the method outlined in section 3.7.1.1 There is a propensity for getting stuck in local minima for monolayer coverage on surfaces, which is in proportion to the surface's roughness; the rougher the surface, the more difficult it is to find a good starting configuration for the water molecules that will minimise readily. The $(10\bar{1}4)$ surface is the least bumpy of the surfaces studied and a global minimum was achieved. However, for the other surface too many local minima existed for a satisfactory stationary point to be found. The energy for the surface with a monolayer is given by the difference between the enthalpy of the surface with n water molecules and the dry surface plus the same number of water molecules in the gas phase [5]. It can be calculated using the following formula:

$$\gamma_{ML} = \frac{U_{s_{hyd}} - \left(U_b + nU_{H_2O_{(1)}}\right)}{A}, \tag{4.6}$$

where $U_{H_2O_{(l)}}$ is the potential enthalpy of n water molecules forming the monolayer, which is equal to the condensation energy for that number of water molecules plus the self energy of the same number of water molecules. To remain self-consistent this value is taken from the work of de Leeuw and Parker [6], from which the parameters for water have been taken. When calculating the energy of substitution of an impurity at the hydrated surface, the energy of formation for the aqueous species must be incorporated, thus:

$$E_{subs\_wet} = \frac{U_{s_{def}} - U_{s_{pure}} - n\left(\Delta_{hyd}G^{\circ}{}_{M2^{2+}(aq)} + \Delta_{hyd}G^{\circ}{}_{M1^{2+}(aq)}\right)}{n}. \qquad (4.7)$$

In the formula above, $M2^{2+}$ denotes the impurity cation and $M1^{2+}$ is the initial surface cation, either calcium or magnesium. The quantity $\Delta_{hyd}G^{\circ}$ is the Gibbs free energy of hydration of the ion, calculated from experiment [7].

The carbonate potential and its interaction with calcium were those of Rohl *et al.* [8], which have been used to model accurately the surface reconstruction of calcite. This potential describes the polarisability of the oxygen ions using the shell model [9]. These potentials can be modified easily for use with the other carbonate minerals through combination with the potentials of Fisler *et al.* [10] to gain the cation-carbonate oxygen potential. Cation-carbon potentials (Table 4.1) were determined through scaling the A parameter of the Born-Mayer potential for the Ca^{2+}-C interaction from Rohl *et al.* [8] with respect to variations in ionic radius [11], a method that has been employed previously with success to derive potentials for ions of varying size [12]. The exception was Mg^{2+}-C interaction, which given its importance in the dolomite structure was varied to optimise lattice parameters and bulk modulus of dolomite and magnesite ($MgCO_3$). It was found that the magnitude of the A parameter of the cation-carbon potential contributes minimally to the energy of the total system and as such varying its value has little effect on the bulk and surface structures studied, as the cation-oxygen potential dominates. Water potentials were those of de Leeuw *et al.* [13], and modified by expressing the Coulomb term as a Morse potential for compatibility with the program used for calculations, GULP 3 [1]. The cation-O_{water}

potentials for the impurity cations were scaled from the cation-$O_{carbonate}$ potential as described in Wright *et al.*[5].

Table 4.1: Born-Mayer Potentials used in this work

Born-Mayer Potential: $U_r = A\exp\left(-\frac{r}{\rho}\right)$

	A/ eV	ρ/ Å	Cutoff/ Å
Ca core C core	120000000	0.12000	10.0
Mg core C core	26164795.4	0.12000	10.0
Fe core C core	90909090.91	0.12000	10.0
Cd core C core	117575757.6	0.12000	10.0
Mn core C core	98181818.18	0.12000	10.0
Ni core C core	100606060.6	0.12000	10.0
Zn core C core	89696969.7	0.12000	10.0
Co core C core	95757575.76	0.12000	10.0
Fe core O_w shell	1550.1075	0.26507	10.1
Cd core O_w shell	3117.3763	0.25630	10.1
Mn core O_w shell	1440.6645	0.27268	10.1
Ni core O_w shell	1176.7798	0.26661	10.1
Zn core O_w shell	741.1401	0.28910	10.1
Co core O_w shell	788.8089	0.28630	10.1

4.2. Results and Discussion I: Substitutions on Dry Surfaces

This section details the results of calculations on pure and defective surfaces of dolomite under vacuum conditions. The suitability of the potential parameters described in section 4.1 is demonstrated by comparing the calculated cell parameters and bulk moduli of dolomite and other end-member carbonates with those obtained from experiment. The data (Table 4.2) show that the potentials are able to reproduce the bulk properties of dolomite,

with agreement between lattice parameters being very favourable, lying within 0.7% of the experimental values. Calculated data for the other end member carbonates (Table 4.3) are also in good agreement with experiment and thus the potentials are suitable for simulating carbonate-metal interactions.

Table 4.2: Bulk properties of dolomite

	Literature	This work
Total Lattice Energy / eV	-88.32[†]	-88.29
Bulk Modulus / GPa	91[‡], 94[*]	93.26
a,b / Å	4.81[+]	4.80
c / Å	16.01[+]	15.89
c/a / Å	3.33	3.31
C_{11}[§]	205	198
C_{33}	113	107
C_{44}	39.8	41.2
C_{12}	71.0	75.9
C_{13}	57.4	68.8
C_{14}	-19.5	20.8
C_{15}	13.7	-9.43

[†][14]

[‡][15]

[*] [10] - Computational Study, and references therein

[+][16]

[§][17] – For all elastic constants

The optimised structures of the non-polar surfaces are shown in Figure 4.1. The relaxed surface energies of the dry surfaces are given in Table 4.4 and show that the most stable surface is the $(10\bar{1}4)$, followed by $(10\bar{2}1)$, $(30\bar{3}0)$ and then the $(11\bar{2}0)$ surface. This follows similar trends to those previously reported [13], although the magnitude of the surface energies is slightly lower, and the relative stabilities of the $(10\bar{2}1)$ and the $(30\bar{3}0)$ surfaces are reversed, so that two of the terminations of the $(10\bar{2}1)$ surface are more stable. The relaxation of the $(30\bar{3}0)$ surface involves distortion of the planar carbonate ion in order to stabilise the surface, and this out-of-plane bending is more restricted by the present potential model, which gives a better description of the carbonate ion in under-coordinated environments [8]. The potential was optimised to describe the carbonate ion both in the bulk and in under-coordinated environments such as surfaces, and is the first potential to give the correct ordering for the possible geometries for the $CaCO_3$ monomer, such that the C_{2v} geometry is lower in energy than the C_{3v} [8]. As a consequence of this improved description, which keeps the carbonate ion more rigid with respect to torsion than previous models, the $(30\bar{3}0)$ surface, in which this distortion of planarity is of greater import than at the $(10\bar{2}1)$ surface, will be less stable in comparison.

Table 4.3: Structural and elastic properties for the end-member carbonates from both theoretical calculations and experiment

End-member	Bulk Modulus/ GPa experiment[†]	Bulk Modulus/ GPa this work	a,c/ Å literature[*]	a,c/ Å this work	c/a literature[*]	c/a this work
$CdCO_3$	100	97	4.90, 16.39	4.88, 16.41	3.34	3.36
$CoCO_3$	124	123	4.67, 14.89	4.64,14.88	3.18	3.20
$FeCO_3$	117	120	4.73, 15.25	4.70,15.25	3.22	3.24
$MnCO_3$	108	107	4.78, 15.56	4.76,15.57	3.26	3.27
$NiCO_3$	131	137	4.64, 14.73	4.61, 14.72	3.17	3.19
$ZnCO_3$	123	122	4.67, 14.88	4.64, 14.88	3.19	3.21

[†] [14]

[*] [10] and references therein

Table 4.4: Surface energies for $(10\bar{1}4)$, $(11\bar{2}0)$, $(30\bar{3}0)$ and $(10\bar{2}1)$ surfaces

Surface	γ/ Jm^{-2}
$(10\bar{1}4)$	0.55
$(11\bar{2}0)$	0.89
$(30\bar{3}0)$	0.80
$(10\bar{2}1)_{0.0000}$	0.82
$(10\bar{2}1)_{0.1218}$	0.77
$(10\bar{2}1)_{0.3718}$	0.79
$(10\bar{2}1)_{0.6282}$	0.83

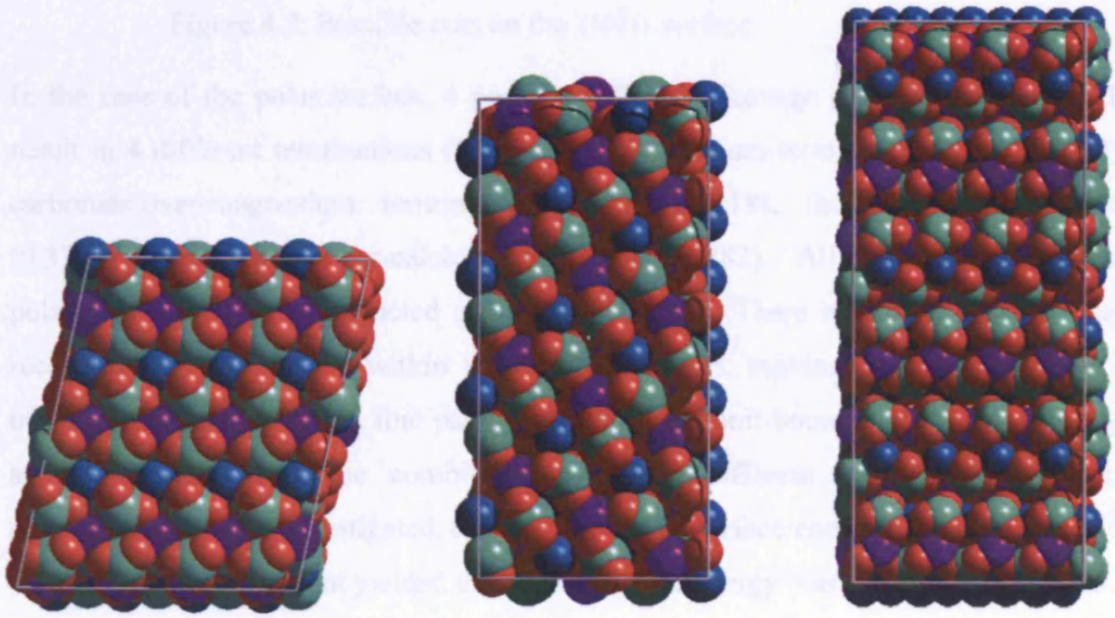

Figure 4.1: Surfaces viewed from above, (left to right) $(10\bar{1}4)$, $(11\bar{2}0)$ and $(30\bar{3}0)$ [Red = Oxygen, Green = Carbon, Purple = Magnesium, Blue = Calcium]

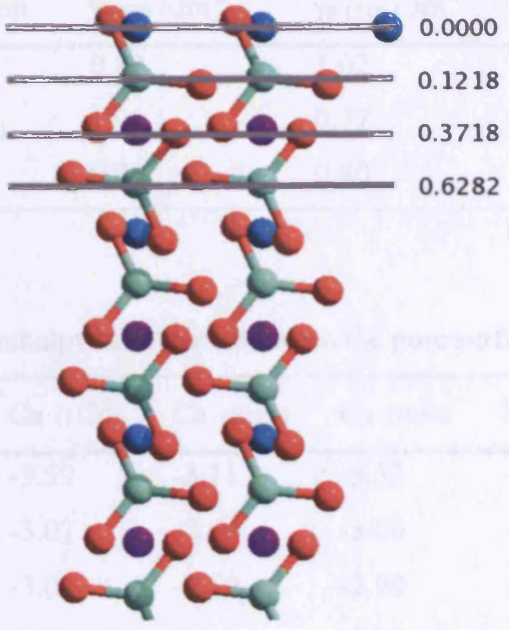

Figure 4.2: Possible cuts on the $(10\bar{2}1)$ surface

In the case of the polar surface, 4 possible different cleavage planes were found. These result in 4 different terminations (Figure 4.2): the calcium-terminated surface (0.000), the carbonate-over-magnesium terminated surface (0.1218), the magnesium terminated (0.3718) and carbonate-over-calcium terminated (0.6282). All of these terminations are polar and must be reconstructed prior to relaxation. There are three possible ways of reconstructing the surface within the 2x1 repeat unit, moving surface ions either in a triangle, denoted as A. in a line parallel to the repeat unit boundaries, B, or in a diagonal across the cell, C. The combination of these different surface terminations and reconstructions were investigated, and the calculated surface energies are reported in Table 4.5. The combination that yielded the lowest surface energy was selected, being the 0.1218 shift and reconstruction B. The 0.3718 shift combined with reconstruction A was also found to have a low surface energy, and investigations were also made upon this surface, so that terminations both with a carbonate at the surface and a cation at the surface were studied.

Table 4.5: Surface energies of the different reconstructions for the $(10\bar{2}1)$ surface

Reconstruction	$\gamma_{0.000}$ / Jm^{-2}	$\gamma_{0.1218}$ / Jm^{-2}	$\gamma_{0.3718}$ / Jm^{-2}	$\gamma_{0.6282}$ / Jm^{-2}
A - row	0.82	1.02	0.99	0.92
B - line	1.01	0.77	0.87	1.00
C - line2	0.98	0.80	0.79	0.83

Table 4.6: Enthalpy difference between the pure surface and the defective surface, in eV

Impurity	Ca $(11\bar{2}0)$	Ca $(10\bar{1}4)$	Ca $(30\bar{3}0)$	Mg $(11\bar{2}0)$	Mg $(10\bar{1}4)$	Mg $(30\bar{3}0)$
Ni	-3.59	-3.11	-3.52	-0.57	-0.65	-0.59
Co	-3.07	-2.61	-3.00	-0.08	-0.10	-0.08
Zn	-3.04	-2.59	-2.98	-0.06	-0.07	-0.06
Fe	-2.71	-2.32	-2.56	0.22	0.32	0.42
Mn	-2.14	-1.80	-1.96	0.73	0.93	1.03
Cd	-1.28	-1.05	-1.08	1.47	1.92	1.97

When comparing the relative energies of the surfaces with and without impurities, a pattern emerges (Table 4.6). The energies are calculated by subtracting the total energy of the pure surface block from the total energy of the surface block containing the cationic defect. The calculations containing impurities at surface calcium sites were found to be consistently lower in energy than the respective pure surface cell, in accordance with earlier work on the $(10\bar{1}4)$ surface [18]. In addition, the degree of cell stabilisation varies with ionic radius of the different cations studied, thus: $Ni^{2+} > Co^{2+} > Zn^{2+} > Fe^{2+} > Mn^{2+} > Cd^{2+}$, adhering to an inverse relationship between cationic radius and a lowering in energy of the surface, which follows the pattern observed in previous studies of defects in calcite in the bulk [10, 19]. It was found that this stabilisation was evident whenever the ionic radius of the impurity cation was smaller than the substituted cation. So, there is stabilisation for substitutions at Mg sites for Ni, Co and Zn, because they have similar ionic radii to the Mg cation, and

stabilisation for all the impurity ions at Ca sites, as they all have smaller radii than the divalent Ca cation. Figure 4.3 shows the substitution energies for the surfaces studied, calculated according to equation 4.4. As shown, the dependency on the ionic radii disappears when considering the exchange of cations in a solid solution, except for substitutions at the calcium site on the $(10\bar{2}1)$, which are unfavourable. The trend is inverted for the $(10\bar{1}4)$ surface, but the substitution enthalpies are also positive for these substitutions.

It is evident, from examination of Figure 4.3, that Cd and Mn substitutions are most favourable at Mg sites on the $(11\bar{2}0)$ surface, and that these ions will also favourably substitute at the Ca site on this surface. Additionally, Zn has a very slightly negative substitution enthalpy for this surface at the calcium site. The substitution of zinc at magnesium sites is also very slightly favourable for the $(30\bar{3}0)$ and $(10\bar{1}4)$ surfaces. The preference for Mn to substitute predominantly at Mg sites in dolomite, but also to substitute at Ca sites, has been observed experimentally [20, 21], supporting the findings in this study. The $(10\bar{2}1)$ surface is not predicted to interact with the impurities according to the model used. The values shown for this surface are for substitutions at the most favourable sites, as the surface Mg sites on both terminations are inequivalent due to the reconstruction. The structures of the surfaces are illustrated in Figure 4.4 and Figure 4.5. For the 0.3718 termination, the magnesium ions sink into the surface on relaxation, resulting in significant stabilisation of the surface, reflected in the 2 eV difference in surface energies between the relaxed and unrelaxed structures. There is a slight preference for substitutions at site 1 over the other two sites. Analysis of the surface geometries shows that this magnesium cation is the least tightly bound of the three, with the largest Mg-O distances for its nearest carbonate ion. The 0.1218 termination has carbonate ions directly on the surface, which cover the surface magnesium ions. It was found that the energies of substitution at sites 1, 4 and 5 were energetically favoured by 1 eV over those at the other 3 sites, and that the substitutions in these two groups of three had equivalent energies. The trend was not, as in the case of the 0.3718 termination, due to the interatomic distances between the Mg ions

and O atoms, but rather it was due to the Mg-C distances. The sites with Mg-C > 2.6 Å have smaller substitution energies than those with Mg-C < 2.6 Å.

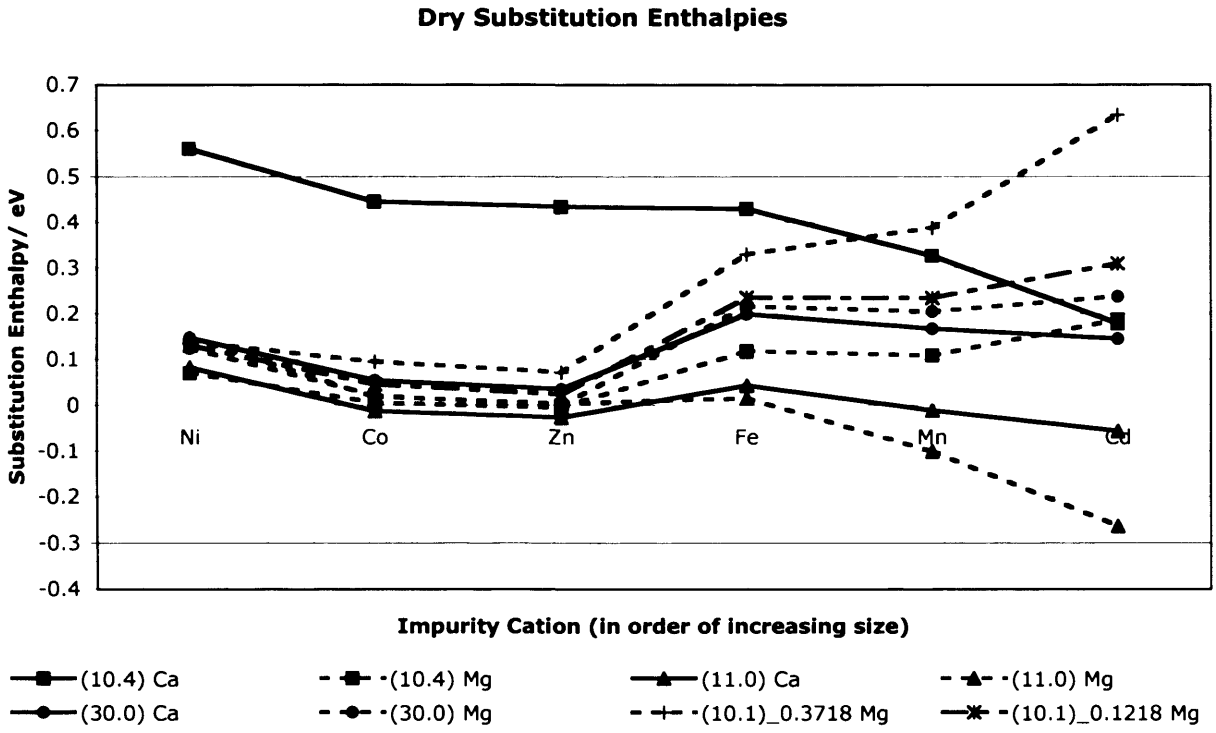

Figure 4.3: Substitution energies for dry dolomite surfaces

Table 4.7: Average cation-nearest neighbour distance

Surface	Average Ca-neighbour distance/ Å	Average Mg–neighbour distance/ Å
$(10\bar{1}4)$	2.39	2.07
$(30\bar{3}0)$	2.35	2.01
$(11\bar{2}0)$	2.41	2.16

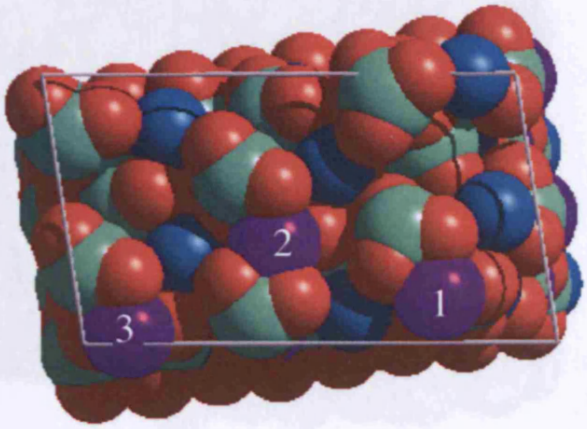

Figure 4.4: View of the relaxed reconstructed $(10\bar{2}1)_{0.3718}$ surface from above

The trend in substitution energy for each non-polar surface can also be explained somewhat by the surface geometries: the distance between the cation and the atoms in its immediate vicinity (Table 4.7) and the differences between pure surfaces and those containing impurities. The $(11\bar{2}0)$ surface is substituted most favourably for Co, Zn, Mn and Cd. The structure of the $(11\bar{2}0)$ surface is the most open, the carbonate ions do not distort over or around a surface cation due to the surface structure. As can be seen from Table 5, the $(11\bar{2}0)$ surface is the most open, especially with respect to the magnesium sites. This has the most importance for the larger cations, and is an explanation for the more negative substitution energies for this surface. The $(30\bar{3}0)$ surface undergoes changes in the orientation of alternate surface carbonate ions near the impurity cations introduced at calcium sites, which leads to a lowering of the surface energy. The extent of this re-orientation is far less at magnesium sites, where substitutions at the more open $(10\bar{1}4)$ surface are preferable to those at the $(30\bar{3}0)$ surface for the larger cations. When multiple substitutions were made at each surface, it was found that there was no marked preference for substitution site for impurity cations relative to each other.

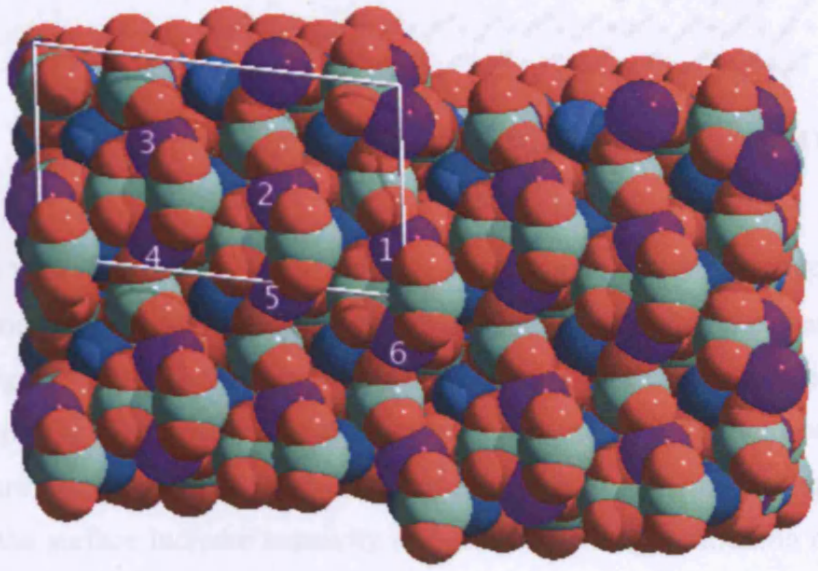

Figure 4.5: View of relaxed $(10\bar{2}1)_{0.1218}$ surface from above

4.3. Stepped surfaces substitutions

Steps were made on the $(10\bar{1}4)$ surface by creating a 2 x 2 supercell and displacing charge neutral units from the surface to the bottom of the simulation block. The most favourable step termination was found to be an acute termination for the carbonate ion at one edge and calcium ions at the opposite edge (Figure 4.6), for which the surface energy was 0.02 Jm^{-2} more stable than the corresponding obtuse terminated structure. This acute terminated configuration was used for the rest of the study into the behaviour of defective surfaces. This finding is in contrast to a recent study using the rigid ion model [22], which found that for calcite the obtuse termination was very slightly (0.04 eV) more favourable than the acute termination. The rigid ion model does not fully describe the polarisability of the carbonate ion, and therefore its behaviour in such an under-coordinated environment as a step edge may not be adequately represented. As the difference in energy between the two surfaces is expected to be small, the inclusion of polarisability could reasonably be expected to affect the relative energetics of the terminations in such a way as that observed.

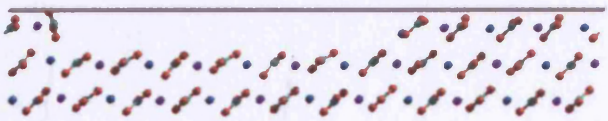

Figure 4.6: Structure of the steps on the $(10\bar{1}4)$ surface

As with the perfect $(10\bar{1}4)$ surface, substitutions at the step edges and terrace follow the same pattern with respect to ionic radius when comparing the energies of the surface units (Figure 4.7). There was, however, a degree of directionality in the substitutions with respect to the favourability of the substitution site. Substitutions on this stepped surface are more exothermic than those on the perfect surface, showing that naturally occurring defects at the surface increase reactivity and cation exchange. Addition of charge neutral units to the step edges were also carried out and it was found, in accordance with previous findings [13, 23] that the addition of one unit to form a kink is slightly energetically unfavourable, but addition of units to complete the step causes a re-stabilization of the surface.

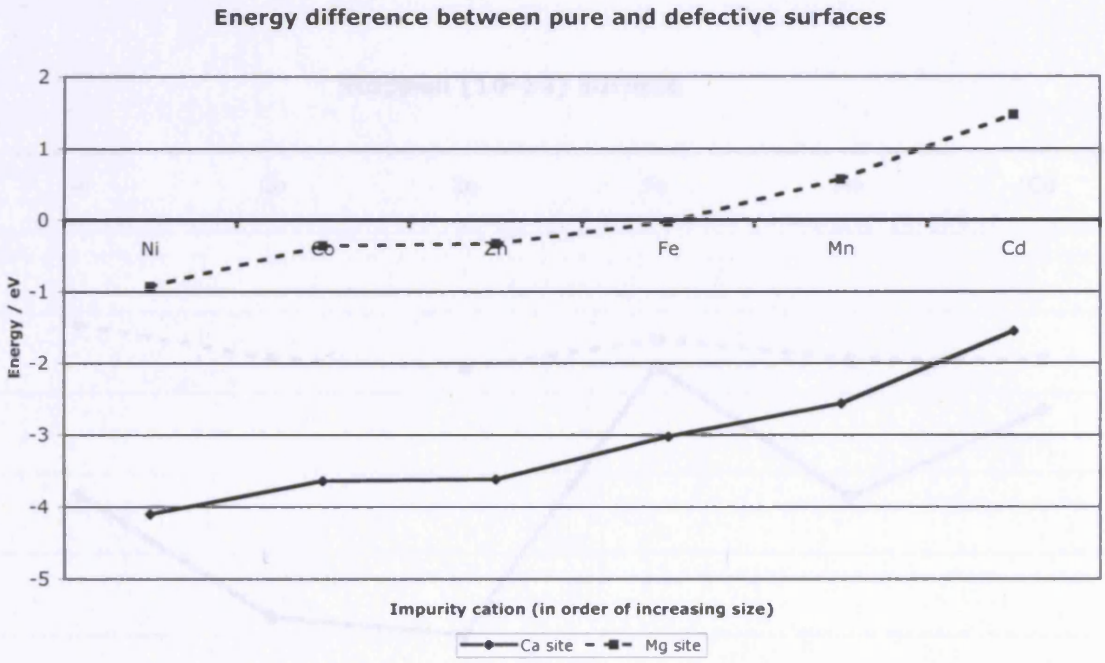

Figure 4.7: The energy difference between pure and defective $(10\bar{1}4)$ stepped surfaces

For calcium site substitutions, it was most favourable to substitute impurity cations at the step edge. Those sites at the other end of the terrace are the next most favourable, and the

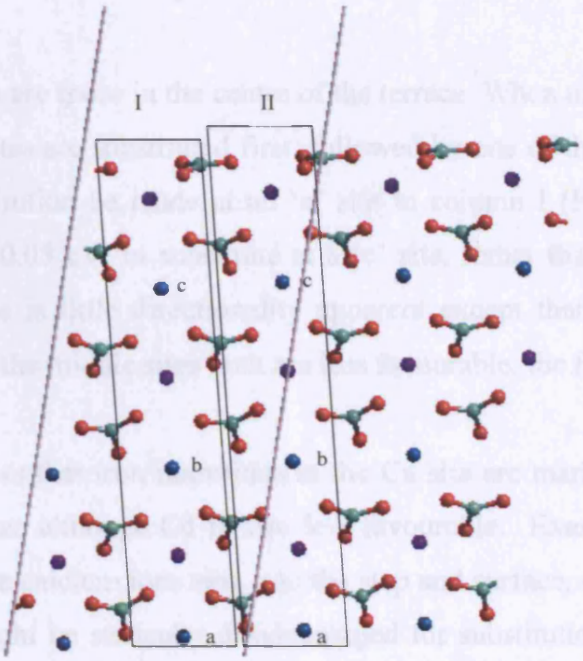

Figure 4.8: Stepped surface from above

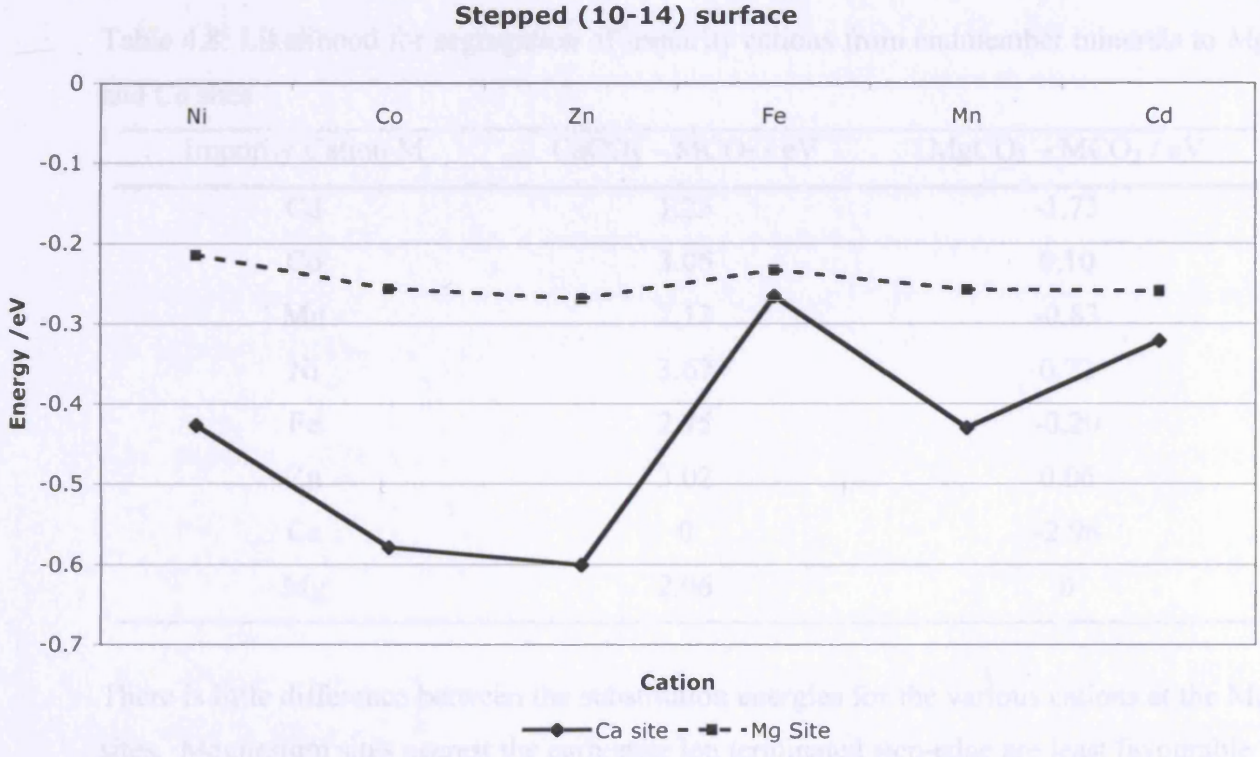

Figure 4.9: Most favourable substitution energies for the $(10\bar{1}4)$ surface with steps

least favourable are those in the centre of the terrace. When multiple substitutions are made, the step edge sites are substituted first, followed by one of the sites furthest from the edge. Should a substitution be made at an 'a' site in column I (Figure 4.8), it is slightly more favourable, by 0.05 eV, to substitute at a 'c' site, rather than at the 'a' site in column II. Thereafter there is little directionality apparent except that the appearance of rows and substitutions at the middle sites both are less favourable, the former more so.

Figure 4.9 shows that iron impurities at the Ca site are markedly less favourable than for the other cations, although Cd is also less favourable. Examination of the surface shows that the step-site calcium ions sink into the step and surface, such that the larger cations Fe, Mn and Cd might be sterically disadvantaged for substitutions at these sites (Figure 4.7), counteracting the fact that they are more likely to segregate from their end-member carbonate minerals (Table 4.8).

Table 4.8: Likelihood for segregation of impurity cations from endmember minerals to Mg and Ca sites

Impurity Cation M	$CaCO_3 - MCO_3$ / eV	$MgCO_3 - MCO_3$ / eV
Cd	1.23	-1.73
Co	3.06	0.10
Mn	2.13	-0.83
Ni	3.67	0.72
Fe	2.75	-0.20
Zn	3.02	0.06
Ca	0	-2.96
Mg	2.96	0

There is little difference between the substitution energies for the various cations at the Mg sites. Magnesium sites nearest the carbonate ion terminated step-edge are least favourable

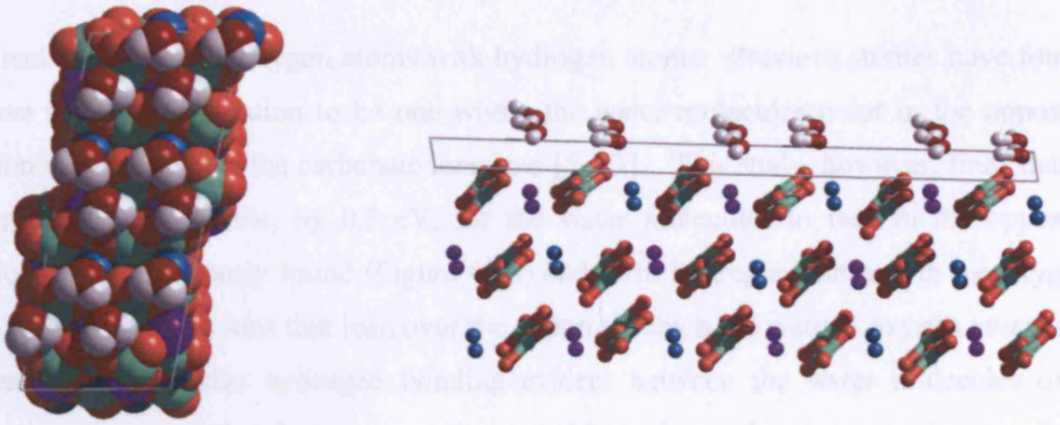

Figure 4.10: Monolayer of water on the $(10\bar{1}4)$ surface of dolomite: Left - from above, right - from the side showing three surface layers. Key: Ca = blue, Mg = purple, O = dark red (water)/ red (carbonate), C = green

for substitution of any cation. It can be seen that there is reorientation of the carbonate ion at the step edge, a phenomenon seen in calcite at step edges with acute carbonate terminations [24]. This reorientation results in a reduction of 1Å in the distance between carbonate oxygen atoms in neighbouring rows, which traps the magnesium ions in their sites. Other than the aforementioned, no significant selectivity has been observed. Multiple substitutions of the larger ions at combinations of Mg and Ca sites show that it is very slightly less favourable, by 0.06 eV, to substitute nearest neighbour sites in columns, all other things being equal. From examination of the relaxed structures it is evident that this is probably due to an increase in unfavourable steric interactions of the larger cations with the carbonate ion that they each flank.

4.4. Results and Discussion II: Substitutions on Wet Surfaces – Monolayer Solvation

In order to study the effect of hydrating the surface, the effect of water was approximated by the addition of a monolayer of water to the $(10\bar{1}4)$ surface, which is the simplest and least computationally expensive approximation, for which a precedent has been set for carbonate mineral surface solvation [18, 25, 26]. The most stable configuration formed 'bands' at the surface (Figure 4.10), via a network of hydrogen bonds between both the

water and the carbonate oxygen atoms with hydrogen atoms. Previous studies have found the most stable configuration to be one where the water molecules point in the opposite direction to that in which the carbonate ions lean [5, 13]. This study, however, finds that it is energetically favourable, by 0.3 eV, for the water molecules to face in the opposite direction to that previously found (Figure 4.10) and form hydrogen bonds with the oxygen atoms on the carbonate ions that lean over the cation to which the water's oxygen atoms are attracted. There is also hydrogen bonding evident between the water molecules over different cations, such that the water oxygen over Mg hydrogen bonds to a hydrogen of the water above Ca, so that the water forms 'bands' along the surface in the same direction as the rows of cations. It is likely that the orientation of the water molecules, and the consequent network of hydrogen bonding, does not have a major influence on the energetics of substitution, as the completion of the coordination of the cations will be the factor with the strongest influence. It should also be noted, that the strong "banding" that is observed is likely to be disrupted by the presence of more water molecules above the monolayer, and as such it must be stressed that the monolayer approximation is just that, a first approximation to the effect of water on the surface, and while it can provide some insight into this problem, its limitations must be remembered in the interpretation of subsequent results.

Upon hydration the surface is stabilised by 0.33 Jm^{-2} giving a surface energy of 0.22 Jm^{-2}. The cations and anions at the dry surface are under-coordinated with respect to their bulk environment, having a coordination number of 5 rather than of 6 respectively. The addition of a monolayer of water results in the 6^{th}, vacant site for each cation being occupied by the water molecule's oxygen atom, so that the surface geometry is expected to more closely correspond to the bulk terminated structure, stabilizing the surface as a consequence.

Substitutions were carried out on the solvated surface in the same manner as at the dry surface. Additionally, Ca and Mg impurities were included, as these cations will be present in the natural aqueous environment due to dolomite dissolution and will be in competition with the other divalent cations [27]. The substitution energies, calculated according to equation 4.7, are reported in Table 4.9. As shown, all the energies are positive, except for

the substitution of a Ca cation at a magnesium site. The preference for this substitution could be the route to magnesian calcite formation and non-stoichiometry in dolomite samples. All energies exhibit the expected behaviour of substitutions being consistently more favourable at the Mg site, which is a result of the more exothermic solvation energy of magnesium in comparison to calcium, -19.0 eV compared to -15.6 eV, which overwhelms the steric preference for calcium site substitution that is particularly important in the case of the larger cations. The self-energy of the water layer was found to be constant, regardless of the impurity substitutions. The substitution energies were found to arise from the interplay between three factors: a) the difference in solvation energies of the cations, b) the difference in the binding energy of the monolayer of water to the surfaces and c) the energetic cost of substituting an impurity at the mineral surface. The self-energy of the water layer, the binding energy of the monolayer to the surface and the overall substitution energy are reported graphically in Figure. 4.11. The relative individual contributions of the three factors that are detailed above to the overall substitution energy in this aqueous model cannot be predicted *a priori* without the use of methods such as those employed in the present study.

The monolayer model has deficiencies when used to approximate bulk water. It is has been shown that in computational studies at least three layers of water should be included in order to describe properly the structure of water at mineral surfaces [28, 29], although experimental evidence for calcite suggests that the effect of the $(10\bar{1}4)$ surface on water structure is less far-reaching, so that there is no observable ordering after the first layer [30]. However, even if the layering, observed in other minerals, is not present at carbonate surfaces, the electrostatic effect of bulk water will considerably affect the energetics of surface substitution. In addition, it is difficult to achieve a minimum for monolayers on rough surfaces, and the use of the current potential model does not allow for the investigation of water dissociation on the surface. It is evident, therefore, that a better description of solvation is necessary if substitution of aqueous species is to be calculated reliably.

Table 4.9: Substitution energies for $(10\bar{1}4)$ surface with a monolayer of water

Cation	E_{subs} Ca site/eV	E_{subs} Mg site/ eV
Cd	1.48	1.06
Co	1.57	0.66
Fe	1.26	0.47
Ni	1.75	0.75
Mn	0.79	0.09
Zn	2.06	1.11
Ca	n/a	-0.27
Mg	0.96	n/a

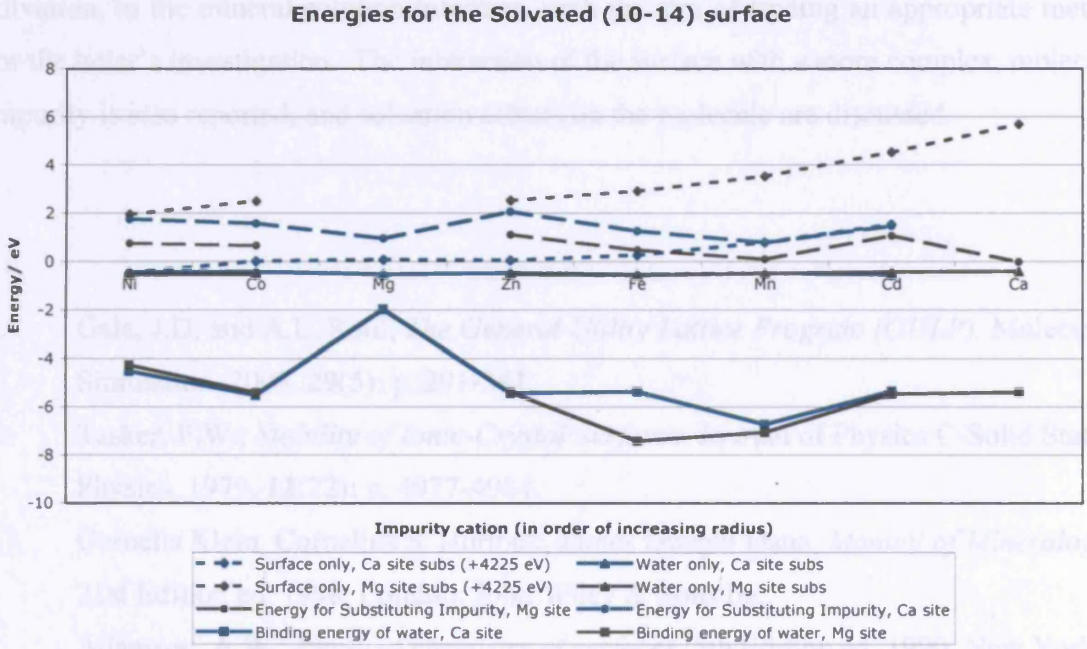

Figure 4.11: Contributions to the energetics of solvated substitutions on the $(10\bar{1}4)$ surface

The results for substitutions modelled in an aqueous environment show that the dry surface substitutions do not contain sufficient information to give qualitative results on the relative cation order of substitution. It is, therefore, important to include a water model when

investigating substitutions at steps. The monolayer model is inapplicable as the stepped surface is too rough and will allow for too many configurations for a minimum to be reached. However, there are other problems with using the monolayer method to solvate a stepped surface. Cations at steps have more freedom to approach their solvated species coordination number, which is often larger than the octahedral coordination afforded by the bulk and surface-monolayer models. The perturbations in the water layer resulting from the step mean that solvation with a monolayer is even more approximate for stepped surfaces than for terraces.

It is evident, from the investigations reported above, that any realistic model of impurity substitution at mineral surfaces must include the effect of water. It is also evident that the monolayer model is severely restricted in its applicability to this problem. The following chapters explore the application of an alternative solvation model, which uses 2D implicit solvation, to the mineral-solution interface, with the aim of finding an appropriate method for the latter's investigation. The interaction of the surface with a more complex, molecular impurity is also reported, and solvation effects on the molecule are discussed.

1. Gale, J.D. and A.L. Rohl, *The General Utility Lattice Program (GULP).* Molecular Simulation, 2003. **29**(5): p. 291-341.
2. Tasker, P.W., *Stability of Ionic-Crystal Surfaces.* Journal of Physics C-Solid State Physics, 1979. **12**(22): p. 4977-4984.
3. Cornelis Klein, Cornelius S. Hurlbut., James Dwight Dana, *Manual of Mineralogy.* 21st Edition ed. 1998, London: John Wiley & Sons Inc.
4. Adamson, A.W., *Physical chemistry of surfaces.* 5th Edition ed. 1990, New York: Wiley.
5. Wright, K., R.T. Cygan, and B. Slater, *Structure of the (10(1)over-bar4) surfaces of calcite, dolomite and magnesite under wet and dry conditions.* Physical Chemistry Chemical Physics, 2001. **3**(5): p. 839-844.

6. de Leeuw, N.H. and S.C. Parker, *Molecular-dynamics simulation of MgO surfaces in liquid water using a shell-model potential for water.* Physical Review B, 1998. **58**(20): p. 13901-13908.
7. Marcus, Y., *Thermodynamics of Solvation of Ions.* Journal of the Chemical Society-Faraday Transactions, 1991. **87**(18): p. 2995-2999.
8. Rohl, A.L., K. Wright, and J.D. Gale, *Evidence from surface phonons for the (2x1) reconstruction of the (10.4) surface of calcite from computer simulation.* American Mineralogist, 2003. **88**(5-6): p. 921-925.
9. Dick, B.G. and A.W. Overhauser, *Theory of the dialectric constants of alkali halide crystals.* Physical Review, 1958. **112**: p. 90-103.
10. Fisler, D.K., J.D. Gale, and R.T. Cygan, *A shell model for the simulation of rhombohedral carbonate minerals and their point defects.* American Mineralogist, 2000. **85**(1): p. 217-224.
11. *CRC Handbook of Chemistry and Physics.* 83rd ed, ed. D.R. Lide. 2002: CRC Press LLC.
12. Woodley, S.M., et al., *Computer-simulation study of the orthorhombic-hexagonal phase change in lanthanide manganates (LnMnO(3)).* Chemistry of Materials, 2003. **15**(8): p. 1669-1675.
13. De Leeuw, N.H., *Surface structures, stabilities, and growth of magnesian calcites: A computational investigation from the perspective of dolomite formation.* American Mineralogist, 2002. **87**(5-6): p. 679-689.
14. Ross, N.L. and R.J. Reeder, *High-Pressure Structural Study of Dolomite and Ankerite.* American Mineralogist, 1992. **77**(3-4): p. 412-421.
15. Zhang, J.Z. and R.J. Reeder, *Comparative compressibilities of calcite-structure carbonates: Deviations from empirical relations.* American Mineralogist, 1999. **84**(5-6): p. 861-870.
16. Martinez, I., J.Z. Zhang, and R.J. Reeder, *In situ X-ray diffraction of aragonite and dolomite at high pressure and high temperature: Evidence for dolomite breakdown to aragonite and magnesite.* American Mineralogist, 1996. **81**(5-6): p. 611-624.
17. Bass, J.D., *A Handbook of Physical Constants: Mineral Physics and Chrystallography*, ed. T.J. Ahrens. Vol. Volume 2. 1995: AGU Reference Shelf.

18. Wright, K., R.T. Cygan, and B. Slater, *Impurities and nonstoichiometry in the bulk and on the (1014) surface of dolomite.* Geochimica Et Cosmochimica Acta, 2002. **66**(14): p. 2541-2546.
19. Cygan, R.T., et al., *Atomistic models of carbonate minerals: Bulk and surface structures, defects, and diffusion.* Molecular Simulation, 2002. **28**(6-7): p. 475-495.
20. Granwehr, J., P.G. Weidler, and A.U. Gehring, *The fate of structure-bound Mn2+ during the decomposition of dolomite and in the resulting conversion products.* Geochimica Et Cosmochimica Acta, 2004. **68**(11): p. A107-A107.
21. Galoisy, L., *Local versus average structure around cations in minerals from spectroscopic and diffraction measurements.* Physics and Chemistry of Minerals, 1996. **23**(4-5): p. 217-225.
22. Duckworth, O.W. and S.T. Martin, *Dissolution rates and pit morphologies of rhombohedral carbonate minerals.* American Mineralogist, 2004. **89**(4): p. 554-563.
23. de Leeuw, N.H., *Molecular dynamics simulations of the growth inhibiting effect of Fe2+, Mg2+, Cd2+, and Sr2+ on calcite crystal growth.* Journal of Physical Chemistry B, 2002. **106**(20): p. 5241-5249.
24. de Leeuw, N.H. and T.G. Cooper, *A computer modeling study of the inhibiting effect of organic adsorbates on calcite crystal growth.* Crystal Growth & Design, 2004. **4**(1): p. 123-133.
25. de Leeuw, N.H. and S.C. Parker, *Surface-water interactions in the dolomite problem.* Physical Chemistry Chemical Physics, 2001. **3**(15): p. 3217-3221.
26. de Leeuw, N.H. and S.C. Parker, *Atomistic simulation of the effect of molecular adsorption of water on the surface structure and energies of calcite surfaces.* Journal of the Chemical Society-Faraday Transactions, 1997. **93**(3): p. 467-475.
27. Stafilov, T., et al., *Determination of trace elements in dolomite and gypsum by atomic absorption spectrometry: overcoming the matrix interference by flotation separation.* Spectrochimica Acta Part B-Atomic Spectroscopy, 2002. **57**(5): p. 907-917.
28. Kerisit, S. and S.C. Parker, *Free energy of adsorption of water and calcium on the (10-14) calcite surface.* Chemical Communications, (1) 2004: p. 52-53.

29. Zhang, C. and P.J.D. Lindan, *Towards a first-principles picture of the oxide-water interface.* Journal of Chemical Physics, 2003. **119**(17): p. 9183-9190.
30. Geissbuhler, P., et al., *Three-dimensional structure of the calcite-water interface by surface X-ray scattering.* Surface Science, 2004. **573**(2): p. 191-203.

5. SOLVATION OF SURFACES: RESULTS OF THE APPLICATION OF IMPLICIT SOLVATION TO SURFACES AND THE EFFECT ON ENERGETICS

"We never know the worth of water 'til the well is dry." Thomas Fuller, 1732.

In Chapter 4 the results of substitutions on dry surfaces and those solvated with a monolayer are reported. It was found that the model could be improved upon by the inclusion of solvation, for which the monolayer was found to be somewhat inadequate and sometimes difficult to implement. The following chapter details the use of a new application of the implicit solvation method to empirically modelled 2-dimensional surface calculations, COSMIC [1].

5.1. Methods Used

The calculations reported here were carried out using the same interatomic potential parameters as those reported in chapter 4. The surface energy, when solvated with COSMIC, is calculated in exactly the same way as that of the dry surface and is given by equation (4.1). There is no need for additional terms and the substitution energy under such conditions can be calculated using equation (4.7). Similarly, the energy of the surface with a monolayer and COSMIC solvation can be calculated using equation (4.6).

When using COSMIC, as with any continuum solvation model, it is important to pay particular attention to the parameterisation of the model. In this study, the atomic radii, the number of points and segments, and the solvent radius and δr were varied to maximise agreement with the Gibb's free energy of solvation reported in Marcus 1991 [2], with the exception of the solvation energy of water, taken from Sefcik and Goddard 2001 [3]. The COSMIC variable parameters used in the calculations are given in Table 5.1. Those calculated for molecules were scaled in the ratio of their van der Waals' radii to achieve the correct solvation energy. The number of points and segments were kept constant in the calculations at 326 and the solvent radius and δr were both held at 1.3 Å. The range for

smoothing was held at 0.2, as prescribed in the COSMIC publication [1]. The radii of the cations are close to their van der Waals' radii, and the reduction in the radii for anions agrees with the findings of Mestres *et al.* who find that the volume of an anion decreases on solvation [4].

Cation	Radius/ Å	Solvation energy from literature /eV	Solvation energy Calc'd /eV
Ca^{2+}	1.8110	-15.598	-15.599
Cd^{2+}	1.5532	-18.189	-18.189
Mg^{2+}	1.4896	-18.966	-18.965
Mn^{2+}	1.5488	-18.241	-18.240
Zn^{2+}	1.3943	-20.262	-20.262
Ni^{2+}	1.3766	-20.521	-20.522
Co^{2+}	1.4233	-19.848	-19.848
Fe^{2+}	1.48136	-19.070	-19.070
C	1.48461	-13.629	-13.629
O (carbonate)	1.327416		
O (water)	1.4400	-0.456	-0.450
H	1.1520		

Table 5.1: Van der Waals' Radii used for COSMIC calculations

The COSMIC model has been applied to two mineralogical problems in order to understand its effect upon crystal surfaces. First, the effect of solvation on the relative energies of surfaces has been assessed by examining the predicted morphologies including and excluding implicit solvation. Second, COSMIC solvation has been applied to the problem of impurity incorporation at surfaces, the results of which calculations are reported in section 5.3.

5.2. COSMIC Solvation: Effects on Morphology

The effect of COSMIC on the relative stability of surfaces was investigated for dolomite by comparing the morphology that is generated from optimised dry surface energies with those using COSMIC solvation. The four morphologically important dolomite surfaces were investigated, the (211), $(10\bar{1})$ $(2\bar{1}\,\bar{1})$ and (100) surfaces, which correspond to the hexagonal unit cell's $(10\bar{1}4)$, $(11\bar{2}0)$, $(30\bar{3}0)$ and $(10\bar{2}1)$ surfaces, respectively. The latter surface from each group is polar, and each of its four possible terminations was studied. The surface energies are given in Table 5.2, both with and without solvation.

Surface	γ_{Dry}/ Jm^{-2}	γ_{Cosmic}/ Jm^{-2}	$\Delta\gamma$/ Jm^{-2}	Solv. E /eV
(211)	0.55	0.12	0.43	-1.08
$(10\bar{1})$	0.89	0.33	0.56	-1.83
$(2\bar{1}\,\bar{1})$	0.80	0.27	0.53	-2.96
$(100)_{0.0000}$	0.97	0.31	0.66	-2.74
$(100)_{0.1218}$	0.79	0.10	0.69	-2.93
$(100)_{0.3824}$	0.80	0.13	0.67	-2.94
$(100)_{0.6175}$	0.84	0.20	0.64	-2.60

Table 5.2: Wet and dry surface energies for dolomite

The resultant wet and dry equilibrium morphologies are given in Figure 5.1. Dolomite usually adopts a unit rhombohedral morphology [5], but Figure 5.1 shows that neither the dry nor the solvated predicted morphologies show a universal expression of the {211} planes that would result in such a crystal habit. The appearance of the $\{2\bar{1}\,\bar{1}\}$ and $\{10\bar{1}\}$ surfaces in the dry morphology can be explained by the lack of solvation in the model, which affects the stability of the surfaces, which will normally be solvated as the crystal develops. However, it would be expected that an improved model, where solvation has been taken into account, would provide a better approximation to the experimentally observed rhombohedral morphology.

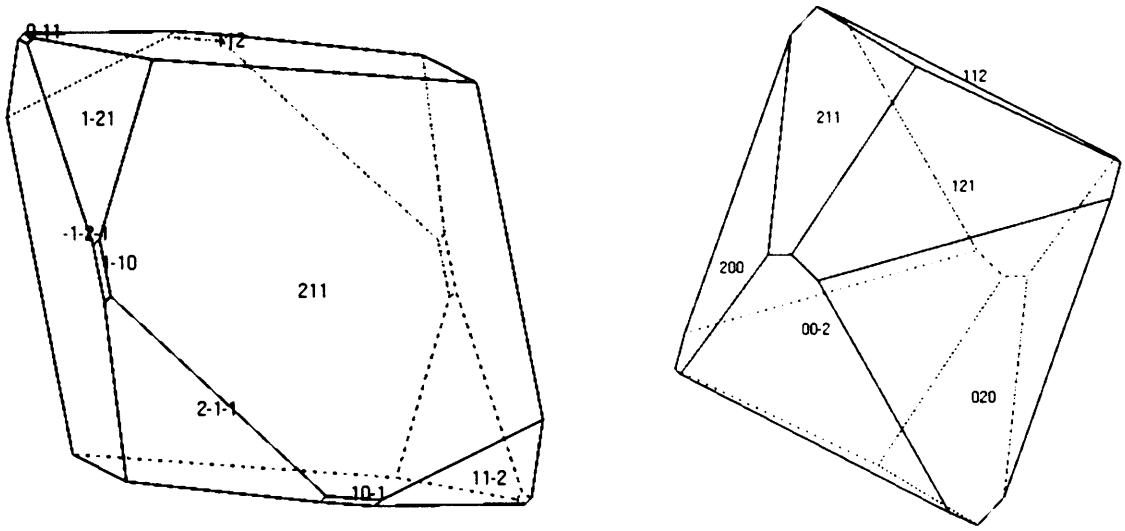

Figure 5.1: Left – Dry equilibrium morphology; Right – Wet (COSMIC) equilibrium morphology

The possible explanations for the differences between the observed morphologies and that predicted by the calculations using COSMIC will now be explored. The first relates to the mechanism by which the crystal grows in nature. The equilibrium morphology, which results from the relative surface energies, reflects the morphology reached by a crystal when in equilibrium with its surroundings and, consequently, under thermodynamic control. Many geological samples are represented more accurately by the growth morphology, which is constructed from the attachment energy and shows the morphology under kinetic control. However, the growth morphology, which is kinetically controlled, is difficult to predict when solvating the structure as the attachment energy has a spurious meaning. This problem is complicated by the "dolomite problem", as it is extremely difficult to grow dolomite under ambient laboratory conditions [6]; due to the uncertainty about the method by which dolomite came into existence in the environment, it is not necessarily the case that the shape of available geological crystals was determined by the relative surface energies, and laboratory samples of the crystal at equilibrium with its surroundings cannot be found:

> After running an experiment for 32 years that unsuccessfully attempted to precipitate dolomite at 25°C, Land (1998) came to the...conclusion, "...we? all agree that the 'Dolomite Problem' is one of kinetics.". [6](citing [7])

There is also an argument that stoichiometric dolomite occurs only after some time, due to Ostwald ripening, where non-stoichiometric dolomite precipitates initially and is thereafter replaced by stoichiometric dolomite over time. In this case, the morphology might be influenced not just by either the surface energy or attachment energies of dolomite, but the crystal habit might be strongly influenced by the non-stoichiometric precursor. Unfortunately, it is beyond the capabilities of this study to provide so sophisticated a model for the prediction of the crystal morphology.

The second explanation is that the (211) $[(10\bar{1}4)]$ surface of calcite has been observed to extend ordering to at least the first layer of water [8], and it is to be expected that the dolomite would affect the water structure in the same manner. In this case, it is possible that the COSMIC model would prove inadequate for modelling solvation of surfaces at which this strong, directional ordering occurs. Additionally, it is possible that some water dissociation could occur on some surfaces, which, if present, could lead to variations in the relative stabilities of surfaces and the explicit nature of which would not be modelled by an implicit solvation model.

As a possible source of error in the calculations, and in order to understand the effect of varying the relative van der Waals' radii for the C and O of the carbonate ion, a number of different values were tested, all of which still maintained the correct solvation energy for the carbonate molecule. It could be conjectured that the oxygen atom radius is more important in the solvation of the carbonate ion than that of the carbon atom. As such, the oxygen radius was systematically increased, and the carbon radius decreased, whilst still achieving the correct solvation energy for the ion, overall. The aim was to increase the oxygen radius to a size as close as possible to its actual van der Waals' radius of 1.36 Å [9]. A selection of these alternative values were used in calculations of the energies of the (211) and (100) surfaces (Table 5.3), which are in competition with each other in the solvated morphologies. However, as inspection of the values for the radii in Table 5.3 shows, the solvation energy was far more sensitive to the oxygen radius than the carbon radius, so that

any increase in the former required a much greater, compensatory decrease in the latter. Consequently, the largest value tested for oxygen was 1.3448Å, corresponding to a carbon radius of 1Å. Decreasing the carbon radius further was considered to create a wholly unrealistic model for the overall ion. It was found that, for each of the radius combinations considered, at least one of the polar surface terminations was always as stable as the (211) surface. Comparison of the relevant dry and solvated surface energies (Table 5.2) shows that the stabilisation afforded by the COSMIC model is greater for the polar surface terminations than any of the non-polar surfaces. The largest stabilisation for a non-polar surface is a lowering of the surface energy by 0.56 Jm^{-2} on the $(10\bar{1})$ surface. However, the largest solvation energy for non-polar surfaces is for the $(2\bar{1}\,\bar{1})$ surface, which shows the greatest degree of atomic roughness (Figure 5.2). As there is no strict correlation between the change in surface energy and the solvation energy, it is evident that a contributing factor to the final, solvated surface energy is surface geometry reconstruction on application of solvation.

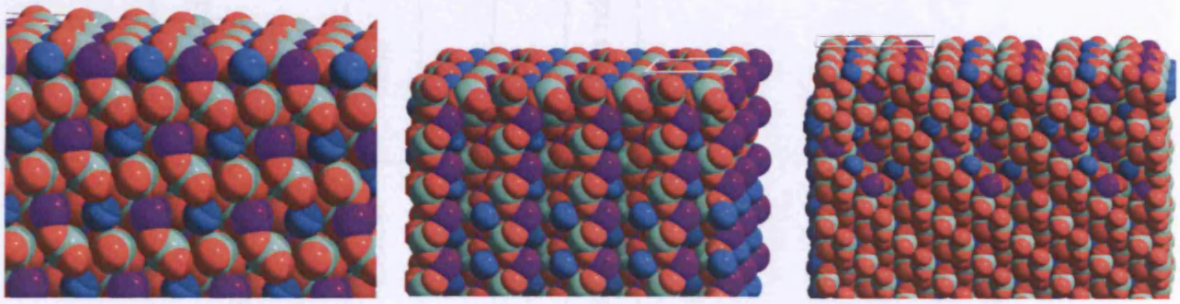

Figure 5.2: Relaxed surfaces of the solvated, non-polar surfaces of dolomite. Left –right: (211), $(10\bar{1})$ and $(2\bar{1}\,\bar{1})$

O radius/ Å	C radius/ Å	CO_3^{2-} Solvation Energy / eV	γ_{Cosmic}/ Jm^{-2} (211)	γ_{Cosmic}/ Jm^{-2} $(100)_{0.0000}$	γ_{Cosmic}/ Jm^{-2} $(100)_{0.1218}$	γ_{Cosmic}/ Jm^{-2} $(100)_{0.3824}$	γ_{Cosmic}/ Jm^{-2} $(100)_{0.6175}$
1.33	1.463	-13.630	0.12	0.31	0.11	Failed	0.22
1.3388	1.34	-13.628	0.11		0.12		
1.3448	1.00	-13.629	0.12	0.32	0.20	0.13	0.20

Table 5.3: Effect of C and O van der Waals' radii on relative surface energies

The degree of stabilisation for the polar surfaces using the COSMIC model is far greater than that reported for them using monolayer solvation [10], where the $(10\bar{1}4)$ surface remains the most stable under both dry and monolayer-solvated conditions. A Wulff plot was created using only the energies of the non-polar surfaces of dolomite, when solvated (Figure 5.3) and, in this case, exhibits the rhombohedral habit. The correlation between the degree of stabilisation and the atomic roughness of the surface, together with the rougher surface of the (100) surface due to reconstruction, when viewed in conjunction with literature results for monolayer solvation [10], suggests that there may be some over-stabilisation of the polar surface with the COSMIC model that is due to surface geometry. In order to investigate further the effect of the COSMIC model on polar surfaces, the (111), another viable, polar surface of dolomite was modelled. The van der Waals' radii given in Table 5.1 were used in the calculations. The surface energies for the four possible terminations are given in Table 5.4. The surface block was converged at R1=37Å and R2=21Å, and a 2x1 supercell was used for the calculations. The surface was reconstructed as previously detailed (Ch 4).

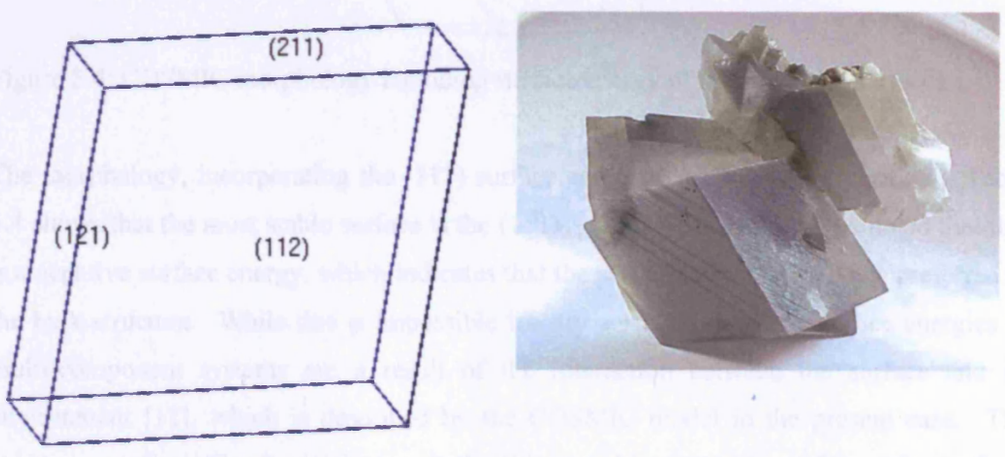

Figure 5.3: Morphology derived from surface energy of solvated, non-polar surfaces (Left) and a rhombohedral dolomite crystal from Eugui, Spain [11]

Table 5.4: Surface energies of dry and solvated (111) surface terminations

Surface	γ_{Dry}/ Jm^{-2}	γ_{Cosmic}/ Jm^{-2}	Solvation Energy /eV
$(111)_{0.0000}$	0.98	0.29	-2.26
$(111)_{0.1345}$	0.82	-0.02	-2.90
$(111)_{0.3845}$	0.90	0.13	-2.72
$(111)_{0.6155}$	0.95	0.23	-2.18

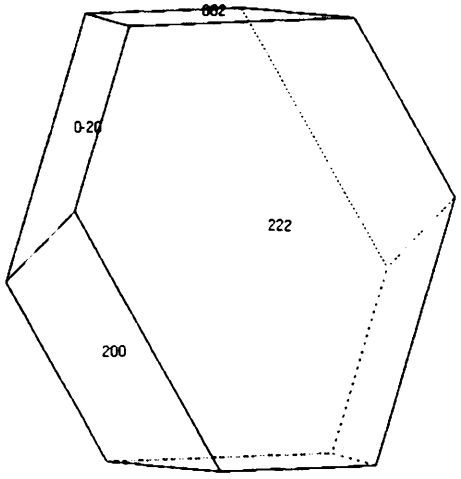

Figure 5.4: COSMIC morphology including surface energy of the two polar surfaces

The morphology, incorporating the (111) surface energies, is shown in Figure 5.4. Table 5.4 shows that the most stable surface is the $(111)_{0.1345}$ surface. It should be noted that this is a negative surface energy, which indicates that the surface, when solvated, is preferred to the bulk structure. While this is impossible for dry surfaces, negative surface energies in multi-component systems are a result of the interaction between the surface and its environment [12], which is described by the COSMIC model in the present case. The $(111)_{0.1345}$ surface, like the $(100)_{0.1218}$, is the CO_3 over Mg termination of the polar surface. Comparison of the relaxed, cation-terminated and carbonate-terminated structures of these (111) and (100) surfaces show that the cation-terminated surfaces are smoother because the cations are able to sink into the surface upon relaxation (Figure 5.5). In the case of both of the polar surfaces, the second-most stabilised surface is the Mg-terminated structure, and it

seems that the contribution of the Mg^{2+} cation's solvation energy to the surface stabilisation, which is far more negative than that of Ca^{2+}, is considerable.

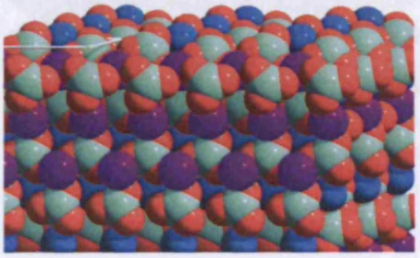

$(100)_{0.0000}$

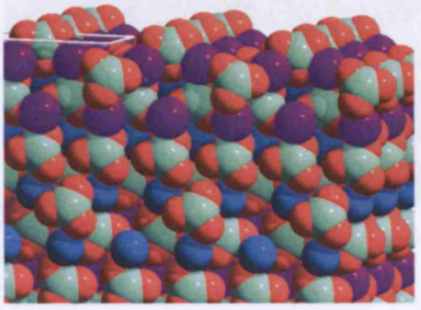

$(100)_{0.1218}$

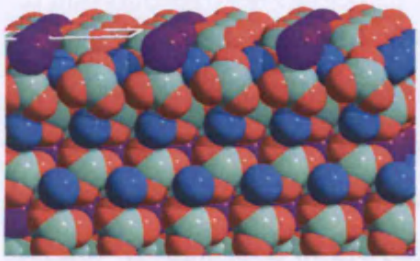

$(100)_{0.3824}$

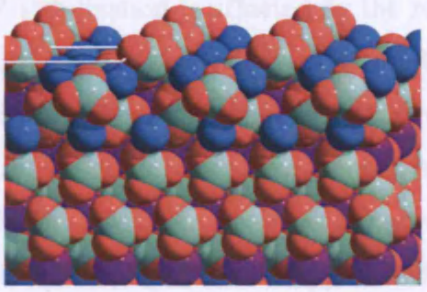

$(100)_{0.6175}$

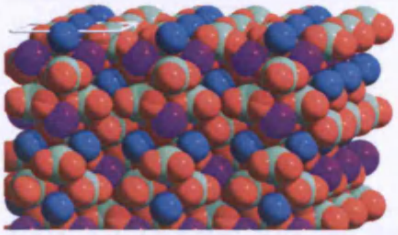

$(111)_{0.0000}$

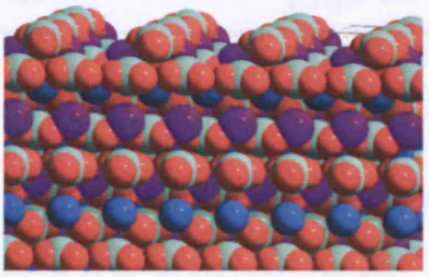

$(111)_{0.1345}$

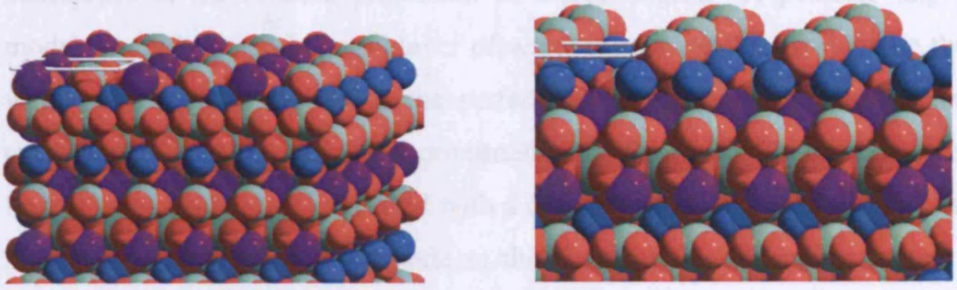

$(111)_{0.3845}$ $(111)_{0.6155}$

Figure 5.5: Relaxed terminations of the polar surfaces of dolomite, showing the roughness of the surfaces.

In order to confirm whether the degree of stabilisation is affected by the roughness of the surface, the surface energies of steps on the (211) surface were compared before and after application of the COSMIC model (Table 5.5). The main difference between the stepped surfaces and the (211) terrace is the degree of perturbation; the stepped surface is much rougher due to surface defects, but the ratio of Ca:Mg:CO_3 is almost the same as the perfect surface. Examination of the data in Table 5.5 shows that the stepped surfaces undergo a large drop in surface energy when solvated with COSMIC, and once again the surface with the most accessible magnesium ion is the most stable.

Step Termination	γ_{Dry}/ Jm^{-2}	γ_{Cosmic}/ Jm^{-2}
Ca, acute CO_3	0.82	0.01
Mg, acute CO_3	0.81	-0.04
Obtuse CO_3, Ca	0.85	0.11
Obtuse CO_3, Mg	0.84	0.03

Table 5.5: Dry and Solvated surface energies of steps on the (211) surface

Thus, the stabilisation of a surface is increased by a) its roughness, which reflects a bigger accessible surface area for solvation per unit surface area, and possibly better accessibility

to surface oxygen atoms, and b) the availability of Mg^{2+} ions at the surface. There appears to be over-stabilisation of rough surfaces using the COSMIC model, which leads to difficulties in the reliable prediction of morphologies. A possible improvement to the model would be to add a monolayer of water to each surface to simulate the rigidity of the water structure directly above the surface, although this would be beyond the scope of current work. As a further approximation to this end, the four most morphologically important surfaces were modelled with a dielectric constant of 10, rather than the 78.4 used previously. The lower value reflects the fact that the dielectric constant decreases as a smooth function from bulk water to its more bound state at the surface, aiming to reproduce the existence of the monolayer without having to model it explicitly.

The surface energies derived when the dielectric constant is 10 are reported in Table 5.6, and the resulting morphology is shown in Figure 5.6. Comparison with Figure 5.3 shows that the morphology is nearer to the observed geological morphology when the surfaces are surrounded with a solvent of ε=10. However, this is a slightly unrealistic model, as the entire solvent is treated as having a dielectric constant of 10, just as setting ε=78.4 is unrepresentative of the value for water near the surface. This model, however, while providing some level of improvement for the relative surface energies, cannot be used when substituting impurities at the surface, as the solvation energies for cations will be relative to a solvent with a dielectric constant of approximately 78.

Surface	γ_{Cosmic}/ Jm^{-2}	Solv. E /eV
$(21\bar{1})$	0.17	-0.94
$(10\bar{1})$	0.41	-1.57
$(2\bar{1}\,\bar{1})$	0.35	-2.42
$(100)_{0.0000}$	0.41	-2.62
$(100)_{0.1218}$	0.26	-2.05
$(100)_{0.3824}$	0.23	-2.41
$(100)_{0.6175}$	0.30	-2.13

Table 5.6: Surface and solvation energies when using ε=10

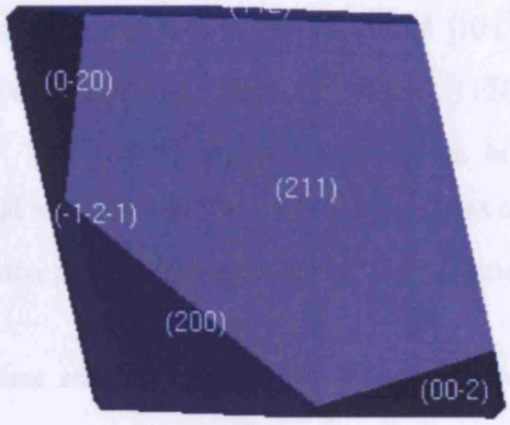

Figure 5.6: Morphology of the surface solvated with a solvent of ε=10

The application of the COSMIC solvation model to a system for which there are available reliable, equilibrium morphologies for the purpose of comparison would provide further insights into the application of the model to the modelling of mineral surfaces. However, despite these difficulties, the model appears to behave well for the non-polar surfaces, and its applicability to the problem of impurity incorporation at surfaces has been tested and will be reported in the following section. The results of this section show that the problems of comparison of relative surface energies should be borne in mind when analysing impurity substitution data gathered using the COSMIC model.

5.3. COSMIC Solvation: Effect on Impurity Substitution

In the previous section the effect of the COSMIC method of solvation [1] was discussed in the context of its application to crystal morphology prediction. In this section the method's effect on the energetics of impurity substitution will be discussed. For the purposes of investigating impurity substitutions, the surface was solvated both with COSMIC alone and, where possible, with COSMIC plus a monolayer of explicit water molecules

immediately above the surface. The monolayer configuration was determined in the same manner as described previously (Ch. 3, Section 3.7.1.1). Substitutions of the divalent cations were carried out on the (211) and $(10\bar{1})$ surfaces, constructed from the primitive unit cell, corresponding to the $(10\bar{1}4)$ and $(11\bar{2}0)$ surfaces, respectively, in Miller-Bravais indices. The $(10\bar{1}4)$ surface was chosen because it is the predominant surface in geological samples, and the $(11\bar{2}0)$ surface was chosen because this is the surface that most readily incorporated impurities under dry conditions (Ch. 4).

The surface energies for the (211) surface solvated with COSMIC, with and without a monolayer, and the $(10\bar{1})$ surface with COSMIC only, are given in Table 5.7. Calculations of the surface with a monolayer coverage could only be minimised for the (211) surface. The surface energy for the monolayer + COSMIC solvated (211) is calculated using equation (4.6), where the energy of the hydrated surface incorporates not just the monolayer, but also the effect of the implicit solvation. The solvation energy of the surface for the monolayer + COSMIC calculation is calculated thus:

$$U_{solvation} = U_{SurfWet} - (U_{SurfDry} + nU_{H_2O_{(l)}}) \tag{5.1}$$

Table 5.7: Surface and solvation energies for the solvated (211) and $(10\bar{1})$ surfaces

Surface and Solvation type	γ /Jm^{-2}	Solvation energy / eV
(211) + COSMIC	0.12	-1.08
(211) + Monolayer + COSMIC	0.08	-0.27 surface -0.13 monolayer
$(10\bar{1})$ + COSMIC	0.33	-1.83

When compared to the values in Table 4.4, it is evident that there has been considerable stabilisation of the surfaces on addition of the continuum solvation model, and that this effect is increased by the addition of monolayer solvation to the (211) surface. The solvation energy of the monolayer is smaller than that of the bare surface, which is to be

expected when comparing the solvation energies of the components of the surface and that of the water molecule, but which would also be expected to have a less stabilising effect on the surface. The stabilisation of the surface in the latter case, therefore, must be a consequence of the explicit interatomic interactions between the monolayer and the surface, which will fill the otherwise incomplete cation octahedral coordination sphere. In chapter 4 the energy of the surface with a monolayer was reported as 0.22 Jm^{-2}, which corresponds to a solvation energy of –0.16 eV (-15.4 $kJmol^{-1}$). This value is much less negative than de Leeuw's value of –85.8 $kJmol^{-1}$ for the hydration of the $(10\bar{1}4)$ surface [10]. However, there is no definition of the derivation of the literature value, so it is possible that the numbers may not be directly comparable. Additionally, the larger value was derived using an earlier potential model, which was not parameterised to model the carbonate-cation interaction in an under-coordinated environment, such as the surface.

Table 5.8 shows the substitution energies when surfaces are solvated with COSMIC for divalent cation impurities on the $(21\bar{1})$ surface, with and without a monolayer of water, and on the $(10\bar{1})$ surface.

Surface	Site	Substitution energy / eV							
		Cd	Mn	Fe	Zn	Co	Ni	Mg	Ca
$(21\bar{1})$ Cosmic	Mg	1.05	0.16	0.32	1.17	0.72	0.84		-0.24
	Ca	1.31	0.67	0.97	1.89	1.46	1.62	0.71	
$(21\bar{1})$ Monolayer+ Cosmic	Mg	1.09	0.03	0.27	1.11	0.38	0.48		-0.55
	Ca	1.55	0.51	1.05	2.04	1.28	1.41	0.65	
$(10\bar{1})$ Cosmic	Mg	0.68	0.05	0.38	1.27	0.78	0.90		-0.59
	Ca	1.50	0.60	0.84	1.77	1.43	1.59	0.49	

Table 5.8: Substitution energetics of solvated surfaces

The data in Table 5.8 show that on all surfaces it is favourable to incorporate Ca at an Mg site, and that the $(10\bar{1})$ is the more favourable than the $(21\bar{1})$ for this substitution.

Comparison of the order in energetics of substitution between the (211) surface solvated with COSMIC and with COSMIC + a monolayer and the $(10\bar{1}4)$ surface solvated by a monolayer shows that the substitution energies at the Mg site follow the same pattern, regardless of the solvation method, but the magnitudes of the energies are different, which is also the case for the more favourable Ca site substitutions. Examination of the graphical representation of the results (Figure 5.7) in conjunction with Table 5.8 shows that in all cases, the impurity cations with the most favourable substitution energies are Mg at the Ca site, Ca at the Mg site, and Mn and Fe at both sites. The substitution energies for incorporation of Mn at the Mg site on both the $(10\bar{1})$ and the (211) surface (COSMIC + monolayer) are extremely small, and such substitutions could conceivably occur.

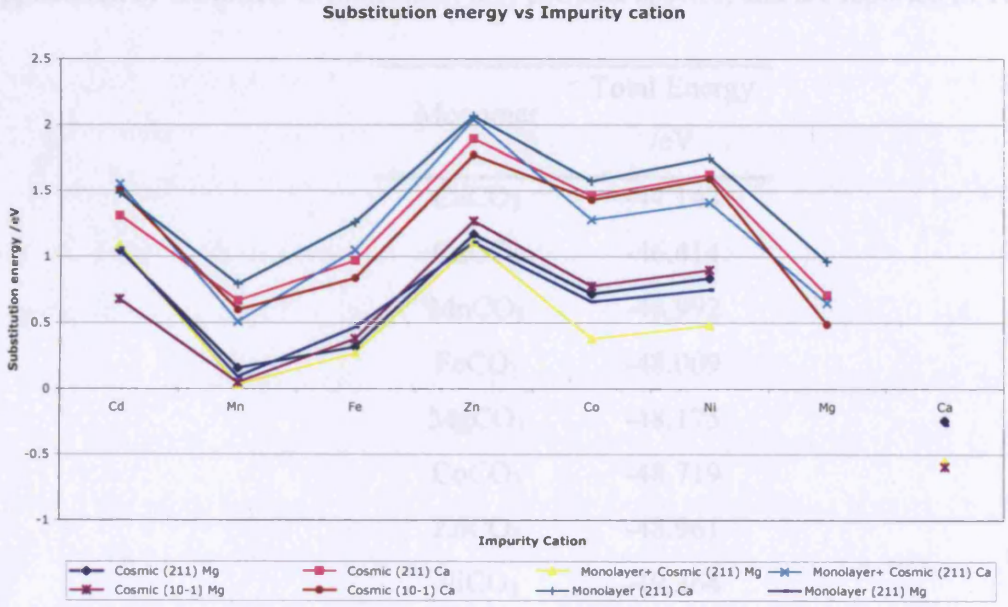

Figure 5.7: Graphical representation of the substitution energy as a function of impurity cation and the solvation model applied to the surface

Addition of a monolayer to the COSMIC solvated (211) surface almost universally decreases the substitution energy at the Mg site and increases it at the Ca site, indicating that the explicit description of water is necessary for the energetic differences between the Ca and Mg site substitutions to be modelled adequately. It is to be expected that the

addition of a monolayer of water to the $(10\bar{1})$ would have a similar effect on the substitution energetics, and it is likely that this would result in a negative substitution energy for Mn at the Mg site, which is observed experimentally [13, 14].

Given the problems with the representation of very rough surfaces with the COSMIC model, stepped surfaces were not investigated using this method of solvation. The model of the surface-solution interface was extended, however, to incorporate the possibility of monomer substitution at the surface. For the surfaces already considered, the substitution energy was calculated for the replacement of a $CaCO_3$ or $MgCO_3$ monomer at the surface with an MCO_3 monomer (M=Ca, Cd, Co, Fe, Ni, Mg Mn, Zn) in solution. The total energies for the monomers were calculated using COSMO in the GULP code, the application of COSMIC to molecular, non-periodic species, and are reported in Table 5.9.

Monomer	Total Energy /eV
$CaCO_3$	-44.143
$CdCO_3$	-46.414
$MnCO_3$	-46.992
$FeCO_3$	-48.009
$MgCO_3$	-48.175
$CoCO_3$	-48.719
$ZnCO_3$	-48.961
$NiCO_3$	-49.364

Table 5.9: Total energy of metal-carbonate monomers

Table 5.10: Substitution energies for monomer substitution at surfaces

Surface	Site	Substitution energy / eV							
		Cd	Mn	Fe	Zn	Co	Ni	Mg	Ca
Cosmic $(2\bar{1}1)$	Mg	0.07	-0.3	0.06	0.66	0.38	0.47		-0.9
	Ca	0.99	0.88	1.37	2.05	1.78	1.92	1.37	
Monolayer+ Cosmic $(2\bar{1}1)$	Mg	0.11	-0.43	0	0.6	0.04	0.12		-1.21
	Ca	1.23	0.71	1.44	2.19	1.61	1.71	1.31	
Cosmic $(10\bar{1})$	Mg	-0.3	-0.4	0.11	0.76	0.45	0.53		-1.25
	Ca	1.18	0.81	1.23	1.92	1.76	1.89	1.16	

Substitutions of monomers (Table 5.10) are shown to be energetically favourable for the Mn substitutions at Mg sites for both the surfaces investigated and for both types of solvation, and for Cd substitutions at Mg sites on the $(10\bar{1})$ surface. The addition of a monolayer of water increases the favourability of the substitution for the $(2\bar{1}1)$ surface, but when comparing the $(2\bar{1}1)$ and $(10\bar{1})$ surfaces solvated with COSMIC it is clear that Mg ions on the $(10\bar{1})$ surface will more favourably be substituted than those on the $(2\bar{1}1)$ surface by larger cations. Comparison with Figure 4.3 shows that the $(11\bar{2}0)/(10\bar{1})$ surface remains the surface upon which Cd and Mn impurity incorporation is most favourable, but that the inclusion of solvation and monomer substitution into the model reverses the preference for Cd and Mn substitutions. It is evident from both the monomer and cation substitution results that, in thermodynamic terms, substitution of Mg for Mn from aqueous solution is a viable method for the incorporation of this impurity transition metal into the mineral, a conclusion supported by experimental observations [13]. Additionally, it has been shown to be favourable to incorporate Ca at Mg sites on both the studied surfaces. This indicates that calcite or disordered magnesian calcite is more energetically favourable at the surface. Such a finding supports Warren's hypothesis for dolomite growth [6], which suggests that disordered magnesian calcite precipitates initially during dolomite growth and

is subsequently replaced by stoichiometric dolomite. To clarify this, it would be informative to generate a large supercell and subsequently carry out a series of site-specific substitutions for Ca at Mg sites for various percentages of coverage, in order to investigate the preferred degree of disorder at the surface. It would also be useful to investigate the growth of Ca and Mg monomers at step sites. Previous work on the growth at calcite steps, using MD simulation of the growth under solvated conditions, shows that $MgCO_3$ incorporation is energetically more favourable than that of $CaCO_3$. The growth of stoichiometric dolomite was not predicted but the growth of magnesian calcite was explained on thermodynamic grounds, at low Mg concentrations [10, 15]. Further investigation of step growth with the aid of COSMIC may lead to better understanding of the growth mechanism of dolomite.

It should be noted that the current model does not include the kinetic barriers to incorporation of either the cations or the monomers at the surface, and the thermodynamic driving force may not be great enough to overcome the activation energy of these substitutions. This is especially the case for monomers, where an extremely specific orientation is necessary for the substitution to go ahead. Kinetic effects of the barriers for approach of solvated Mg, Ca and Sr ions to the calcite surface have been studied in recent MD simulations [16, 17], where the barrier for Mg approach to the surface is less than that for the other ions. The authors attribute this to the more negative solvation energy for the Mg^{2+} ion and its smaller solvated coordination number. Application of a similar technique to dolomite surfaces could yield interesting information and help to complete the mineral-solution interface model. However, there are some limitations to the technique as it stands. These results were gained from MD using interatomic potentials, which conflict with experimental results as to the degree of imposed ordering on the solvent by the surface [8]. As this ordering is of fundamental importance to the kinetic information gained from the simulations, there is obviously scope for the improvement of this model, either by the generation of a potential that accords with experimental results on the ordering above the surface, or by QMMD calculations. Similarly, dissociation of water at the dolomite surface has not been conclusively studied, and if present this could strongly affect the behaviour of solvated species near the surface.

1. Gale, J.D. and A.L. Rohl, *An efficient technique for the prediction of solvent-dependent morphology: The COSMIC method.* In Preparation.
2. Marcus, Y., *Thermodynamics of Solvation of Ions.* Journal of the Chemical Society-Faraday Transactions, 1991. **87**(18): p. 2995-2999.
3. Sefcik, J. and W.A. Goddard, *Thermochemistry of silicic acid deprotonation: Comparison of gas-phase and solvated DFT calculations to experiment.* Geochimica Et Cosmochimica Acta, 2001. **65**(24): p. 4435-4443.
4. Mestres, J., et al., *Effect of solvation on the charge distribution of a series of anionic, neutral, and cationic species. A quantum molecular similarity study.* Journal Of Physical Chemistry, 1996. **100**(2): p. 606-610.
5. Cornelis Klein, C.D.A.H., James Dwight Dana, *Manual of Mineralogy.* 21st Edition ed. 1998, London: John Wiley & Sons Inc. .
6. Warren, J., *Dolomite: occurrence, evolution and economically important associations.* Earth-Science Reviews, 2000. **52**(1-3): p. 1-81.
7. Land, L.S., *Failure to precipitate dolomite at 25 degrees C from dilute solution despite 1000-fold oversaturation after 32 years.* Aquatic Geochemistry, 1998. **4**(3-4): p. 361-368.
8. Geissbuhler, P., et al., *Three-dimensional structure of the calcite-water interface by surface X-ray scattering.* Surface Science, 2004. **573**(2): p. 191-203.
9. *CRC Handbook of Chemistry and Physics.* 83rd ed, ed. D.R. Lide. 2002: CRC Press LLC.
10. De Leeuw, N.H., *Surface structures, stabilities, and growth of magnesian calcites: A computational investigation from the perspective of dolomite formation.* American Mineralogist, 2002. **87**(5-6): p. 679-689.
11. http://www.lhconklin.com/Gallery%20I/Eugui%20Dolomite.htm.
12. Mathur, A., P. Sharma, and R.C. Cammarata, *Negative surface energy - Clearing up confusion.* Nature Materials, 2005. **4**(3): p. 186-186.

13. Granwehr, J., P.G. Weidler, and A.U. Gehring, *The fate of structure-bound Mn2+ during the decomposition of dolomite and in the resulting conversion products.* Geochimica Et Cosmochimica Acta, 2004. **68**(11): p. A107-A107.
14. Lumsden, D.N. and R.V. Lloyd, *Mn(Ii) Partitioning Between Calcium And Magnesium Sites In Studies Of Dolomite Origin.* Geochimica Et Cosmochimica Acta, 1984. **48**(9): p. 1861-1865.
15. de Leeuw, N.H. and S.C. Parker, *Surface-water interactions in the dolomite problem.* Physical Chemistry Chemical Physics, 2001. **3**(15): p. 3217-3221.
16. Kerisit, S. and S.C. Parker, *Free energy of adsorption of water and calcium on the (10-14) calcite surface.* ChemComm, 2004: p. 52-53.
17. Kerisit, S. and S.C. Parker, *Free energy of adsorption of water and metal ions on the {1014} calcite surface.* Journal of the American Chemical Society, 2004. **126**(32): p. 10152-10161.

6. RESULTS OF ELECTRONIC STRUCTURE CALCULATIONS

"The problems of language here are really serious. We wish to speak in some way about the structure of atoms... But we cannot speak about atoms in ordinary language."
Werner Heisenberg, 'Physics and Philosophy', 1958.

In the previous chapters, the results are reported of investigations into the reactivity of carbonate surfaces with the use of interatomic potential methods and static geometry optimisations. Water has been approximated, initially by the inclusion into the calculations of a monolayer of water and subsequently by the COSMIC model. An obvious improvement on previously utilised models is the explicit description of water, for which a dynamic simulation is necessary in order to sample the many configurations possible for the liquid state. The following chapter reports the results of the application of continuum solvation to, and quantum mechanical molecular dynamics (QMMD) simulations of, a more complex impurity than the metal cations studied previously, the arsenate molecule [$AsO(OH)_3$] and its relevant deprotonated anion. The molecule has been studied both in a vacuum and in solution, and subsequently preliminary calculations have been made of its adsorption at the dolomite surface in the vacuum. It had been hoped, when starting this series of calculations, to be able to characterize the adsorption behaviour of arsenate ions near dolomite under environmentally-relevant conditions. Initial work has been carried out on simulating the dolomite surface with explicit solvation. The statistical sampling obtained from these large calculations is not good enough to extract data with confidence and as such the results will not be presented here. However, while constraints on time and CPU power have prevented full-scale calculations of the system, various components have been modelled separately, and insights into the mineral – water interface drawn in the light of the results obtained.

6.1. Arsenate and Its Structure

The structure of arsenate has been investigated with the use of a variety of electronic structure methods: HF, MP2 and DFT. The importance of solvation was investigated through the inclusion of the Conductor-like Polarisable Continuum Model (CPCM) [1] and gauged by comparison of the calculated Raman frequencies and bond lengths with those from experiment. Finally, two molecular dynamics simulations were carried out, one on a cluster comprised of one arsenate molecule and 8 water molecules, the other on a simulation box containing one arsenate molecule and 110 water molecules. All calculations were carried out using the Gaussian03 [2] program, except the arsenate in water simulation box, for which the SIESTA [3] code was used, due to its efficiency for periodic systems. An attempt was made to carry out a molecular dynamics simulation on the cluster surrounded by continuum solvation, so that the electrostatic effects of bulk water could be incorporated into the calculation. Unfortunately this was not possible using Gaussian03 [2], due to an acknowledged bug in the code. Attempts were made to use the NWChem code [4] for the same purpose, but this code also contained a bug in the continuum solvation part, so these attempts were also unsuccessful.

Table 6.1: Energies of high and low spin arsenate complexes

Species and Spin State		Total Energy in vacuum/ a.u.
AsO_4^{3-}	high	--
	low	-2537.33
AsO_4H^{2-}	high	-2537.37
	low	-2537.47
$AsO_4H_2^-$	high	-2538.08
	low	-2538.20
AsO_4H_3	high	-2538.66
	low	-2538.77

The energies of arsenate in various degrees of protonation were investigated by energy minimisation of high and low spin complexes. Of course, the low spin complexes would be the ground state configuration, which is confirmed by the results in Table 6.1. The difference in the energies between high and low spin complexes represent the difference in energy between the ground and excited states of the complexes. In all cases, the energy difference is sufficiently large, and a transition from the low to the high spin state would require flipping one electron's spin, which would have a high kinetic barrier. Therefore, the high spin complex will not be significant in an environmental context. All calculations hereafter were carried out on low spin complexes, as these will be the complexes of interest in nature. The calculation on the high spin AsO_4^{3-} complex could not reach convergence due to its high instability due to its unlikely chemical state. The B3LYP [5-7] functional was used with a 6-311+G(3df,2p) basis set for these calculations.

6.1.1. Effect of Solvation on the Raman Spectra and Energetics of Arsenate

Arsenate was studied both in vacuum and with implicit solvation. A precedent has been set for gauging the validity of a computational model by calculating the Raman spectrum of a complex [8]. The Raman spectra were calculated and compared with experimental data [9]. The calculations were run using Gaussian03 [2] at the B3LYP/6-311+G(3df,2p) level of theory, and CPCM was used for the implicit solvation. The dielectric constant used for water was 78.39, and default radii were used, according to the United Atom Topological Model [10]. The solvation energy for each of the protonated species, derived using the CPCM, is given in Table 6.2. The solvation energies become far less negative with increasing protonation, a trend observed also in the solvation of arsenite ions [8]. In the following section, the solvation energy will be calculated for the arsenate molecule in water, as derived from a molecular dynamics calculation, and this result is in agreement with the magnitude of the results for $AsO_4H_2^-$ and AsO_4H_3 shown below. These values are larger than those reported for arsenite ($As(OH)_3$ and its ions)[8], due to the presence of the additional oxygen atom in the complex, a trend seen also in the solvation energies of organic molecules [11]. The result for AsO_4^{3-} is rather large, even given the proportional relationship between ionic charge and solvation energy. This could be due to an excess of

delocalisation of charge on the solvent accessible surface, leading to an overestimation of the solvent energy. Whilst the CPCM is a parameterisable model, there are no experimental values available for the solvation energy of arsenate. The agreement between the solvation energy from the MD calculations reported in section 6.1.2 and those in Table 6.2 show that the model is well parameterised for the more protonated species, which are the species of interest at the point of zero charge of dolomite, pH neutral.

Arsenate Species	Solvation Energy / eV
AsO_4^{3-}	-21.1
AsO_4H^{2-}	-9.9
$AsO_4H_2^-$	-3.8
AsO_4H_3	-1.1

Table 6.2: Solvation energies for arsenate in varying degrees of protonation

Figure 6.1 shows the Raman spectra obtained from two simulations, one of AsO_4^{3-} molecule in vacuum, and the second of the molecule solvated with the CPCM. It is evident from comparison of the experimental and simulated spectra, that there is a degeneracy of two vibrations in the gas-phase spectrum, which results in a single peak at 350 cm^{-1}. The peaks at the higher values are shifted further towards the experimentally observed values when the molecular ion is solvated with CPCM. The highest vibration, ν_s As-O, is observed experimentally at 818 cm^{-1} [9], whereas it is calculated to occur at 757 cm^{-1} and 707 cm^{-1} for the solvated and gaseous calculations respectively. An important feature of this spectrum is the inversion of the usual behaviour of tetrahedral ions because the symmetric stretching mode is at a higher wavenumber than the triply degenerate asymmetric stretches. This behaviour is reflected in both the gaseous and solvated vibrational frequencies, although the gaseous values are too low by about 100 cm^{-1} for both the symmetric and asymmetric stretches.

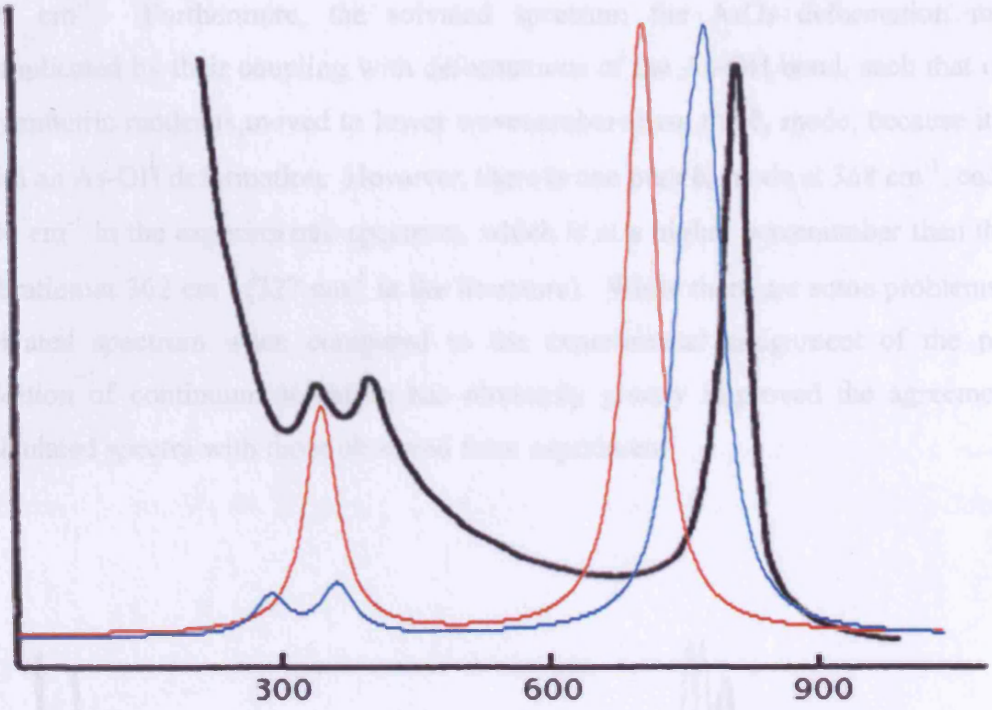

Fig 6.1: Raman Spectra for AsO_4^{3-}. Red: Dry simulated spectrum, Blue: CPCM Solvation added, Black: Experimental spectrum [9]

Figure 6.2 shows a similar improvement in the Raman spectrum on the addition of implicit solvation to AsO_4H^{2-}. The shoulder in the dry spectrum, at around 835 cm^{-1}, disappears, which is due to a larger difference in the value of the symmetric and asymmetric stretching vibrations in the gaseous values (ν_s = 790 cm^{-1}, ν_a = 826 cm^{-1} and 842 cm^{-1}) and the solvated values (ν_s = 801 cm^{-1}, ν_a = 815 cm^{-1} and 824 cm^{-1}). The peak at 981 cm^{-1} in the gaseous spectrum is due to an As-OH wagging vibration that is not observed in the experimental or solvated spectra. The As-O(H) ν_s vibration is at a much lower wavenumber for the dry spectrum than the solvated, although it is still too low by about 140 cm^{-1} (564 cm^{-1} compared to the experimental value of 707 cm^{-1}). The deformation vibrations, δ_s and δ_a are swapped around in the dry spectrum when compared to the experimental assignment, which places the δ_a, doubly degenerate AsO_3 deformation at higher wavenumbers than the singly degenerate, δ_s deformation. In the dry spectrum, the δ_a vibrations are not only at lower wavenumbers than the symmetric deformation, but they

are 100 cm^{-1} apart and are separated by an As-O wagging vibration at a central point of 297 cm^{-1}. Furthermore, the solvated spectrum the AsO_3 deformation modes are complicated by their coupling with deformations of the As-OH bond, such that one of the asymmetric modes is moved to lower wavenumbers than the δ_s mode, because it is mixed with an As-OH deformation. However, there is one pure δ_a mode at 368 cm^{-1}, compared to 380 cm^{-1} in the experimental spectrum, which is at a higher wavenumber than the pure δ_s vibration at 362 cm^{-1} (327 cm^{-1} in the literature). While there are some problems with the solvated spectrum when compared to the experimental assignment of the peaks, the addition of continuum solvation has obviously greatly improved the agreement of the calculated spectra with those observed from experiment.

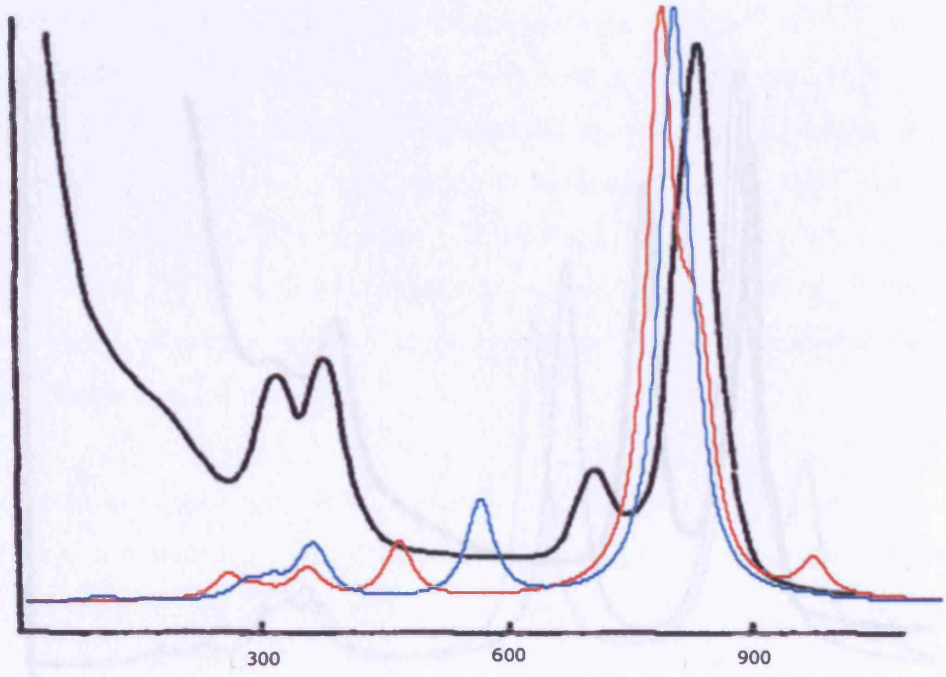

Fig 6.2: Raman Spectra for AsO_4H^{2-}. Red: Dry simulated spectrum, Blue: CPCM Solvation added, Black: Experimental spectrum [9]

The Raman spectrum for $AsO_4H_2^-$ (Fig 6.3) shows great improvement upon the addition of the CPCM. The ν_a and ν_s AsO_2 vibrations become 30 cm^{-1} closer upon the addition of the CPCM; the ν_a vibration moves to a lower wavenumber, from 948 cm^{-1} to 906 cm^{-1}, in much closer agreement with the literature value of 915 cm^{-1}. The proximity of the ν_a and ν_s peaks in the solvated spectrum results in the shoulder observed also in the experimental spectrum. Thus, the addition of the CPCM remedies the presence of the peak at 948 cm^{-1} in the dry spectrum. The order of the stretching vibrations of the $As(O(H))_2$ is reversed in the dry spectrum, and the addition of CPCM does not change this. However, upon the inclusion of CPCM the wavenumbers of the vibrations are increased, and the degeneracy in the gaseous spectrum is removed, resulting in better accordance with the experimental values. The small peak in the dry spectrum at around 1000 cm^{-1} is due to a symmetric and

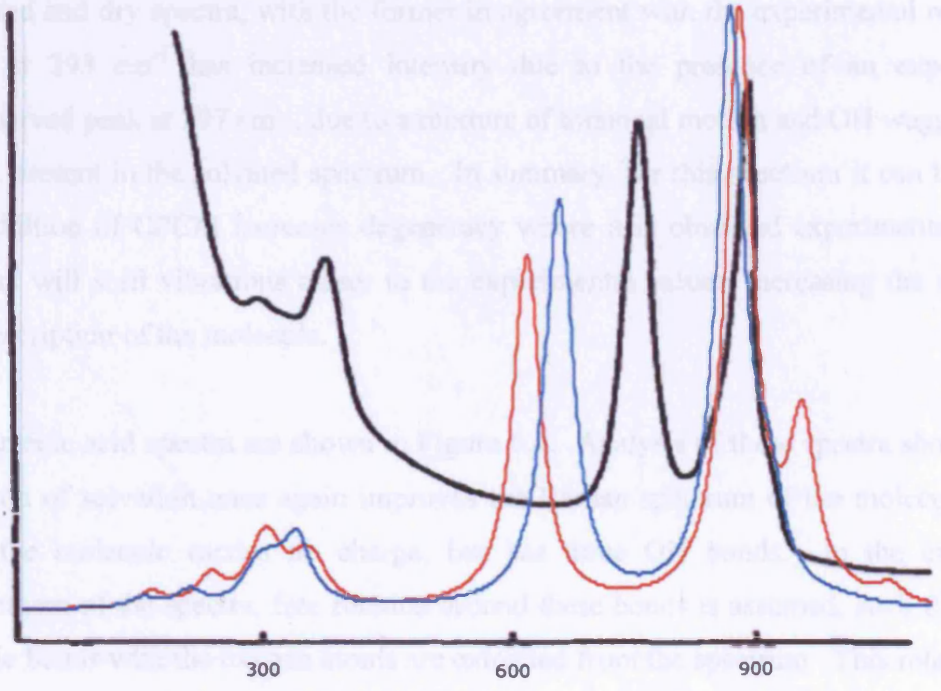

Fig 6.3: Raman Spectra for $AsO_4H_2^-$. Red: Dry simulated spectrum, Blue: CPCM Solvation added, Black: Experimental spectrum [9]

asymmetric bending around the As-O-H angle, something that is unlikely to be observed in experimental spectra at room temperature, as under these conditions the barrier to rotation of the hydroxyls around the As-O bonds would be negligible. In contrast to this, the calculations are geometry optimisations carried out at the athermal limit, and as such the barrier to rotation will be far more significant.

The degeneracy in the peaks at the lower end of the spectrum in Figure 6.3 increase with the addition of implicit solvation, concurring with the experimental results, where an overlap of the $As(OH)_2$ wagging, AsO_2 wagging and AsO_2 bending modes is observed at 365 cm^{-1}. In the solvated spectrum, these peaks are at 308 cm^{-1}, 338 cm^{-1} and 335 cm^{-1} respectively. Similarly, in the dry spectrum the same peaks are at 309 cm^{-1}, 345 cm^{-1} and 361 cm^{-1}, showing a much more marked difference in the values than exhibited in the solvated spectrum. The ordering of the peaks below 500 cm^{-1} is reversed between the solvated and dry spectra, with the former in agreement with the experimental results. The peak at 293 cm^{-1} has increased intensity due to the presence of an experimentally unobserved peak at 297 cm^{-1}, due to a mixture of torsional motion and OH wagging, which is not present in the solvated spectrum. In summary, for this spectrum it can be seen that the addition of CPCM increases degeneracy where it is observed experimentally, and in general will shift vibrations closer to the experimental values, increasing the accuracy of the description of the molecule.

The arsenic acid spectra are shown in Figure 6.4. Analysis of these spectra shows that the addition of solvation once again improves the Raman spectrum of the molecule. In this case the molecule carries no charge, but has three OH bonds. In the experimental assignment of the spectra, free rotation around these bonds is assumed, such that only the arsenic bonds with the oxygen atoms are extracted from the spectrum. This rotation results in six fundamental vibrations, three of which are degenerate. For the gaseous molecule, it is difficult to isolate the identity of the vibrations at lower wavenumbers, as they are affected by the inclusion of some OH vibrations. However, these lower wavenumber vibrations, corresponding to the deformational modes, are clearer for the solvated spectrum

and have the correct value and intensity. The two $As(OH)_3$ rocking vibrations, experimentally observed at 350 cm^{-1}, are too low by around 50 cm^{-1} for both the solvated and dry spectra, although the observed degeneracy is preserved. The ordering of the $As(OH)_3$ asymmetric and symmetric stretching modes is correct for both calculated spectra, although the values are closer to experiment for the solvated spectrum. This is also the case for the AsO stretch, which is 923 cm^{-1} experimentally, and the addition of solvation to the model reduces it from 982 cm^{-1} to 941 cm^{-1}. The low-intensity peak above 1000 cm^{-1} in the dry spectrum is due to hydroxyl vibrations that were not observed experimentally, as discussed previously. Similarly, the calculated spectra are unable to reproduce the small peak at 881 cm^{-1} in the experimental spectrum, as this is assigned to polymeric vibrations within the solution and was observed to disappear at lower concentrations. Obviously, the calculation of an isolated molecule will not capture this peak.

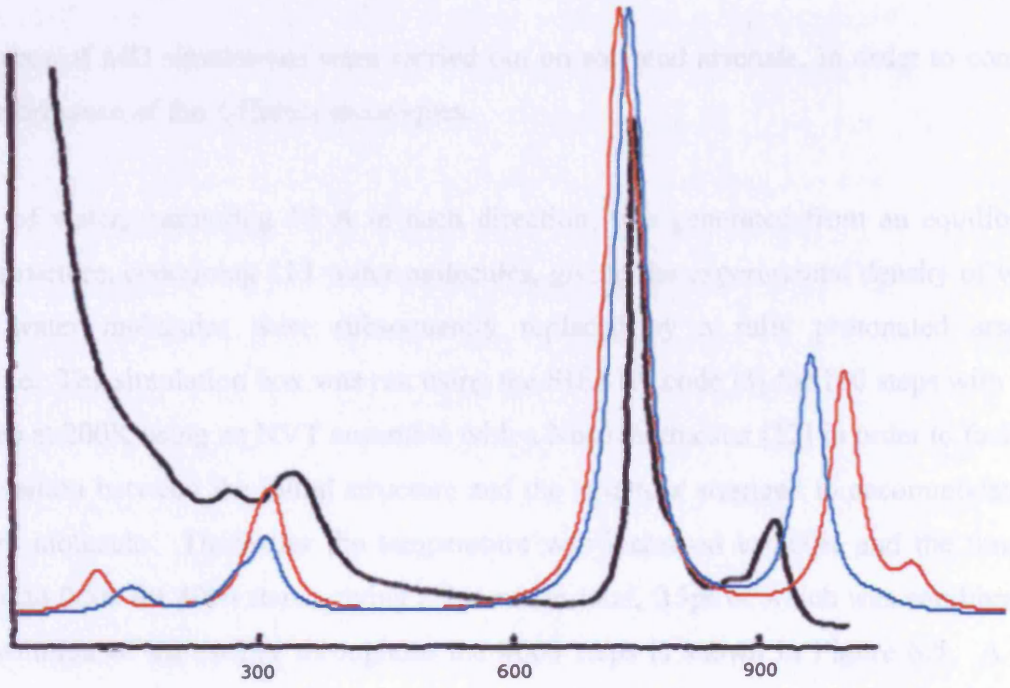

Fig 6.4: Raman Spectra for AsO_4H_3. Red: Dry simulated spectrum, Blue: CPCM Solvation added, Black: Experimental spectrum [9]

The results of these solvated and dry calculations show that the behaviour of the molecules cannot be accurately modelled without incorporation of some of the solvation effects. As a first approximation, the addition of the CPCM helps to produce Raman spectra in better accordance with the experimental data. The conclusion can be drawn that models neglecting the effect of solvation are inadequate in the case of solvated molecules. This inadequacy will be of equal, if not greater, importance when considering the interaction of the molecules with surfaces, as there are two components in such systems that interact with the solution. For such complex systems, it is of paramount importance to include solvation effects, whether explicitly or implicitly, once preliminary gas phase calculations have been carried out to find likely starting geometries. The following sections examine the explicit description of water around the arsenic acid molecule, and compares the results from MD calculations on the explicitly solvated molecule with those from this section.

6.1.2. Results of Molecular Dynamics Calculations on Arsenate

Two types of MD simulations were carried out on solvated arsenate, in order to compare the performance of the different techniques.

A box of water, measuring 15 Å in each direction, was generated from an equilibrated water structure, containing 113 water molecules, giving the experimental density of water. Three water molecules were subsequently replaced by a fully protonated arsenate molecule. The simulation box was run using the SIESTA code [3] for 100 steps with a 1fs timestep at 200K using an NVT ensemble with a Nosé thermostat [12] in order to facilitate the transition between the initial structure and the structure arranged to accommodate the arsenate molecule. Thereafter the temperature was increased to 300K and the timestep reduced to 0.5fs for 4000 steps, giving a 2ps run in total, 0.5ps of which was equilibration. The evolution of the energy throughout the 4000 steps is shown in Figure 6.5. A DZP basis set was used for the calculations along with the PBE functional [13], and Troullier-Martins [14] pseudopotentials were used for each of the elements present in the calculations.

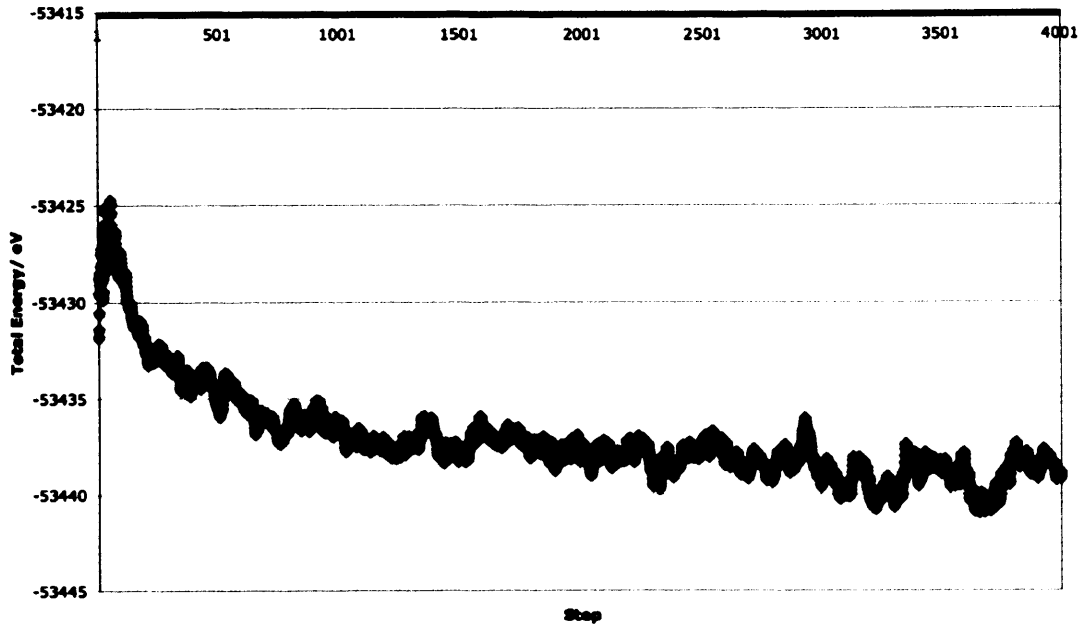

Figure 6.5: Evolution of the total energy during the final 4000 steps of the MD run

The radial distribution function (RDF) between arsenic and oxygen, calculated per step of the production period of the simulation, is shown in Figure 6.6. The radial distance shown in Figure 6.6 is limited to 4.65Å because the box size was not big enough to allow reliable data to be taken beyond this point. The RDF shows that there is no appreciable ordering of the oxygen atoms around the arsenic atom except for the four oxygen atoms belonging to the arsenate molecule. Observation of the simulation shows that the arsenate molecule loses one proton during the equilibration phase, and occasionally a second proton detaches from the molecule. This is to be expected, as at the conditions of neutral pH that were simulated in this instance the arsenate molecule is present as the $[AsO_2(OH)_2]^-$. The detached arsenate proton initiates proton transfer according to the Grötthus mechanism [15, 16], where proton transfer to form H_3O^+ leads to the loss of a different proton from the complex, which thereafter transfers to a different water molecule to form another H_3O^+ ion, and so the proton transfer continues. It would be interesting to run a longer simulation with the arsenate in a larger box of water, to observe the trajectory of the proton, and to see if a larger water box will result in ordering of water molecules around the arsenate molecule, which has not been observed in this simulation. Such calculations are, however, beyond the scope of this work.

Figure 6.6 shows the average bond length of the molecule in water to be between 1.7 and 1.9Å, which is slightly longer than the range of those observed from previous theoretical calculations (As-O = 1.63Å, As-OH = 1.81Å) [17]. However, the aforementioned study used a polarised SBK basis set in Gaussian94, rather than the DZP basis set used in this study, and included only 4 water molecules as an approximation to solvation. The presence of bulk water around the arsenate molecule will affect the bond lengths via a combination of electrostatics and more extensive H-bonding. The calculations reported in Section 6.1.1 give bond lengths for the gaseous molecule of As-O = 1.62Å and As-OH = 1.74Å, and for the solvated molecule of As-O = 1.63Å and As-OH = 1.74 Å. It must also be remembered that the molecule loses a proton during the simulation, so that the bond lengths for consideration are those of the $AsO_4H_2^-$. The application of the CPCM lengthens the As-O bonds while shortening the As-OH bonds. This model, however, does not take into account any explicit hydrogen bonding, which will change the bond lengths. Additionally, the bond lengths from the SIESTA calculation are an average over the simulation at 300K and over the four bonds present, which are both As-O and AsOH bonds, whereas the values in the literature are from a static geometry optimisation, which incorporates no temperature effects. Theoretically, it would have been possible to extract Raman frequencies, although not intensities, from the atomic vibrations taking place throughout the simulation. However, it was considered that there were too few simulation steps for such a procedure and that the errors on the data gleaned would be too great to warrant the analysis. Raman spectra depend on the bond lengths and strengths, so the effect of these longer bonds would be to shift the frequencies in the spectra to lower wavenumbers, as can be seen from the results shown in Section 6.1.1, for example the decrease of the frequency of the As-O bond in $AsO_4H_2^-$ on addition of CPCM (Figure 6.3). However, it is not possible to predict further the appearance of the spectrum, as the strength of the bond cannot be easily determined.

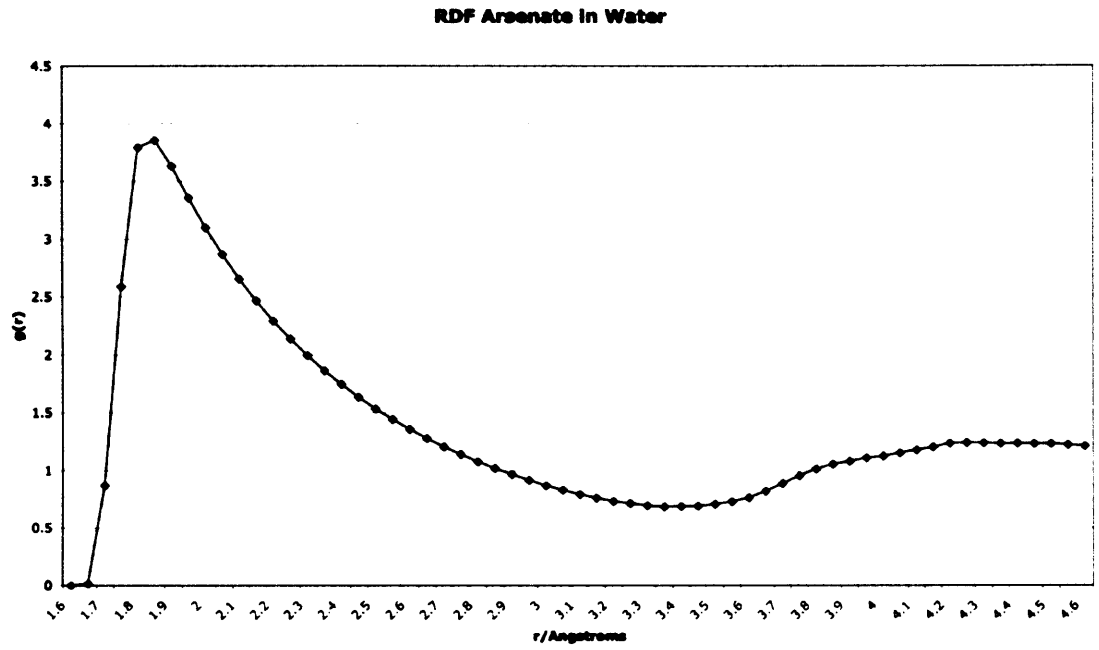

Figure 6.6 Radial distribution function for arsenate in a box of water

The solvation energy of arsenate has been calculated using SIESTA MD. The average equilibrated energy of the box of water containing 113 molecules and 15Å each side was taken, and the average energy per water molecule was calculated. The energy of arsenate in vacuum was also calculated from a geometry optimisation calculation. The solvation energy was then calculated as the difference in energy between arsenate in the vacuum and the energy of the arsenate molecule in the box of water, and found to equal -2.76 eV. This compares favourably with the energy given in Table 6.2, lying between the predicted solvation energies of the fully protonated and singly deprotonated arsenate molecule. This is to be expected, as the arsenate molecule spends time in both states during the MD simulation, but the energy is closer to that of the arsenate ion, which is its preferred state at the neutral pH of the simulation.

For comparison, a cluster of 10 water molecules around a fully protonated arsenate molecule was also run using Gaussian03 [2]. The aim of these calculations was to run the final calculation with the cluster surrounded by various implicit solvation models, however attempts to achieve this failed on each occasion, and following discussions with the Gaussian developers it was deduced that at present such calculations are not feasible using

the Gaussian03 [2] code. A 6-311G* basis set was used with the B3LYP functional to carry out QMMD for 500 steps of 1fs each, yielding a total run of 0.5ps in length. This calculation proved too computationally expensive enough to allow for an extended production run, especially when the desired functionality was not available. While proton transfer was observed during the Gaussian03 [2] MD calculation, it was not as long lived as that observed in the SIESTA calculation, and the smaller size of the cluster restricted the movement of the detached proton. The Gaussian03 [2] calculation was more computationally expensive than the SIESTA calculation and provided less instructive results due to the restrictions on cluster size. As such, the use of Gaussian03 [2] for this type of calculation is inadvisable until such time as further advances are made both in the code and in computational resources.

6.2. Arsenate at the Surface of Dolomite

Following the simulations of arsenate in water, and having confirmed that the methods employed produced the expected dissociation of the fully protonated arsenate molecule under neutral conditions, the necessity of using a charged molecule in surface adsorption calculations was clear. Consequently, initial calculations of the $AsO_4H_2^-$ on the dolomite (211) surface were carried out using the SIESTA code [3]. These precursive calculations facilitated the determination of the time-scales necessary to run calculations of this nature on a charged system.

A smaller slab depth of two layers was taken for these calculations, having been obtained from the surface of a larger, optimised, 6-layer slab. A 2x2 surface supercell was used in the calculations in order to prevent charge–charge interactions between periodic images. The 6 layers were found to be sufficient to converge the surface energy, which was found to have the value 0.58 Jm^{-2}, in accordance with the value of 0.55 Jm^{-2} obtained when using interatomic potential methods (Ch. 4) [18]. The geometry of the 2 layers taken from this slab was fixed at their optimised positions during the calculations. Eight different starting geometries were chosen. These sampled bidentate binuclear and bidentate mononuclear complexation at different surface sites, as is typical of arsenate at mineral surfaces at high

arsenate concentrations [19-24]. The molecule was placed over both Mg and Ca sites, with the arsenate molecule aligned either in the direction of the carbonate ions or against them (Figure 6.7). The molecule's geometry was slightly distorted at the start of each calculation so that the excess electron density would centre on the arsenate molecule, facilitating the optimisation.

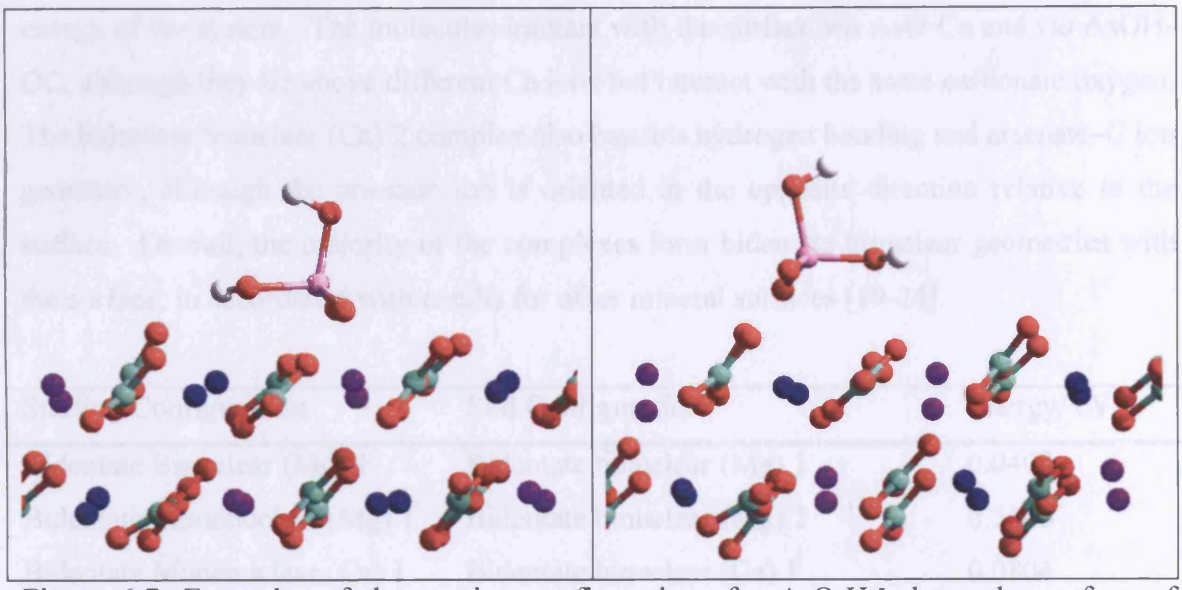

Figure 6.7: Examples of the starting configurations for $AsO_4H_2^-$ above the surface of dolomite.

Achieving convergence was difficult for all starting configurations. It proved necessary to decrease the mixing weight of the density matrix from the previous steps to avoid the SCF oscillating between two states. It was also necessary in some cases to reduce the maximum displacement per conjugate gradient step so that the potential energy surface was adequately sampled between local minima, as it became apparent that, as the optimisations progressed, the conjugate gradient algorithm was finding it difficult to determine a local minimum; even though the geometry was changing very little, the energy was fluctuating between states. Table 6.3 lists the energy difference between the lowest energy configuration for adsorption of the ion onto the dolomite surface, and gives the initial and final configurations.

The final lowest energy geometry was found to be a bidentate binuclear configuration. Rather than the arsenate oxygen atoms both interacting with cations of the same element, which lie in rows along the (211) surface, the arsenate molecule straddles a carbonate ion on the surface so that one oxygen atom interacts with a Ca cation and one interacts with a Mg cation (Figure 6.8). The two bidentate mononuclear (Ca) 1 complexes differ in the orientation of the arsenate molecule above the surface, resulting in a large difference in the energy of the system. The molecules interact with the surface *via* AsO-Ca and *via* AsOH-OC, although they lie above different Ca ions but interact with the same carbonate oxygen. The bidentate binuclear (Ca) 2 complex also has this hydrogen bonding and arsenate–C ion geometry, although the arsenate ion is oriented in the opposite direction relative to the surface. Overall, the majority of the complexes form bidentate binuclear geometries with the surface, in accordance with results for other mineral surfaces [19-24].

Starting Configuration	End Configuration	Energy/ eV
Bidentate Binuclear (Mg) 1	Bidentate binuclear (Mg) 1	0.0408
Bidentate Mononuclear (Mg) 1	Bidentate binuclear (Mg) 1	0.5346
Bidentate Mononuclear (Ca) 1	Bidentate binuclear (Ca) 1	0.0804
Bidentate Binuclear (Ca) 1	Bidentate binuclear (Ca) 1	0.8237
Bidentate Binuclear (Ca) 2	Bidentate binuclear (Ca) 2	0.4351
Bidentate Mononuclear (Ca) 2	Bidentate binuclear Ca,Mg 2	0
Bidentate Mononuclear (Mg) 2	Monodentate mononuclear (Mg) 2	0.1647
Bidentate Binuclear (Mg) 2	Bidentate binuclear Mg 2	0.5223

1= mol facing the direction of the CO_3 leaning, 2= facing against

Table 6.3: Relative energies and relaxed structures for different starting geometries

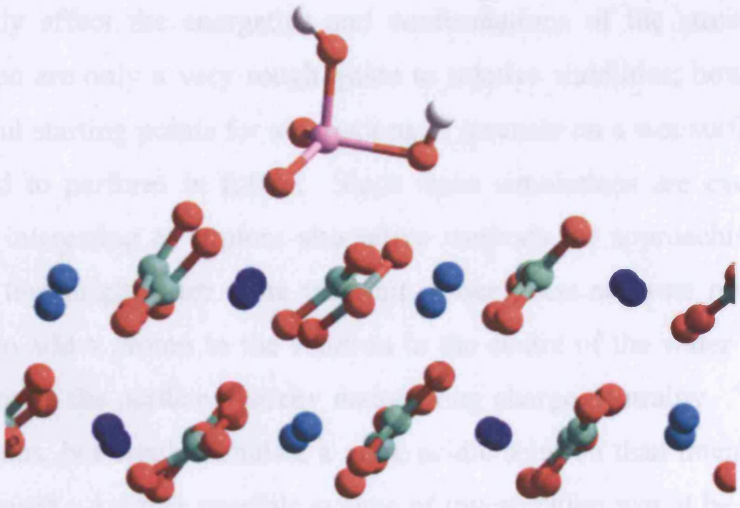

Figure 6.8: Most energetically favourable binding configuration for $AsO_4H_2^-$ on the dolomite (211) surface

To conclude, this chapter has detailed the exploration of approaches to full-scale DFT calculations of the behaviour of arsenate ions near dolomite surfaces. Therefore, the first section of this chapter showed results from Raman spectra, which showed that inclusion of solvation effects results in a marked improvement in the description of arsenate behaviour and are necessary in the generation of meaningful results.

QMMD calculations have been performed on the arsenate molecule, in order to understand its aqueous behaviour and its structural effects on the surrounding water. By comparing the resultant energy with that from an arsenate molecule in vacuum, and a box of water, a theoretical value of the solvation energy of the arsenate ion. This is a very useful quantity for further examination of arsenate near a surface, and for comparison with results from continuum models. As the arsenate molecule became deprotonated throughout this simulation, the singly deprotonated ion was used in further studies into the behaviour of arsenate under environmentally relevant conditions.

Finally, a series of possible starting configurations were generated for arsenate ions adsorbed onto a dry dolomite surface, and the molecular coordinates were then optimised.

These resulting configurations are of limited direct applicability, since the presence of water will significantly affect the energetics and conformations of the structures. The energies thereby gained are only a very rough guide to relative stabilities; however, they will provide very useful starting points for simulations of arsenate on a wet surface, which calculations we intend to perform in future. Since these simulations are exceptionally expensive, it may be interesting to explore alternative methods for approaching the wet adsorption behaviour that might offer more tractable, though less accurate results. One alternative would be to add a proton to the solution in the centre of the water slab while placing the arsenate ion at the surface, thereby maintaining charge neutrality. This might speed up the calculations, but would simulate a more acidic solution than intended unless the cell size was increased. Another possible avenue of investigation would be to develop a CPCM implementation for electronic structure surfaces, or to develop potentials for the arsenate ion, water, and carbonate interactions and use these to evaluate the problem. Work is underway to investigate the behaviour of water at the surface of dolomite through QMMD simulations in SIESTA. Preliminary results suggest that some dissociation of the solvent occurs at the (211) surface.

1. Barone, V. and M. Cossi, *Quantum calculation of molecular energies and energy gradients in solution by a conductor solvent model.* Journal of Physical Chemistry A, 1998. **102**(11): p. 1995-2001.
2. Frisch, M.J.T., G. W.; Schlegel, H. B.; Scuseria, G. E.; Robb, M. A.; Cheeseman, J. R.; Montgomery, Jr., J. A.; Vreven, T.; Kudin, K. N.; Burant, J. C.; Millam, J. M.; Iyengar, S. S.; Tomasi, J.; Barone, V.; Mennucci, B.; Cossi, M.; Scalmani, G.; Rega, N.; Petersson, G. A.; Nakatsuji, H.; Hada, M.; Ehara, M.; Toyota, K.; Fukuda, R.; Hasegawa, J.; Ishida, M.; Nakajima, T.; Honda, Y.; Kitao, O.; Nakai, H.; Klene, M.; Li, X.; Knox, J. E.; Hratchian, H. P.; Cross, J. B.; Bakken, V.; Adamo, C.; Jaramillo, J.; Gomperts, R.; Stratmann, R. E.; Yazyev, O.; Austin, A. J.; Cammi, R.; Pomelli, C.; Ochterski, J. W.; Ayala, P. Y.; Morokuma, K.; Voth, G. A.;

Salvador, P.; Dannenberg, J. J.; Zakrzewski, V. G.; Dapprich, S.; Daniels, A. D.; Strain, M. C.; Farkas, O.; Malick, D. K.; Rabuck, A. D.; Raghavachari, K.; Foresman, J. B.; Ortiz, J. V.; Cui, Q.; Baboul, A. G.; Clifford, S.; Cioslowski, J.; Stefanov, B. B.; Liu, G.; Liashenko, A.; Piskorz, P.; Komaromi, I.; Martin, R. L.; Fox, D. J.; Keith, T.; Al-Laham, M. A.; Peng, C. Y.; Nanayakkara, A.; Challacombe, M.; Gill, P. M. W.; Johnson, B.; Chen, W.; Wong, M. W.; Gonzalez, C.; and Pople, J. A.; Gaussian, Inc., Wallingford CT, 2004., *Gaussian 03, Revision C.02.*

3. Soler, J.M., et al., *The SIESTA method for ab initio order-N materials simulation.* Journal Of Physics-Condensed Matter, 2002. **14**(11): p. 2745-2779.

4. Aprà, E.W., T.L.; Straatsma, T.P.; Bylaska, E.J.; de Jong, W.; Hirata, S.; Valiev, M.; Hackler, M.; Pollack, L.; Kowalski, K.; Harrison, R.; Dupuis, M.; Smith, D.M.A; Nieplocha, J.; Tipparaju V.; Krishnan, M.; Auer, A.A.; Brown, E.; Cisneros, G.; Fann, G.; Früchtl, H.; Garza, J.; Hirao, K.; Kendall, R.; Nichols, J.; Tsemekhman, K.; Wolinski, K.; Anchell, J.; Bernholdt, D.; Borowski, P.; Clark, T.; Clerc, D.; Dachsel, H.; Deegan, M.; Dyall, K.; Elwood, D.; Glendening, E.; Gutowski, M.; Hess, A.; Jaffe, J.; Johnson, B.; Ju, J.; Kobayashi, R.; Kutteh, R.; Lin, Z.; Littlefield, R.; Long, X.; Meng, B.; Nakajima, T.; Niu, S.; Rosing, M.; Sandrone, G.; Stave, M.; Taylor, H.; Thomas, G.; van Lenthe, J.; Wong, A.; Zhang, Z.; NWChem, A Computational Chemistry Package for Parallel Computers, Version 4.6 (2004), Pacific Northwest National Laboratory, Richland, Washington 99352-0999, USA. and K. High Performance Computational Chemistry: an Overview of NWChem a Distributed Parallel Application, R.A.; Aprà, E.; Bernholdt, D.E.; Bylaska, E.J.; Dupuis, M.; Fann, G.I.; Harrison, R.J.; Ju, J.; Nichols, J.A.; Nieplocha, J.; Straatsma, T.P.; Windus, T.L.; Wong, A.T. Computer Phys. Comm., 2000, 128, 260-283 .

5. Becke, A.D., *Density-Functional Exchange-Energy Approximation With Correct Asymptotic-Behavior.* Physical Review A, 1988. **38**(6): p. 3098-3100.

6. Lee, C.T., W.T. Yang, and R.G. Parr, *Development Of The Colle-Salvetti Correlation-Energy Formula Into A Functional Of The Electron-Density*. Physical Review B, 1988. **37**(2): p. 785-789.
7. Becke, A.D., *Density-functional thermochemistry. III. The role of exact exchange*. The Journal of Chemical Physics, 1993. **98**(7): p. 5648-5652.
8. Tossell, J.A., *Theoretical studies on arsenic oxide and hydroxide species in minerals and in aqueous solution*. Geochimica Et Cosmochimica Acta, 1997. **61**(8): p. 1613-1623.
9. Vansant, F.K., Vanderve.Bj, and H.O. Desseyn, *Vibrational Analysis of Arsenic Acid and Its Anions .1. Description of Raman-Spectra*. Journal of Molecular Structure, 1973. **15**(3): p. 425-437.
10. Barone, V., M. Cossi, and J. Tomasi, *A new definition of cavities for the computation of solvation free energies by the polarizable continuum model*. Journal of Chemical Physics, 1997. **107**(8): p. 3210-3221.
11. Baldridge, K. and A. Klamt, *First principles implementation of solvent effects without outlying charge error*. Journal of Chemical Physics, 1997. **106**(16): p. 6622-6633.
12. Nosé, S., *A unified formulation of the constant temperature molecular dynamics methods*. The Journal of Chemical Physics, 1984. **81**(1): p. 511-519.
13. Perdew, J.P., K. Burke, and M. Ernzerhof, *Generalized Gradient Approximation made simple*. Physical Review Letters, 1996. **77**: p. 3865-3868.
14. Troullier, N. and J.L. Martins, *Efficient pseudopotentials for plane-wave calculations*. Physical Review B, 1991. **43**(3): p. 1993-2006.
15. Day, T.J.F., U.W. Schmitt, and G.A. Voth, *The mechanism of hydrated proton transport in water*. Journal of the American Chemical Society, 2000. **122**(48): p. 12027-12028.
16. Agmon, N., *The Grotthuss Mechanism*. Chemical Physics Letters, 1995. **244**(5-6): p. 456-462.
17. Myneni, S.C.B., et al., *Vibrational spectroscopy of functional group chemistry and arsenate coordination in ettringite*. Geochimica Et Cosmochimica Acta, 1998. **62**(21-22): p. 3499-3514.

18. Austen, K.F., et al., *The interaction of dolomite surfaces with metal impurities: a computer simulation study*. Physical Chemistry Chemical Physics, 2005. **7**(24): p. 4150-4156.

19. Foster, A.L., G.E. Brown, and G.A. Parks, *X-ray absorption fine structure study of As(V) and Se(IV) sorption complexes on hydrous Mn oxides*. Geochimica Et Cosmochimica Acta, 2003. **67**(11): p. 1937-1953.

20. Randall, S.R., D.M. Sherman, and K.V. Ragnarsdottir, *Sorption of As(V) on green rust (Fe-4(II)Fe-2(III)(OH)(12)SO4 center dot 3H(2)O) and lepidocrocite (gamma-FeOOH): Surface complexes from EXAFS spectroscopy*. Geochimica Et Cosmochimica Acta, 2001. **65**(7): p. 1015-1023.

21. Fendorf, S., et al., *Arsenate and chromate retention mechanisms on goethite .1. Surface structure*. Environmental Science & Technology, 1997. **31**(2): p. 315-320.

22. Roddick-Lanzilotta, A.J., A.J. McQuillan, and D. Craw, *Infrared spectroscopic characterisation of arsenate (V) ion adsorption from mine waters, Macraes mine, New Zealand*. Applied Geochemistry, 2002. **17**(4): p. 445-454.

23. Ladeira, A.C.Q., et al., *Mechanism of anion retention from EXAFS and density functional calculations: Arsenic (V) adsorbed on gibbsite*. Geochimica Et Cosmochimica Acta, 2001. **65**(8): p. 1211-1217.

24. Sherman, D.M. and S.R. Randall, *Surface complexation of arsenic(V) to iron(III) (hydr)oxides: Structural mechanism from ab initio molecular geometries and EXAFS spectroscopy*. Geochimica Et Cosmochimica Acta, 2003. **67**(22): p. 4223-4230.

7. CONCLUSIONS AND FURTHER WORK

"Reasoning draws a conclusion, but does not make the conclusion certain, unless the mind discovers it by the path of experience." Roger Bacon, 1214-1294.

This work has been directed towards providing a better understanding of the surface processes of dolomite in aqueous environments. In the first instance, the dominant dolomite surfaces were studied in vacuum using empirical potentials using the GULP 3.0 code [1], and surface energies and geometries were obtained. The relative stabilities of the surfaces varied slightly from those calculated previously [2], due to the improved description of the carbonate ion in the potential used in this study [3]. Environmentally common impurity cations were substituted at these surfaces, for which potentials were developed [4, 5]. The substitution energy was calculated with respect to the energy of the impurity's bulk end-member carbonate, and while it was found that the enthalpy difference between the pure and the substituted surface varied as the ionic radius of the impurity ion, the substitution energy, which represents the exchange of cations in a solid-solution, shows that substitutions by Cd and Mn of Mg at the $(11\bar{2}0)$ surface are the most favourable, and that these cations, along with Zn and Co, will also substitute at the Ca site on this surface. The preference for the $(11\bar{2}0)$ surface is due to its more open surface geometry, such that the cations on the surface are less tightly bound than the other surfaces studied. Steps on the $(10\bar{1}4)$ surface were also studied under vacuum conditions. The most energetically favoured step was found to be the acute carbonate ion termination, with an exposed Ca ion on the opposite side of the trough. Impurity substitutions on this surface were shown to be far more energetically favourable, as the cations are considerably more accessible at step defects, especially at the step edge. The substitutions at the surface showed that Zn incorporation was preferred over the other cations studied, but that all the substitutions were favourable at both Ca and Mg sites on the surface, although there is some evidence of steric hindrance to substitutions of the larger cations: Cd, Fe and Mn.

Overall, these calculations have shown that some information on mineral surface behaviour can be gleaned from the study of surfaces under vacuum, such as the comparative ease of substitution at various surfaces, and the effect of surface defects. While the *in vacuo* calculations are computationally inexpensive, and while they provide the previously mentioned insights, it must be remembered that, in the environment, it is of great interest to understand the behaviour of surfaces at the mineral-aqueous solution interface. In order to understand the behaviour of aqueous pollutants and minerals, it is of utmost importance that solvation of both the surface and the foreign species of interest is taken into account.

Two approaches were used to solvate the dolomite surfaces. The first was the oft-used application of a monolayer of water to the surface, which stabilised the $(10\bar{1}4)$ surface by 0.3 Jm^{-2}. It was not possible to find global minima for the other surfaces that were studied, a drawback to the monolayer method. The geometry of the monolayer at the $(10\bar{1}4)$ surface was found to differ from that predicted using previous carbonate potentials, such that the water molecules face the opposite way on the surface, pointing in the direction towards which the carbonate ions lean [2, 4, 6]. Substitutions were made on the solvated surface, incorporating the solvation energy of the impurity and the substituted cations. It was found that, using this model, substitutions were almost universally unfavourable, with the exception of the Ca substitution at an Mg site, although the substitution energy for Mn at the Mg site was fairly close to zero. These results show that, using the monolayer approximation, Ca/Mg disordering is likely. However, the monolayer approximation is not quite adequate for modelling the solvent effects on a mineral surface, as it provides none of the long-range electrostatic effects that should be present from bulk water. The neglect of the electrostatic contribution could explain the slightly unfavourable substitution for Mn at the Mg site, despite experimental evidence that Mn/Mg impurities are observed [7].

The second approach to the solvation of dolomite surfaces was the application of a newly implemented continuum solvation method for surfaces in GULP [1], COSMIC [8]. The method was found to be useful in the study of substitution energies, but

proved less robust in the prediction of crystal morphology. The substitution energies gained generally followed the trend described by the monolayer approach, but the substitution energy of Mn at the Mg site was more favourable. Once again Ca/Mg substitutions were predicted as energetically favourable, indicating that the growth of calcite or disordered magnesian calcite is favourable thermodynamically. The drawback of these types of calculations is the neglect of kinetic barriers in the predictions made. While thermodynamic factors are of great importance, for substitution at the surfaces the kinetic barriers to substitution may be great, and as such a more complete picture of mineral surface interactions would also include such considerations, by the use of molecular dynamics calculations.

The aim of the final chapter of this thesis was to use DFT to study the $(10\bar{1}4)$ surface under explicit solvation and the adsorption of the arsenate molecule onto the surface both under vacuum conditions and when solvated for the purpose of comparison. Due to time constraints and the expense of the calculations, the QMMD calculations of the solvated surface are not reported here, but will follow in a future publication. Preliminary results indicate that there is dissociation of the water directly above the surface, but further time in the production phase is needed for these results to be quantifiable.

The arsenate molecule was studied using MD and DFT in both the Gaussian03 [9] and SIESTA [10] programs, from which studies it was found that the SIESTA program is a more appropriate tool for this type of study. It was found that the arsenate molecule imposes no appreciable ordering on its immediate surrounding solvent, but that it will dissociate as expected to form its singly deprotonated ion at neutral pH. Armed with this result, the singly deprotonated arsenate ion was introduced to the $(10\bar{1}4)$/ (211) dolomite surface, and the geometry optimised using the SIESTA program [11]. These geometry optimisations were far more cumbersome and time-consuming than expected, and great efforts were needed to coax the system into an optimised geometry. Consequently, the planned MD simulation of the solvated ion's approach to the solvated surface was deemed impractical using present methods and computing

facilities. However, under vacuum the molecule was found to form a bidentate binuclear complex with the surface, which bridges over a carbonate ion to interact with both a Ca and an Mg ion, and the inclusion of solvation, while it may affect the energetics of adsorption and subtly affect the geometry, is not expected to greatly affect the preference for this geometry, which relies upon interaction of the unhydroxylated arsenate oxygens with the surface cations.

Throughout this work, a method for the modelling of mineral-solution interactions has been sought. The most interesting aspect of this problem has been found to be the accurate and efficient inclusion of the solvent. Newly implemented continuum methods have been applied to the system, using the environmentally significant mineral dolomite as an example. Simulations of arsenate ions in solution have been successfully performed with full quantum DFT molecular dynamics, and the resultant energies and conformations investigated. Further, large steps have been taken towards performing similar simulations for the much more challenging system of the arsenate ion on a wet dolomite surface.

In a more general context, this work has been useful for evaluating the utility of various methods for calculating mineral-solution systems. It is important to quantify the importance of explicitly describing the water molecules, and of their dissociative behaviour. Methods of describing solvated pollutants have been probed and evaluated in the context of their application to the mineral-solution system, using the arsenate molecule as a model impurity, and it has been found that the continuum method is sufficient, at least for the arsenate molecule, which does not impose ordering upon the surrounding solvent. This result is not immediately transferable to other species, whose solvation may cause more significant ordering; therefore, it is important to evaluate this for any impurity studied.

A number of areas of the work would be of particular interest to investigate further. It would be of great interest to include solvation into the model for adsorption of arsenate onto the dolomite surface. Currently, as the computational cost of the DFT MD

calculations is too great, it would be instructive to develop a dissociative potential for water at the surface and for the arsenate molecule, and thereafter employ classical molecular dynamics to evaluate the free energy of adsorption. The alternative to this method, which has been shown by the results of continuum solvation calculations in this work to be viable, would be to implement continuum solvation for surfaces in a DFT code and incorporate solvation effects in this way. Additionally, it be of great interest to investigate the effect of incorporation of the metal cation impurities during nucleation and growth. This could be carried out either by static geometry optimisations, or by molecular dynamics calculations of surface growth. Finally, investigations of the formation of aqueous complexes of arsenate and other relevant metal cations, specifically iron, and the interaction of these complexes with dolomite surfaces, would be an exciting addition to the current work on the subject.

1. Gale, J.D. and A.L. Rohl, *The General Utility Lattice Program (GULP).* Molecular Simulation, 2003. **29**(5): p. 291-341.
2. De Leeuw, N.H., *Surface structures, stabilities, and growth of magnesian calcites: A computational investigation from the perspective of dolomite formation.* American Mineralogist, 2002. **87**(5-6): p. 679-689.
3. Rohl, A.L., K. Wright, and J.D. Gale, *Evidence from surface phonons for the (2x1) reconstruction of the (10(1)over-bar4) surface of calcite from computer simulation.* American Mineralogist, 2003. **88**(5-6): p. 921-925.
4. Austen, K.F., et al., *The interaction of dolomite surfaces with metal impurities: a computer simulation study.* Physical Chemistry Chemical Physics, 2005. **7**(24): p. 4150-4156.
5. Austen, K.F., et al., *Computer modelling of the structure and stability of carbonate surfaces.* SOPRO 2004 Abstracts, 2004.
6. Wright, K., R.T. Cygan, and B. Slater, *Structure of the (10(1)over-bar4) surfaces of calcite, dolomite and magnesite under wet and dry conditions.* Physical Chemistry Chemical Physics, 2001. **3**(5): p. 839-844.

7. Granwehr, J., P.G. Weidler, and A.U. Gehring, *The fate of structure-bound Mn2+ during the decomposition of dolomite and in the resulting conversion products.* Geochimica Et Cosmochimica Acta, 2004. **68**(11): p. A107-A107.

8. Gale, J.D. and A.L. Rohl, *An efficient technique for the prediction of solvent-dependent morphology: The COSMIC method.* In Preparation.

9. Frisch, M.J.T., G. W.; Schlegel, H. B.; Scuseria, G. E.; Robb, M. A.; Cheeseman, J. R.; Montgomery, Jr., J. A.; Vreven, T.; Kudin, K. N.; Burant, J. C.; Millam, J. M.; Iyengar, S. S.; Tomasi, J.; Barone, V.; Mennucci, B.; Cossi, M.; Scalmani, G.; Rega, N.; Petersson, G. A.; Nakatsuji, H.; Hada, M.; Ehara, M.; Toyota, K.; Fukuda, R.; Hasegawa, J.; Ishida, M.; Nakajima, T.; Honda, Y.; Kitao, O.; Nakai, H.; Klene, M.; Li, X.; Knox, J. E.; Hratchian, H. P.; Cross, J. B.; Bakken, V.; Adamo, C.; Jaramillo, J.; Gomperts, R.; Stratmann, R. E.; Yazyev, O.; Austin, A. J.; Cammi, R.; Pomelli, C.; Ochterski, J. W.; Ayala, P. Y.; Morokuma, K.; Voth, G. A.; Salvador, P.; Dannenberg, J. J.; Zakrzewski, V. G.; Dapprich, S.; Daniels, A. D.; Strain, M. C.; Farkas, O.; Malick, D. K.; Rabuck, A. D.; Raghavachari, K.; Foresman, J. B.; Ortiz, J. V.; Cui, Q.; Baboul, A. G.; Clifford, S.; Cioslowski, J.; Stefanov, B. B.; Liu, G.; Liashenko, A.; Piskorz, P.; Komaromi, I.; Martin, R. L.; Fox, D. J.; Keith, T.; Al-Laham, M. A.; Peng, C. Y.; Nanayakkara, A.; Challacombe, M.; Gill, P. M. W.; Johnson, B.; Chen, W.; Wong, M. W.; Gonzalez, C.; and Pople, J. A.; Gaussian, Inc., Wallingford CT, 2004., *Gaussian 03, Revision C.02.*

10. Soler, J.M., et al., *The SIESTA method for ab initio order-N materials simulation.* Journal Of Physics-Condensed Matter, 2002. **14**(11): p. 2745-2779.

11. Austen, K.F., et al., *Computational Investigation into the Adsorption of Pollutants onto Mineral Surfaces: Arsenate and Dolomite.* MRS Abstracts Spring 2006, 2006.

"...for what greater wealth can there be than cheerfulness, peace of mind, and freedom from anxiety?"

Thomas More, 1478-1535.

The End.